UNIVERSITY OF CALIFORNIA

Santa Barbara

Correlation Effects and Emergent Phases in Oxide Heterostructures

A Dissertation submitted in partial satisfaction

of the requirements for the degree of

Doctor of Philosophy

in

Materials

by

Patrick Brian Marshall

Committee in Charge:

Professor Susanne Stemmer, Chair

Professor S. James Allen

Professor Christopher Palmstrøm

Professor Stephen Wilson

December 2018

The Dissertation of

Patrick Brian Marshall is approved:

Professor S. James Allen

Professor Christopher Palmstrøm

Professor Stephen Wilson

Professor Susanne Stemmer, Committee Chairperson

October 2018

Correlation Effects and Emergent Phases in Oxide Heterostructures

Acknowledgements

What really distinguishes the Materials department at UCSB as an elite graduate program are the intellectual and personal qualities of the faculty and staff and their willingness to go well out of their way to share both their knowledge and experience with students. First, I would like to thank my advisor Susanne Stemmer for the instruction, guidance, and the opportunities to participate in world-class research she provided throughout my five years in the program. Most importantly, she always made herself available to her students. I would also like to express my gratitude to the members of my doctoral committee: Jim Allen, Christopher Palmstrøm, and Stephen Wilson. The ongoing scientific insight they provided through discussions, during both the preliminary examinations and impromptu meetings, has been invaluable in shaping the work in this thesis. Collaboration with Stephen Wilson and his student Ryan Need greatly added to our understanding of the nature of the magnetism in the titanate quantum wells discussed in this work.

I would also like to express my gratitude to the excellent group of graduate students and postdocs, both past and present, which I have had the opportunity to work with during my tenure at UCSB. The present group includes Chris Freeze, Timo Schumann, Manik Goyal, Honggyu Kim, Omor Shoron, Kaveh Ahadi, David Kealhofer, Salva Rezaie, Luca Galleti, Nick Combs, Wangzhou Wu, Hanbyeol Jeong, Alex Lygo, Raj Chaklashiya, and Tyler Pardue. In particular, I would like to acknowledge Honggyu for the guidance and stimulating discussions he provided during the time we shared an office and Kaveh for close collaboration on the correlated oxide projects. I would also like to acknowledge

former group members Evgeny Mikheev and Santosh Raghavan for their assistance and training related to much of the work presented in this thesis and Clayton Jackson for laying the groundwork for the study of quantum criticality in the titanate heterostructures.

The nature of MBE growth necessitates technical expertise and experience. I would like to thank the engineers of the MBE laboratory, John English and Kurt Olsson, for their technical input and invaluable assistance in the maintenance of the MBE lab over the years. Without their support this research would not have been possible. I would also like to thank the staff of the UCSB Nanofabrication Facility, Amanda Strom for managing the TEMPO measurement facilities in the MRL, and Youli Li for managing the x-ray characterization facilities.

Finally, I would like to express my gratitude to Professor Bharat Jalan at the University of Minnesota. He first introduced me to the world of MBE when I was an undergraduate and he played a pivotal role in my decision to pursue my graduate studies in the Materials department at UCSB. For that I will always be thankful.

Curriculum Vitæ

Patrick Brian Marshall

Education

PhD in Materials, University of California, Santa Barbara 2013-2018

BS in Materials Science & Engineering, University of Minnesota 2008-2012

Awards

National Science Foundation Graduate Research Fellowship (2014-2017)

APL Materials Excellence in Research Award, 3rd place (2017)

APS Division of Materials Physics Ovshinsky Travel Award (2017)

University of Minnesota College of Science & Engineering Merit Scholarship (2011)

Professional Appointments

Graduate Student Researcher, University of California Santa Barbara 2013-2018

Teaching Assistant, University of California, Santa Barbara Winter 2014

Undergraduate Research Assistant, University of Minnesota 2012-2013

Publications

P.B. Marshall, K. Ahadi, H. Kim, and S. Stemmer. "Electron nematic fluid in a strained $Sr_3Ru_2O_7$ film", *Physical Review B* 5 155160 (2018)

P.B. Marshall, H. Kim, K. Ahadi, and S. Stemmer. "Growth of strontium ruthenate films by hybrid molecular beam epitaxy", *APL Materials* 5 096101 (2017)

P.B. Marshall, H. Kim, and S. Stemmer. "Disorder versus two transport lifetimes in a strongly correlated electron liquid", *Scientific Reports* 7 10312 (2017)

P.B. Marshall, E. Mikheev, S. Raghavan, and S. Stemmer. "Pseudogaps and Emergence of Coherence in Strongly Correlated Electron Liquids in $SrTiO_3$", *Physical Review Letters* 117 046402 (2016)

R.F. Need, **P.B. Marshall**, E. Weschke, A.J. Grutter, D.A. Gilbert, E. Arenholz, P. Shafer, S. Stemmer, and S.D. Wilson. "Resolving interfacial charge transfer in titanate superlattices using resonant x-ray reflectometry", *Physical Review Materials* 2 093801 (2018)

R.F. Need, **P.B. Marshall**, E. Kenney, A., T. Prokascha, Z. Salman, B.J. Kirby, S. Stemmer, M.F. Graf, and S.D. Wilson. "Quasistatic antiferromagnetism in the quantum wells of $SmTiO_3/SrTiO_3$ heterostructures", *Quantum Materials* 7 (2018)

H. Kim, **P.B. Marshall**, K. Ahadi, T.E. Mates, E. Mikheev, and S. Stemmer. "Response of the lattice across the filling-controlled Mott metal-insulator transition of a rare earth titanate", *Physical Review Letters* 119 186803 (2017)

K. Ahadi, O.F.Shoron, **P.B.Marshall**, E.Mikheev, and S.Stemmer. "Electric field effect near the metal-insulator transition of a two-dimensional electron system in $SrTiO_3$", *Applied Physics Letters* 110 062104 (2017)

W.J. Hardy, B. Isaac, **P. Marshall**, E. Mikheev, P. Zhou, S. Stemmer, and D. Natelson. "Potential Fluctuations at Low Temperatures in Mesoscopic-Scale $SmTiO_3/SrTiO_3/SmTiO_3$ Quantum Well Structures", *ACS Nano* 11 3760 (2017)

T. Wang, K. Ganguly, **P. Marshall**, P. Xu, and B. Jalan. "Critical thickness and strain relaxation in MBE-grown $SrTiO_3$", *Applied Physics Letters* 103 212904 (2013)

E. Mikheev, S. Raghavan, J.Y. Zhang, **P.B. Marshall**, A.P. Kajdos, L. Balents, S. Stemmer. "Carrier density independent scattering rate in $SrTiO_3$-based electron liquids", *Scientific Reports* 6 20865 (2016)

Abstract

Correlation Effects and Emergent Phases in Oxide Heterostructures

Patrick Brian Marshall

Strong electron correlations in transition metal oxides give rise to the emergence of a diverse array of transport phenomena and emergent phases such as quantum criticality, nematic order, and magnetism. The synthesis of thin films of these materials using molecular beam epitaxy (MBE) has enabled the discovery of additional phases that are not observed in bulk crystals. Furthermore, the precision offered by MBE over layer thickness in the growth of heterostructures and subtle modifications of the lattice imposed by epitaxial strain open the possibility of tuning these phases. The central aim of the work in this thesis is to explore the relationships between the strongly correlated transport phenomena and emergent phases and the structure of the MBE-grown crystal. This includes tilting and connectivity of the oxygen octahedra in the perovskite structure, quantum well thickness, epitaxial strain, and proximity effects.

The thesis begins with an introduction to the physics of metallic transport in correlated materials with an emphasis on highlighting the phenomena that have been observed in the MBE-grown materials discussed in this work. This includes pseudogap behavior in the density of states, quantum criticality, non-Fermi liquid transport, and Van Hove singularities in the electronic structure. This is followed by an overview of the specific perovskite materials and the hybrid MBE growth technique used to synthesize them.

The body of the experimental work in this thesis is comprised of two main parts. First, investigations of the electron correlations in RTiO$_3$/SrTiO$_3$/RTiO$_3$ (R = Gd, Sm) quantum wells will be discussed. This includes tunneling spectroscopy experiments in which tunnel junction devices were fabricated to the pseudogap phase that emerges in the two-dimensional electron gas residing in the well. A robust quadratic dependence of the Hall angles in these quantum wells is discussed. The second part focuses on the transport properties of the layered strontium ruthenate Ruddlesden-Popper series. A novel method of growing these materials incorporating the use of the volatile precursor RuO_4 is introduced. Finally, a study of the electronic and magnetic properties of an epitaxially strained $Sr_3Ru_2O_7$ film is discussed, where it was found that slight perturbations of the lattice greatly enhance the emergent ordered phases. The thesis concludes with a brief summary and proposals for future research in correlated oxides.

Contents

List of Figures

Chapter 1 Introduction to Transport in Correlated Materials

1.1 Transport in *d* and *f*-bands in Transition Metal Oxides

In the conventional semiconductors commonly used in modern electronic devices, prototypical examples being Si and the III-V semiconductors, electronic bands arising from *s* and *p*-orbitals dominate transport. These large orbitals are delocalized within the crystal lattice, which has the effect of increasing the bandwidth and kinetic energy of the charge carriers. As a consequence, the interactions between the charge carriers in these materials, such as those arising from spin or charge, are relatively weak. This allows for a rather facile understanding and prediction of the transport properties with models that approximate the charge carriers as non-interacting particles. This is compounded by the fact that the sheet carrier densities in the commonly studied two-dimensional electron gases (2DEGs) are low (typically not exceeding 10^{-13} cm^{-2}). The comprehensive understanding and modeling of this transport regime and the vast array of heterostructures and processing techniques that have been engineered over many decades have allowed for the development of the semiconductor devices that are ubiquitously used in modern technology. Nevertheless, the weak interactions between the charge carriers and the resultant simple electronic and magnetic phase diagrams represent an inherent limitation of these materials as the demand for new types of functionality increases.

In contrast, electronic bands arising from *d* and *f*-orbitals largely govern the transport in complex transition metal oxides. These orbitals are more localized within the lattice with less overlap. For example, the spatial extent of transition metal *d* orbitals is

typically on the order of 0.5 Å compared to the roughly 4 Å spacing of the transition metal ions themselves [1]. As a result, the electrons contributing to transport experience a narrower bandwidth and are more localized near individual atomic sites, a situation illustrated in Figure 1.1. Carriers traversing the lattice experience a strong Coulombic repulsion at occupied atomic sites due to the like charges of the electrons. This effect is enhanced at high carrier densities, as is the case in the strongly correlated 2DEGs to be discussed in Chapters 3 and 4, where the electrostatic doping can induce sheet carrier densities up to 7×10^{14} cm^{-2}. A simple physical argument to explain this is that the electron-electron Coulomb forces are enhanced when there is a high probability for two electrons to occupy the same atomic site. This double occupation is more likely at high carrier densities, and in particular when the band is half filled. The strength of this on-site interaction is often parameterized by the variable U in the literature.

A related but converse parameter is t, which is a measure of the tendency for the charge carriers to delocalize in the lattice by hopping to neighboring atomic sites. It is sometimes referred to as the *hopping integral*. The ratio U/t is therefore a measure of the charge carriers' tendency to localize versus their tendency towards itinerancy, and it is the delicate balance and competing interactions between these states that gives rise to the rich variety of unconventional metallic behavior found in correlated metals and semiconductors [2]. A related quantity is U/W, where W is the bandwidth of the conduction band. In normal metals $U/W < 1$, while the case of $U/W > 1$ promotes Mott insulating behavior [2]. In correlated metals U/W is near unity. Thus, when the strength of the onsite

Coulomb interactions is on the order of the bandwidth one may expect electron correlation effects to play an important role in transport, giving rise to unconventional metallic behavior. This quantity is one of the fundamental distinctions between conventional transport in weakly correlated semiconductors and metals and transport in strongly correlated transition metal oxides.

The strong tendency towards localization in correlated materials gives rise to the emergence of degrees of freedom whose effects are usually suppressed in materials in which the electrons interact weakly. These include effects related to the charge, orbital, lattice, and spin degrees of freedom [3]. The interplay of these additional degrees of freedom influence the charge carriers via effects related to crystal field splitting, bandwidth modification, Coulomb interactions, and Hund's coupling. These competing interactions, in turn, lead to the emergence of unusual correlated electronic and magnetic phases as illustrated in Figure 1.2. An example is the hallmark discovery of unconventional high-temperature superconductivity in layered cuprate compounds in 1986 [4]. This led to a surge of detailed studies of this class of materials in an effort to uncover how the delicate interplay of these interactions could lead to an electron pairing mechanism at high temperatures, an understanding of which would have wide ranging applicability in both the theory of condensed matter physics and technology. Another major development was the discovery of colossal magnetoresistance in the manganite perovskites [5].

In the early 2000s research on oxide thin film heterostructures revealed the discovery of a conductive electron gas at the $LaAlO_3/SrTiO_3$ oxide interfaces [6]. This was

accompanied by the observation of superconductivity, magnetism, and even the coexistence of superconducting and magnetic order at these interfaces, hinting at the important role played by the narrow and strongly correlated Ti 3*d* bands in transport in $SrTiO_3$ [7]–[10]. Similar electron gases are present at $RTiO_3/SrTiO_3$ (*R* = Gd, Sm) interfaces with sheet charge densities that are even higher than those at the $LaAlO_3/SrTiO_3$ interface [11]. The growth of heterostructures of these materials by molecular beam epitaxy (MBE) provides the ability to carry out experiments to explore the underlying correlation physics of these low-dimensional electron systems, as well as opening up new routes toward atomic scale engineering not possible with bulk synthesis techniques. Experiments can be designed in which a number of degrees of freedom can be tuned systematically to offer new insight into how correlated phases emerge from the underlying correlation-driven degrees of freedom. Such studies are the central subject of this thesis. In summary, the strong electron-electron interactions, rich phase diagrams, and the ability to systematically tune the emergent ordered phases contribute to the tremendous potential of transition metal oxides in the development of new functional oxide devices with capabilities that are beyond the reach of conventional weakly correlated elemental or III-V semiconductor materials. The following sections will highlight some of the unusual emergent phases and transport phenomena that have been observed experimentally in correlated transition metal oxides.

1.2 Mott Metal-to-Insulator Transition

Among the many phenomena that have been explored over decades of research in the field of strongly correlated materials, perhaps the most quintessential is the Mott metal-to-insulator transition. The Mott metal-to-insulator transition is an electronically driven phase transition from a metallic to an insulating state that is predicted to occur when the strength of the Coulomb repulsion between electrons on nearby atomic sites U becomes sufficiently large relative to the hopping integral t. When the ratio U/t reaches a critical value the electrons self-localize, and a material that would be predicted to exhibit metallic behavior with a partially filled conduction band according to classical band theory is driven into an insulating state. The first example of this contradictory behavior was observed in nickel oxide [12]. Eugene Wigner subsequently proposed that electron-electron interactions may underlie the phenomenon [13], and a quantitative model was put forth by Neville Mott [14].

A simple physical picture is provided by a single band Hubbard model described by a Hubbard Hamiltonian of the form

$$\mathcal{H}_H = -t \sum_{<i,j>,\sigma} \left(c_{i\sigma}^{\dagger} c_{j\sigma} + c_{j\sigma}^{\dagger} c_{i\sigma}\right) + U \sum_{i} n_{i\uparrow} n_{i\downarrow} + \mu \sum_{i,\sigma} n_{i,\sigma} \qquad 1.1$$

where i and j are indices of the atomic sites, $\sigma = (\uparrow, \downarrow)$ are the electron spins, $c_{i\sigma}^{\dagger}$ and $c_{j\sigma}$ are the particle creation and annihilation operators, and $n_{i\uparrow} \equiv c_{i\sigma}^{\dagger} c_{i\sigma}$ is the number operator [15]. The first term can be thought of as the kinetic energy, which is proportional to the

hopping integral t. The summation over $< i,j >$ signifies that hopping can occur only between neighboring atomic sites. The second term can be thought of as the potential energy cost arising from the repulsive Coulomb interaction when two electrons occupy the same atomic site i. The value of U, as discussed in previous sections, describes the strength of the electron-electron interactions. The final term, accounting for band filling, is characterized by the chemical potential μ. When $t \gg U$ the kinetic energy dominates and the system is can be described by classical band theory. The limit of $U \gg t$ corresponds to the case of isolated atoms, where the interatomic distance is far too great for electron hopping and insulating behavior prevails. The most interesting behavior is observed for intermediate cases where the relative values of U and t place the system in close proximity of a metal-to-insulator transition. The interplay of the metallic and insulating states can lead to the emergence of magnetic ordering and unconventional metallic behavior [2].

The strong on-site Coulomb repulsions in the case of sufficiently large U/t open up a *Mott gap* in the conduction band, illustrated in Figure 1.3. The band structure in the Mott insulating state then consists of an occupied lower Hubbard band (LHB) and an unoccupied upper Hubbard band (UHB) separated by the Mott gap defined by U.

Mott insulating behavior is commonly observed in oxides containing light $3d$ transition metals. Prototypical examples of transition metal oxides that host a Mott metal-insulator transition are the vanadates and the rare earth titanates [2], [16], [17]. Two Mott insulators that play a central role in the work discussed in this thesis are the rare earth titanates $GdTiO_3$, and $SmTiO_3$. These materials, which are orthorhombic perovskites with

d^1 electron configurations, were used as the barrier materials for the quantum wells discussed in Chapters 3 and 4. The insulating nature of these materials and their conduction band offset with the band insulator $SrTiO_3$ provide an electrostatic potential barrier to confine the conduction electrons in the $SrTiO_3$ well.

1.3 Fermi Liquid Scattering Behavior

Fermi liquid theory is a framework in which weak electron-electron interactions can be accounted for in predictions of the thermodynamic and transport properties of a correlated metal [18]. The central concept of the theory is that if the interactions in a many-body electron system are treated adiabatically, the electron eigenstates transition smoothly from the case of a non-interacting electron gas to the interacting system. That is to say, when the interactions are turned on sufficiently slowly, there is a one-to-one correspondence between the eigenstates in the non-interacting and the weakly interacting scenarios. This preserves quantum numbers such as spin and charge. Other properties, such as effective mass, specific heat, and spin susceptibility, are renormalized. The end result is that these renormalized quantities show the same qualitative temperature dependence but take on values that differ from those in the non-interacting picture, with the extent of the change being governed by the strength of the electron-electron interactions in the metal. The renormalized charge carriers are referred to as *quasiparticles*, which obey the Pauli exclusion principle and Fermi-Dirac statistics just as the "bare" electrons would.

The Fermi liquid framework is restricted to low temperatures ($k_B T < E_F$) where the quasiparticles are well-defined.

The presence of a Fermi liquid state is predicted to give rise to a T^2 temperature dependence of the resistivity at temperatures that sufficiently low such that phonons are not the dominate scattering mechanism [19]. In the Drude model of metallic transport the electrical resistivity is given by

$$\rho = \frac{m^*}{ne^2\tau} \tag{1.2}$$

where m^* is the effective mass, n is the three-dimensional carrier concentration, and τ is the average electron scattering time. Of these quantities, the scattering time τ (or equivalently the scattering rate τ^{-1}) primarily influences the temperature dependence. At a temperature of absolute zero, where the Fermi sphere is filled up to the Fermi level (E_F), scattering events will occur between an excited electron above the Fermi level ($E_1 \geq E_F$) and an electron below the Fermi level ($E_2 \leq E_F$). They will be scattered into unoccupied states with energies $E_{3,4} > E_F$. Energy conservation imposes that

$$E_1 + E_2 = E_3 + E_4. \tag{1.3}$$

With the condition of T = 0 K there is no thermal activation energy, so $E_1 = E_F$. Pauli's exclusion principle dictates that no states within the Fermi sphere can be doubly occupied, so it follows that $E_{2,3,4} = E_F$. This means that the phase space for scattering around the Fermi sphere at absolute zero is vanishingly small. For $T > 0$, a shell around the Fermi

sphere of width of approximately $k_B T$ will be created in which scattering can take place. The scattering event probability for the excited electron with energy $E_1$is calculated by double integration though the phase space. Doing so reveals a scattering rate that scales as $\tau^{-1} \propto T^2$, and therefore at sufficiently low temperatures the resistivity can be expected to follow a dependence of the form

$$\rho(T) = \rho_0 + AT^2, \qquad 1.4$$

where ρ_0 is the residual resistivity arising from impurity scattering and A is the scattering amplitude coefficient. Because of this, a T^2 dependence of the resistivity is oftentimes interpreted as strong experimental evidence of the existence of a Fermi liquid. However, as will be discussed in Chapter 4, this straightforward interpretation is likely too simplistic in many cases. Robust T^2-dependences in the transport coefficients, and in particular in the Hall angle (to be introduced in Section 1.5), are often observed under conditions that should otherwise exclude Fermi liquid behavior. For example, according to Fermi liquid theory the scattering rate should be dependent on the carrier density. However, in many correlated materials, a carrier density independent scattering rate is observed over a range of densities that spans multiple decades. A good example of this anomaly has been noted in $SrTiO_3$ [20]. A T^2 resistivity dependence is also observed in $SrTiO_3$ at high temperatures where Fermi liquid theory should not apply. This points to the need for a more complete theory of T^2 dependences in the transport coefficients of strongly correlated metals that goes beyond the standard Fermi liquid framework.

1.4 Quantum Criticality and Non-Fermi Liquid Transport

A quantum critical point is a phase transition between two quantum ground states that occurs at 0 K [21]. This is typically achieved through the suppression of a temperature-driven phase transition to zero temperature. In a classical phase transition the temperature of the system is one of the parameters determining the phase, with thermal fluctuations destroying ordered phases above a critical temperature. In contrast, quantum phase transitions are driven by a non-thermal *external tuning parameter*, which can include chemical composition in an alloy system, applied pressure, or an applied magnetic field. When this external tuning parameter reaches a critical value at 0 K, the system undergoes a phase transition between two quantum ground states, common examples of which are different forms of magnetic ordering such as a transition from a paramagnetic to a ferromagnetic or antiferromagnetic state. A generic phase diagram of a quantum critical system is illustrated in Figure 1.4.

Although by definition the critical point occurs at 0 K, proximity to the critical point gives rise to critical fluctuations of a quantum (rather than thermal) nature, whose effects are felt throughout the phase space in the vicinity of the critical point. These order parameter fluctuations alter the nature of the electronic quasiparticles and gives rise to anomalies in a number of observable properties at $T > 0$, which is sometimes called *strange metal* or *non-Fermi liquid* behavior [22].

Perhaps the most striking anomaly occurs in the heat capacity, which displays a divergent logarithmic dependence with temperature in the vicinity of the quantum critical point:

$$\frac{\Delta C}{T} \propto -\ln T \qquad 1.5$$

This is in stark contrast to the heat capacity of a Fermi liquid, where the quantity $\Delta C/T$ is constant. This behavior has been studied intensively in heavy-Fermion metals. This characteristic divergent behavior makes heat capacity measurements a useful signature of non-Fermi liquid behavior in bulk crystals. However, in thin film samples, the subject of this work, the extremely small volume of material in a thin film sample makes reliable heat capacity measurements exceedingly difficult.

The critical fluctuations also cause anomalies in the in-plane resistivity. This behavior is much more experimentally accessible in studies of thin films. In many metals the resistivity can be fit to a power law of the form

$$\rho_{XX} = \rho_0 + AT^n \qquad 1.6$$

where ρ_0 is the residual resistivity arising from defect scattering, A is the scattering amplitude, and n is a power law exponent. In a metal with weak electron-electron interactions that can be described within the framework of Fermi liquid theory, n is predicted to take on a value of 2 at low temperatures. When the system is close to a

quantum critical point the enhanced scattering off quantum fluctuations can lead to anomalous non-Fermi liquid behavior in which $n < 2$. A classic example of this occurs in the cuprate superconductors, where resistivity that scales linearly with T (n = 1) is observed over large regions of the temperature-composition phase space. This behavior is not completely understood. However, various theoretical models have been proposed which predict that the values of n will depend on both the dimensionality and the nature of the magnetic ordering in the metal [22].

Another manifestation of quantum criticality and breakdown of Fermi liquid theory that can be observed in the resistivity is enhancement of the effective mass as the system approaches the quantum critical point. The framework of Fermi liquid theory is based on the concept of quasiparticles, which are excitations that carry the same charge and spin as the non-interacting particles. The effective mass, m^*, of such quasiparticles is renormalized according to the strength of the interactions. However, near a quantum critical point the interactions become extremely large, and at some point the quasiparticle states are no longer adiabatically connected to the non-interacting system. In this case the effective mass can diverge ($m^*/m \rightarrow \infty$), which marks the breakdown of the quasiparticle concept as the renormalization connecting the quasiparticles to the non-interacting particles vanishes completely. The scattering amplitude A in Equation 1.6 for the resistivity given above is directly related to the effective mass ($A \propto m^*$). Therefore, A can serve as a useful probe of the mass enhancement phenomenon and in many correlated materials it has been

found to diverge as criticality is approached. One example of this occurs in the vicinity of the metamagnetic transition in $Sr_3Ru_2O_7$ [23], which will be the subject of Chapter 6.

1.5 Scattering Rate Separation and Two-Lifetime Transport Behavior

In standard models of transport only one scattering rate (τ) is typically considered in describing the transport properties of conventional metals. That is, the transverse Hall and the longitudinal scattering rates are assumed to be identical ($\tau_H = \tau_{xx} = \tau$). Under conditions of small applied electric field E, the current density J depends linearly on field with the conductivity tensor as the prefactor, expressed as $J_i = \sigma_{ij}E_j$. The isotropic conductivity can be expressed as

$$\sigma = \begin{pmatrix} \sigma_{xx} & -\sigma_{xy} \\ \sigma_{xy} & \sigma_{xx} \end{pmatrix} = \frac{Ne^2\tau}{m^*}\frac{1}{1+\omega_c^2\tau^2}\begin{pmatrix} 1 & \omega_c\tau \\ -\omega_c\tau & 1 \end{pmatrix}, \qquad 1.7$$

where N is the carrier density and ω_c is the cyclotron frequency given by eH/m^*. Inverting the tensor gives us an expression for the resistivity:

$$\rho = \begin{pmatrix} \rho_{xx} & -\rho_{xy} \\ \rho_{xy} & \rho_{xx} \end{pmatrix} = \frac{m^*}{Ne^2\tau}\begin{pmatrix} 1 & -\omega_c\tau \\ \omega_c\tau & 1 \end{pmatrix}. \qquad 1.8$$

The Hall coefficient measured experimentally in an applied magnetic field H is then given by

$$R_H = \frac{\rho_{xy}}{H} = \frac{1}{H}\frac{\sigma_{xy}}{\sigma_{xx}^2+\sigma_{xy}^2} \cong \frac{1}{H}\frac{\sigma_{xy}}{\sigma_{xx}^2} = \frac{1}{eN}. \quad 1.9$$

In the case of $\tau_{xx} = \tau_H$ the Hall coefficient gives us a direct measure of the carrier density N, which is what makes Hall measurements a useful technique in the electrical characterization of conventional semiconductors. To reiterate, this is based on the assumption that the Hall and longitudinal scattering rates are equivalent, leading to scattering rate cancellation with $\sigma_{xx} \propto \tau$ and $\sigma_{xy} \propto \tau^2$.

The situation in strongly correlated metals exhibiting non-Fermi liquid behavior is different. In this case, there is evidence of a *lifetime separation* phenomenon in which the Hall and longitudinal scattering rates take on distinct values. This scenario was originally explored in the context of high-T_C cuprate superconductors [24], [25]. A classic feature of cuprate superconductors is a T-linear scaling of the in-plane resistivity of the form $\rho_{xx} = \rho_0 + AT$. This carries the implication that the longitudinal scattering rate is also linear with T: $\tau_{xx}^{-1} \propto T$. On the other hand, the Hall angle, given by the reciprocal of the Hall mobility μ_H, follows a robust T^2 dependence over a wide range of temperatures, described by the expression

$$\frac{1}{\mu_H} = \cot(\theta_H) = C + \alpha T^2, \quad 1.10$$

where C is the Hall angle residual arising from chemical impurities or defects and α is the Hall scattering amplitude. Because $\mu_H^{-1} \propto \tau_H^{-1}$, the distinct temperature dependences of

the resistivity and the Hall angle imply a carrier lifetime separation ($\tau_{xx} \neq \tau_H$). Looking back the expression for the Hall coefficient, we see that

$$R_H \cong \frac{1}{H}\frac{\sigma_{xy}}{\sigma_{xx}^2} = \frac{1}{eN}\frac{\tau_H}{\tau_{xx}} \tag{1.11}$$

when lifetime separation is present. Now, instead of being dependent entirely on the carrier concentration, the Hall coefficient also depends on the ratio of the scattering rates. Because this ratio changes with temperature, the Hall coefficient will also exhibit a non-trivial temperature dependence even if the carrier concentration remains unchanged. In this case the Hall coefficient is no longer a reliable measure of the carrier concentration. If non-Fermi liquid behavior is present with $\rho(T) \propto T^n$ and $\cot(\theta_H) \propto T^2$ the Hall coefficient will be given by

$$\frac{1}{eR_H} = N\frac{\mu_{xx}}{\mu_H} = \frac{H}{e}\frac{C + \alpha T^2}{R_0 + AT^n} \tag{1.12}$$

In the case of the cuprates where the resistivity depends linearly on T, we would expect the quantity R_H^{-1} to increase linearly with T at sufficiently high temperatures, a dependence that has been experimentally observed [26]. The phenomena of two-lifetime transport has also been observed in a number of other correlated metals in proximity to a quantum critical point, notably the $V_{2-y}O_3$ system [27] and heavy Fermion metals [28]. Theories of the origin of carrier lifetime separation in these systems have been proposed, including anisotropic scattering on the Fermi surface [29], decoupling of spin and charge degrees of

freedom [24], and proximity to a quantum critical point [30]. Despite this, there is still no universally accepted microscopic theory explaining the origin of this behavior. Such an understanding could go a long way towards the development of a more comprehensive understanding of quantum criticality and related phenomena such as high-T_C superconductivity, as the robust T^2 dependence of the Hall angle and the associated lifetime separation seem to be a nearly universal features of this class of materials. A study treating the lifetime separation phenomena in correlated 2DEGs in $SrTiO_3$ quantum wells will be discussed in Chapter 4. In particular, the effect of disorder on the temperature dependence of the Hall angle and the low-temperature Hall angle residual C will be explored.

1.6 Van Hove Singularity

The density of states of a metal with a well-defined energy dispersion $E(\vec{k})$ is given by the expression

$$D(E) = \int_{S(E)} \frac{dS}{4\pi^3} \frac{1}{\left|\nabla E\left(\vec{k}\right)\right|} \tag{1.13}$$

where $S(E)$ is a surface of constant energy. Consequently, we see that when the gradient of the dispersion $\nabla E\left(\vec{k}\right)$ approaches zero on flat regions of the Fermi surface, sharp peaks or singularities in the density of states will arise. This phenomenon is known as a *Van Hove singularity*, named after the Belgian physicist Léon Van Hove who first investigated

these singularities in the 1950s in the context of the phonon density of states [31]. In three dimensions Van Hove singularities can occur when the band structure contains a local maximum, a local minimum, or a saddle point, where the derivative of the DOS is predicted to be divergent. In the two-dimensional case the DOS itself diverges logarithmically at a saddle point. Experimental evidence of Van Hove singularities can be obtained by techniques that can provide direct measures of the DOS, such as tunneling spectroscopy or angle-resolved photoelectron emission spectroscopy [32], [33].

Van Hove singularities have been observed in a number of strongly correlated materials and are now believed to be one of the fundamental features underlying many of the exotic electronic and magnetic phases observed in these materials. When the Fermi level lies close to the sharp DOS peak, the Fermi surface is especially susceptible to breakdown into ordered states. For example, Van Hove singularities can lead to divergences of the spin susceptibility $\chi(\vec{q},\omega)$ both in the intra-VHS case ($\vec{q}=0$) and the inter-VHS case ($\vec{q}=\vec{Q}_0$) where the wave vector $\vec{Q}_0$ connects two saddle points on the Fermi surface. This can lead to instability toward itinerant ferromagnetic or antiferromagnetic phases, which can take the form of spin density waves. Van Hove singularities have even been proposed to play a role in the pairing mechanism of unconventional superconductivity [34].

The position of the van Hove singularity relative to the Fermi level can be tuned via external perturbations such as an applied magnetic field, chemical doping, or gating [35], [36]. This could be used to engineer the ordered phases arising from the DOS

singularity-induced instabilities. Another route to achieving this is through modification of the band structure induced by the applied pressure. This could include chemical pressure induced by isovalent doping, uniaxial pressure, or biaxial pressure such the distortion that arises from epitaxial strain [37], [38]. In Chapter 6 an experiment in which an epitaxially strained film of the metamagnet $Sr_3Ru_2O_7$ was found to have low-temperature properties that differed significantly from the bulk will be described, likely due to the modification of the band structure and closer proximity to the Van Hove singularity [39].

1.7 Pseudogap Behavior

A pseudogap is a partial reduction of the density of states near the Fermi level. This phenomenon has been observed in a multitude of strongly correlated systems, including high-temperature cuprate superconductors [40], heavy-fermion materials [41], rare-earth nickelates [42], and cold atom systems [43]. Experimental observation of the pseudogap state can be provided by techniques that provide access to a measure of the single-particle spectral weight around the Fermi level, the most common of which are scanning tunneling microscopy (STM) and angle-resolved photoelectron spectroscopy (ARPES). The concept of a pseudogap stands in contrast to *hard gaps* (sometimes referred to as *true gaps*), in which the density of states falls to zero in a finite energy range around the Fermi level, as is the case in conventional insulators, Mott insulators, and BCS superconductors. In contrast, the pseudogap is only a partial reduction of the density of states, implying that the material retains metallic character.

The precise nature and origin of pseudogap behavior in strongly correlated metals has been the subject of research for decades. The pseudogap behavior in underdoped cuprate superconductors has been intensively studied, as some researchers believe that it may be intimately linked to the high-temperature superconducting state in the form of pre-formed Cooper pairs [44]. Others believe it is a competing electronic state with a separate origin [45]. In any case, pseudogap state is generally believed to originate from the formation of a low-temperature ordered phase driven by strong correlations, examples of which could include charge and spin density waves. The electrons contributing to the ordered phase can no longer contribute to conduction.

A related concept is the zero-bias anomaly, which is a general term for suppression of the density of states near the Fermi level resulting from the combined effect of electron-electron interactions and disorder. The reduction in electron itinerancy caused by disorder has the effect of increasing their effective Coulomb interactions, thereby enhancing correlation effects. The effect of the zero-bias anomaly is most pronounced in low dimensional systems. Boris Altshuler and Arkady Aronov published a theory of the zero-bias anomaly in 1979 [46]. They considered the problem under conditions of diffusive transport in which the scattering rate is large relative to the electron energy ($1/\tau \gg \varepsilon/\hbar$). Their results predict a dependence of the density of states of $DOS \propto V^{1/2}$ in three dimensions and $DOS \propto \ln V$ in two dimensions [47], which has been experimentally verified in a number of materials systems [48], [49].

The theory of the zero-bias anomaly was extended to insulators by Boris Shklovskii and Alexei Efros in 1975 [50]. The Efros-Shklovskii Coulomb gap is an example of a *soft gap*, which is gap-like behavior in which the density of states reaches zero precisely at the Fermi level but remains finite elsewhere. Efros and Shklovskii predicted the dependence of the density of states on bias to be parabolic in three dimensions and linear in two dimensions. These predictions have also been observed experimentally, and it has been shown that the zero-bias anomaly at the Fermi level predicted by the Altshuler-Aronov theory for metals continuously evolves into the Efros-Shklovskii Coulomb gap behavior as a metal-to-insulator transition is induced through reduction of the doping density [51]. Because of the variety of conditions under which zero-bias anomaly and Coulomb gap behavior has been observed, it is important to consider them as possibilities during studies of the electronic structure of strongly correlated metals.

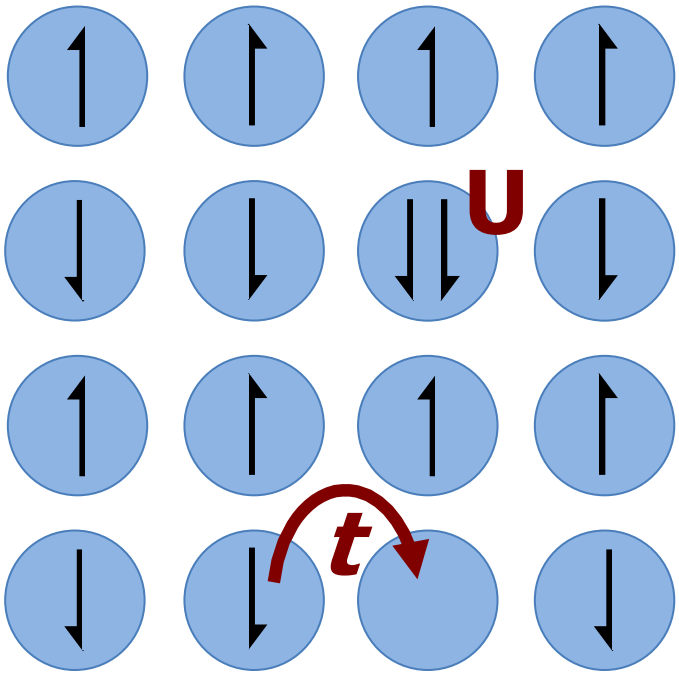

Figure 1.1 Illustration of origin of the on-site Coulomb interaction U and the hopping integral t in the lattice of a correlated material with strongly localized electrons.

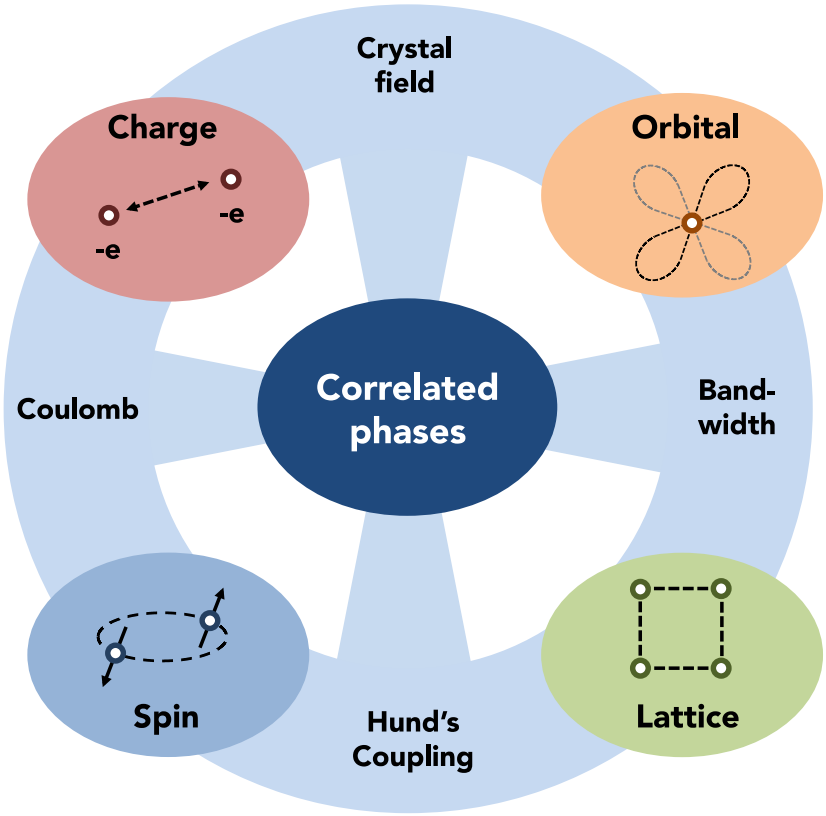

Figure 1.2 Degrees of freedom and interactions resulting from the effects of transport within narrow *d* and *f*-bands in transition metal oxides. The interplay of the degrees of freedom leads to the emergence of unusual correlated phases.

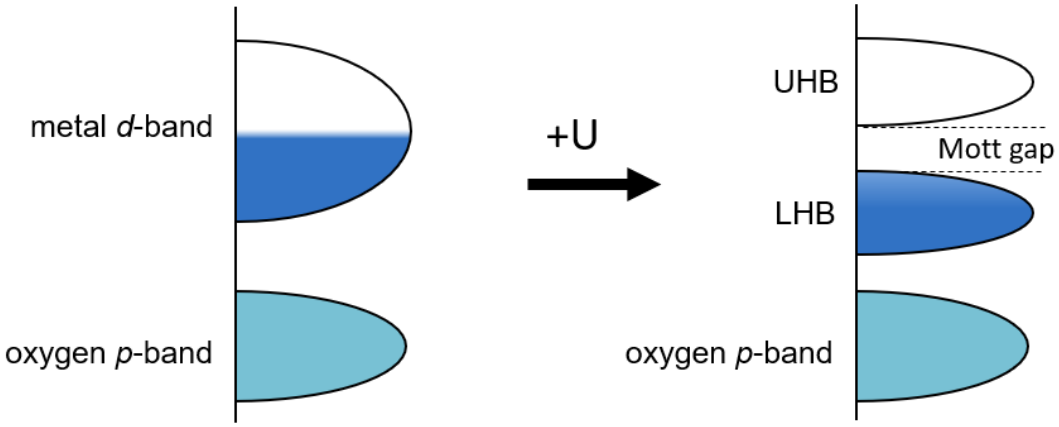

Figure 1.3. Illustration of energy levels in a Mott insulator. The band structure on the left is that of a conventional metal with a partially filled *d*-band. The addition of electron-electron interactions, characterized by U, leads to a splitting of the *d*-band into an upper Hubbard band (UHB) and a lower Hubbard (LHB) separated by a Mott gap.

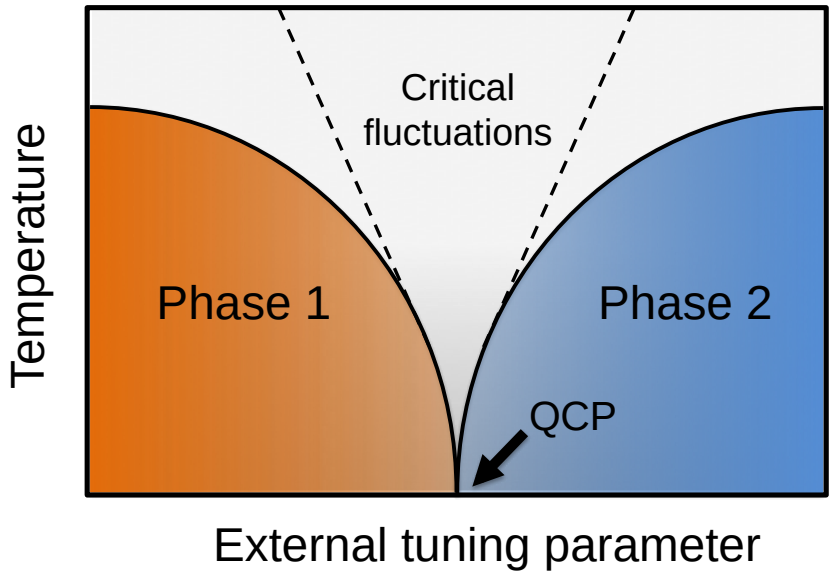

Figure 1.4 Illustration of a phase diagram of a quantum critical system. The external tuning parameter drives the system between two quantum ground states, labeled Phase 1 and Phase 2, at 0 K. Critical fluctuations in the vicinity of the phase transition give rise to observable transport anomalies at $T > 0$.

Chapter 2 Introduction to Correlated Perovskite Oxides

2.1 ABO_3 Perovskites and $SrTiO_3$

The family of perovskite oxides of the type ABO_3 (where A and B are metal cations) are an incredibly diverse class of materials whose members exhibit a vast array of structural, electronic, and magnetic properties. The unit cell of the simple perovskite crystal structure is illustrated in Figure 2.1, along with some examples of the ordered electronic and magnetic states that have been observed in this family of oxides. Each combination of A and B cations leads to perovskite compound with unique structural and electronic properties. The effect of the relative sizes of the A and B ions on the structure of the unit cell can be summarized with the Goldschmidt tolerance factor, defined as

$$t = \frac{r_A + r_0}{\sqrt{2}(r_B + r_0)}, \qquad 2.1$$

where r_A is the ionic radius of the A-site cation, r_B is the ionic radius of the B-site cation, and r_0 is the ionic radius of the anion, which would be oxygen in the case of perovskite oxides [52]. The case of $t > 1$ typically promotes a hexagonal or tetragonal crystal structure, $t \approx 1$ promotes an ideal cubic structure (as is the case in $SrTiO_3$), and $t < 0.9$ promotes orthorhombic or rhombohedral distortions, such as the $GdFeO_3$-type structure. The orthorhombic distortions tend to rotate the BO_6 octahedra relative to each other. This changes the B-O-B bond angle from its ideal value of 180°, which in turn, influences the bandwidth and the electronic properties of the material. Minute changes in the geometric distortion are correlated with a variety of physical states, such as magnetism and

ferroelectricity. For example, in the series of titanates of the type RTiO$_3$, the varying size of the R^{3+} ion when moving down the series of lanthanides La to Gd induces a change in the Ti-O-Ti bond angle from less distorted to more distorted, which is associated with a transition from antiferromagnetic to ferrimagnetic behavior [53].

Among the vast number perovskite oxides, SrTiO$_3$ perhaps remains the most well studied perovskite oxide semiconductor. SrTiO$_3$ has a nonpolar cubic structure with a lattice constant of 3.905 Å. It has an indirect band gap of 3.2 eV, centered at the Γ point. Its valence band is dominated by oxygen 2*p*-orbitals while its conduction is primarily of Ti 3*d* character [54]. Metallic behavior can be induced by doping with trivalent rare-earth ions on the Sr^{2+} site (La^{3+} is commonly used for this) or with pentavalent ions on the Ti^{4+} site (a common example being Nb^{5+}). Annealing SrTiO$_3$ in a reducing environment forms oxygen vacancies, giving rise to n-type metallic behavior. Another method of doping, to be addressed in detail in later chapters, is electrostatic doping at an interface with a polar perovskite material. This phenomenon will be introduced in the following section.

2.2 Two-dimensional Electron Gas at RTiO$_3$/SrTiO$_3$ Interfaces

Conductive two-dimensional electron gases (2DEGs) arising from polarization discontinuities at semiconductor interfaces have been intensively studied for decades. A technologically important example is the 2DEG arising at AlGaN/GaN interfaces, where the polarization discontinuity induces a highly mobile 2DEG (mobility of 1000-2000 cm^2/Vs at 300 K) with sheet carrier densities on the order of 10^{12} cm^{-2}. This is commonly

exploited in high-electron mobility transistors. In 2004 a similar phenomenon was reported to occur at polar/nonpolar interfaces between the perovskite oxides $LaAlO_3$ and $SrTiO_3$ [6]. This was followed by reports of numerous electronically and magnetically ordered phases that can emerge in the 2DEG such as superconductivity and induced ferromagnetism [7], [8], leading to a surge of interest in this system. Based on the fixed immobile positive charge in the $La^{3+}O^{2-}$ layer (formal charge of +1), one would naturally expect the transfer of ½ an electron per interfacial unit cell to the adjacent non-polar $SrTiO_3$ layer, inducing a sheet carrier density of 3.5×10^{14} cm^{-2} in the 2DEG. However, at $LaAlO_3/SrTiO_3$ interfaces these high carrier densities have not been achieved. In many cases the carrier densities are an order of magnitude less than expected based on intrinsic electronic reconstruction [55], leading to many suggestions about the relative role played by oxygen vacancies, cation disorder, and surface reconstructions [56].

In contrast, the expected sheet carrier density has been observed at all-titanate $RTiO_3/SrTiO_3$ interfaces, where *R* is either Gd or Sm [11]. The electrostatic doping mechanism for an all-titanate interface is illustrated in Figure 2.2. The high sheet carrier density and high mobility of the 2DEG at low temperatures has enabled detailed studies of its transport properties and underlying physics, such as analysis of Shubnikov-de-Haas oscillations in strong magnetic fields and elucidation of its sub-band structure [57], [58].

2.3 Quantum Criticality in $SrTiO_3$ Quantum Wells

The electrostatic doping introduced in Section 2.2 was taken a step further through the growth of RTiO$_3$/SrTiO$_3$/RTiO$_3$ (R = Gd, Sm) quantum well structures [59]. The two back-to-back RTiO$_3$/SrTiO$_3$ interfaces in such a structure, illustrated in Figure 2.3, induce extremely high carrier densities of 7×10^{14} cm^{-2}, a situation that enhances the electron-electron Coulomb repulsions. Additionally, the electrostatic confinement provided by the band offsets of RTiO$_3$ and SrTiO$_3$ confine the carriers to the thin wells, whose thickness can be controlled down to monolayer dimensions during growth with MBE. This further enhances the correlation effects, which has led to the observation of phenomena such as proximity-induced magnetism and metal-insulator transitions in thin wells [59]–[61]. Detailed transport studies of SrTiO$_3$ wells embedded in both SmTiO$_3$ and GdTiO$_3$ barrier layers have been carried out. Both of these materials are d^1 Mott insulators with orthorhombic GdFeO$_3$-type structural distortions (space group *Pbnm*). The differences between these two materials are found in both the degree of distortion of the oxygen octahedra (as quantified by the deviation of the angle between three successive A-site cations from 180°), and the nature of magnetic ordering. Pure SmTiO$_3$ possesses a deviation angle of 14.7°, while GdTiO$_3$ is slightly more distorted with a deviation of 15.7° [53]. SmTiO$_3$ orders antiferromagnetically at a Néel temperature of 50 K, while GdTiO$_3$ is a ferrimagnet with a Curie temperature of 30 K.

The behavior of the in-plane sheet resistance differs as a function of quantum well thickness in the two barrier materials. It was found that quantum wells in $SmTiO_3$ remain metallic all the way down to a quantum well consisting of only a single layer of SrO (the thicknesses of the quantum wells will be specified in terms of the number of SrO layers they contain). In $GdTiO_3$ barriers, metallic behavior is observed in thick wells but a metal-to-insulator transition is observed in thin quantum wells at or below a critical thickness of 2 SrO layers. A study of the structure found evidence of a symmetry-lowering structural distortion in the $GdTiO_3$-embedded wells at this thickness, suggesting that the greater distortion of the octahedral tilts in the $GdTiO_3$ can couple into the structure of the $SrTiO_3$ [61]. In 2 SrO layer thick wells a deviation angle of roughly 6° was found in the $GdTiO_3$-embedded well, while it was only 3° in $SmTiO_3$-embedded well. The abrupt transition of the behavior of the resistance suggests that Mott-Hubbard-like physics is at play. The decreased Ti-O-Ti bond angle in the more distorted wells likely reduces the Ti 3*d* bandwidth and plays a role in driving the critical transition.

The most striking feature of this quantum well system is the observation of non-Fermi liquid behavior in the in-plane transport [62]. This was evidenced by power law exponents n in the sheet resistance $R_S = R_0 + AT^n$ which differed from the Fermi liquid value of 2. In particular, $n \approx 5/3$ behavior was commonly observed. When the transport coefficients R_S and the Hall coefficient $(eR_H)^{-1}$ are mapped out as a function of quantum well thickness t_{QW}, the patterns point to the existence of a quantum critical point at a critical well thickness of t_{QW} = 5 SrO layers. This includes both a discontinuity in the

temperature power-law exponent n and a divergence in the low-temperature Hall coefficient, likely arising from critical fluctuations leading to a divergent Hall angle residual near this thickness [63]. Enhanced scattering off of the critical fluctuations of the order parameter can explain the deviation from T^2-behavior of the resistivity. The microscopic origin of the quantum critical behavior is still an open question. Considering the magnetic nature of the barriers, a magnetic origin seems likely. This is supported by the observation of induced ferromagnetism in $GdTiO_3$ wells and evidence of itinerant antiferromagnetism in $SmTiO_3$ wells near t_{QW} = 5 SrO layers, evidence that the magnetic ordering in the barrier layers can readily couple into the conductive well [60], [64]. Phase diagrams demonstrating the critical behavior of these two systems based on the available experimental evidence are illustrated in Figure 2.4. Studies of this quantum well system will be extended in Chapters 3 and 4 of this work.

2.4 $Sr_{n+1}Ru_nO_{3n+1}$ Ruddlesden-Popper Series

The perovskite oxide materials discussed to this point have been limited to the simple perovskite structure, in which the network of interconnected BO_6 octahedra is effectively infinite throughout the lattice. An additional layer of complexity is added in layered perovskite compounds, in which the thickness of adjacent layers of BO_6 octahedra, separated by layers of A^{2+} cations, is finite. Reducing the thickness of the BO_6 layers effectively reduces the dimensionality of the transport behavior from three-dimensional

toward the two-dimensional limit, a situation which often leads to even stronger correlation effects and more complex electronic and magnetic phases.

A material system in which this effect is at play is the Ruddlesden-Popper series of layered strontium ruthenate materials, in which the variable n is used to specify a member of the series with the chemical formula $Sr_{n+1}Ru_nO_{3n+1}$. All members of this series are metallic, with conduction occurring within the adjacent RuO_6 layers. For example, n = 1 corresponds to the phase with the formula unit Sr_2RuO_4, where the conducting layers only contain a single RuO_6 layer. Increasing n increases the thickness of the RuO_6 layer and the itinerancy of the electrons. This is illustrated in Figure 2.5 for several members of the series. The limit of $n = \infty$ corresponds to the simple perovskite $SrRuO_3$, in which the RuO_6 octahedra are interconnected throughout the entire crystal.

This series of perovskite oxides hosts many fascinating low-temperature ordered phases. The formation of these phases is driven by both electron correlations that affect transport in the Ru 4*d* bands and the shape of the Fermi surface itself. For example, Sr_2RuO_4 displays unusual p-wave superconductivity below a critical temperature of T_C = 1.5 K, in which the spin-triplet nature of the Cooper pairs and the ferromagnetic fluctuations hint that the spins play an important role in the unconventional pairing mechanism [65], [66]. The n = 2 member $Sr_3Ru_2O_7$, a double layer perovskite, exhibits a quantum critical metamagnetic transition, nematic order, and spin density wave phases arising at low temperatures [67]–[69]. The $n = \infty$ member $SrRuO_3$ is an itinerant

ferromagnet with a Curie temperature of T_C = 160 K, making it useful as an electrical contact in certain types of magnetic devices [70].

The band structure is believed to play a major role in many of these phenomena. One of the underlying features in the band structure, observed in both Sr_2RuO_4 and $Sr_3Ru_2O_7$, is a saddle point of vanishing curvature on the quasi-two dimensional Fermi surface [71], [72]. This leads to a Van Hove scenario in which there is a divergence of the density of states near the Fermi level, making the Fermi surface susceptible to breakdown into ordered electronic or magnetic states. As a result of this, small perturbations of the Fermi surface can lead to dramatic changes in the electronic and magnetic properties. This has been explored via chemical substitution of the Sr^{2+} by La^{3+}, which has been found to enhance magnetism by increasing the Fermi level [73]. Another route to perturbing the Fermi surface is via applied pressure, which can either be uniaxial, hydrostatic, or biaxial, such as the stress imposed by epitaxial strain during growth on a lattice mismatched substrate. The growth of the $Sr_{n+1}Ru_nO_{3n+1}$ series by a hybrid molecular beam epitaxy will be introduced in Chapter 5, which has the potential to overcome some of the difficulties traditionally encountered during thin film growth of the ruthenates with conventional sources of ruthenium. In Chapter 6 a study of the transport and magnetic properties of epitaxially strained thin films of $Sr_3Ru_2O_7$ will be discussed, where it was found that the low temperature ordered phases were dramatically modified by epitaxial strain.

2.5 Hybrid Molecular Beam Epitaxy Growth of Perovskite Oxides

Among the various thin film deposition techniques, molecular beam epitaxy (MBE) stands alone in its unmatched control of film purity, composition, and layer thickness during heterostructure growth. Several features inherent to the MBE technique contribute to this. The energies of the particles reaching the substrate from the thermally sublimated source are extremely low, typically on the order of 0.1 eV [74]. This stands in contrast to the energies involved in pulsed laser deposition and sputtering deposition, where the energies can range from 1-10 and 10-100 eV, respectively, which can contribute to the formation of extended defects. Another advantage is that the technique takes place in a growth chamber pumped to ultra-high vacuum (UHV) conditions, with base pressures on the order of 10^{-10} Torr routinely being achieved with the use of a liquid nitrogen-cooled cryopanel. This reduces film contamination arising from the incorporation of background impurities present in the chamber, which can be an issue during metal-organic chemical vapor deposition.

The large mean free paths possible in the UHV environment during growth (1-10 km) enables the delivery of very precise quantities of source material to the substrate in the form of a molecular beam. The precise control over growth rate, which can be controlled at rates below 1 Å/s, enables control of layer thicknesses down to atomic dimensions. Additionally, atomically abrupt interfaces between two materials can be grown, allowing for precise engineering of transport properties for device applications. A prominent

example of a technology that was made possible by this is the high electron mobility transistor. The use of a lattice-mismatched substrate allows for the growth of epitaxially strained films with lattice constants that differ from the nominal bulk values. This perturbation of the lattice, in turn, alters the band structure and therefore the transport properties of the film, opening even more avenues to engineer transport properties for device applications. The highly precise and tunable nature of the growth process also make MBE ideal for the study of low-temperature transport phenomena and emergent phases driven by strong electron correlations, where subtle structural aspects of the lattice directly couple into the electronic properties. All of the correlated oxide materials discussed in this thesis were grown with this powerful technique.

Although epitaxial growth with MBE provides the inherent advantages of high purity, low intrinsic defect concentrations, and monolayer control over layer thickness described above, control of stoichiometry is a more complicated issue. MBE was originally used for the growth of III-V semiconductors, a prototypical example of which is GaAs. The great success of III-V MBE growth can largely be attributed to the very wide thermodynamic growth window of this class of materials [75]. The thermodynamics of the reaction occurring at the substrate surface to form the solid film is a fundamental consideration in epitaxial growth. For example, during the growth of GaAs, the vapor pressure of As is sufficiently high to allow excess As to simply desorb from the Ga-rich growth surface. Only the As needed to react with the Ga in a 1:1 ratio will remain, with the end result being a pure stoichiometric GaAs film. This self-regulating process allows

for the extremely low defect densities possible in MBE-grown III-V materials, which in turn enables the high electron mobilities necessary for device applications.

In contrast, the thermodynamic growth window for perovskite oxides is extremely narrow relative to that of the III-V semiconductors. The vapor pressures of the A and B site metals in the ABO_3 perovskite structure tend to be very low, so the sticking coefficients are near unity. It is instructive to consider the prototypical example of $SrTiO_3$. The temperatures necessary to reach a vapor pressure of 1 Torr of Sr and Ti are 750 and 2200 °C, respectively. In contrast, As would only be needed to be heated to near 400 °C. In the case of Sr and Ti, excess metal on the growth surface cannot readily desorb into the vacuum chamber. Rather, it is likely to incorporate into the film as non-stoichiometry related defects such as inclusions of different phases or vacancies of the cation present in deficient quantities. If we consider the fact that a typical MBE source only has flux control of about 0.1 to 1% over the course of a typical growth, this could easily result in defect densities in the range of $10^{20} – 10^{21}$ cm^{-3}, which would severely impact the transport properties and render the film useless in any electronic application.

A route around this fundamental challenge imposed by thermodynamics is offered by the technique of hybrid molecular beam epitaxy. In this method, a volatile precursor molecule is used in lieu of one or more of the conventional metallic sources. An example is the use of the metal-organic compound titanium tetra-isopropoxide (TTIP) in place of metallic Ti. TTIP has a vapor pressure around 1 Torr at 50 °C, which is many orders of magnitude higher than Ti. The TTIP precursor (or similar volatile precursor) is delivered

to the chamber via a custom-built gas inlet system in which a linear leak valve and a capacitive pressure sensor are connected in a feedback loop to deliver precisely controlled quantities of precursor gas to the growth chamber. The stainless steel tubing of the inlet system is typically heated to prevent condensation of the precursor on the tubing walls. The precursor is delivered to the growth chamber via a heated gas injector with a showerhead-type nozzle to ensure a uniform distribution of molecules.

When the precursor reaches the substrate surface it decomposes into TiO_2 and a variety of hydrocarbon byproducts. The TiO_2 reacts with SrO on the growth surface to form solid $SrTiO_3$, while the volatile hydrocarbons desorb from the hot surface and are pumped out of the growth chamber. It has been demonstrated that the use of the TTIP precursor opens up a "stoichiometric growth window" in which the stoichiometry of the film is self-regulating, similar to the case of GaAs discussed above [76], [77]. Because of the high vapor pressure of the TTIP molecule, excess TTIP can easily desorb from the growth surface rather than incorporating into the film in the form of defects. Additionally, because the Ti^{4+} cation is already bonded to four oxygen atoms in the TTIP molecule and initially decomposes to form TiO_2, the precursor acts as an additional source of oxygen during growth. This assists in preventing oxygen deficiency in the film. In fact, use of the TTIP precursor allows for the growth of perovskite oxides even without an external oxygen source. The wide growth window opened up by the precursor minimizes the creation of non-stoichiometry-related defects in the film. As a consequence, homoepitaxial $SrTiO_3$ films with record electron mobilities exceeding 50,000 cm^2/Vs have been demonstrated using this approach [78], [79].

Since the introduction of the use of TTIP as a source of Ti for the growth of perovskite titanates, additional precursor molecules have been explored to supply the B-site cation flux during the growth of ABO_3-type oxides. Examples include the use of vanadium oxytriisopropoxide for the growth of vanadates [80], hexamethylditin for the growth of the stannates [81], and the use of the inorganic precursor ruthenium tetroxide for the growth of compounds in the strontium ruthenate Ruddlesden-Popper series [39], [82], a subject discussed in-depth in Chapter 5 of this work.

A schematic illustrating the setup of a hybrid MBE chamber is shown in Figure 2.6. During the growth of $SrTiO_3$, a conventional high-purity metallic Sr charge is evaporated from an effusion cell, a radio frequency oxygen plasma source provides an oxidizing background environment, and the volatile TTIP precursor supplies the source of Ti. The three elements combine on the substrate (typically heated to around 900 °C as measured by a thermocouple mounted behind the sample) to form the solid $SrTiO_3$ thin film. Real time characterization of the film is made possible by an in-situ reflection high-energy electron diffraction (RHEED) system, which provides information about the smoothness of the film surface, the in-plane lattice constant, and surface reconstructions. Chemical species present in the growth chamber can be identified with a residual gas analyzer. This is especially relevant when using chemical precursors, which can decompose to multiple gaseous fragments at sufficiently high temperatures.

MBE is a powerful growth technique with the ability to synthesize highly pure single crystal thin films with ultra-low defect densities. The control it offers over

composition, thickness, and epitaxial strain makes it an ideal technique to explore fundamental questions in materials science. In the following chapters, several studies in which this technique was used to carry out detailed and systematic studies to address outstanding issues in the field of strongly correlated electronic materials will be discussed.

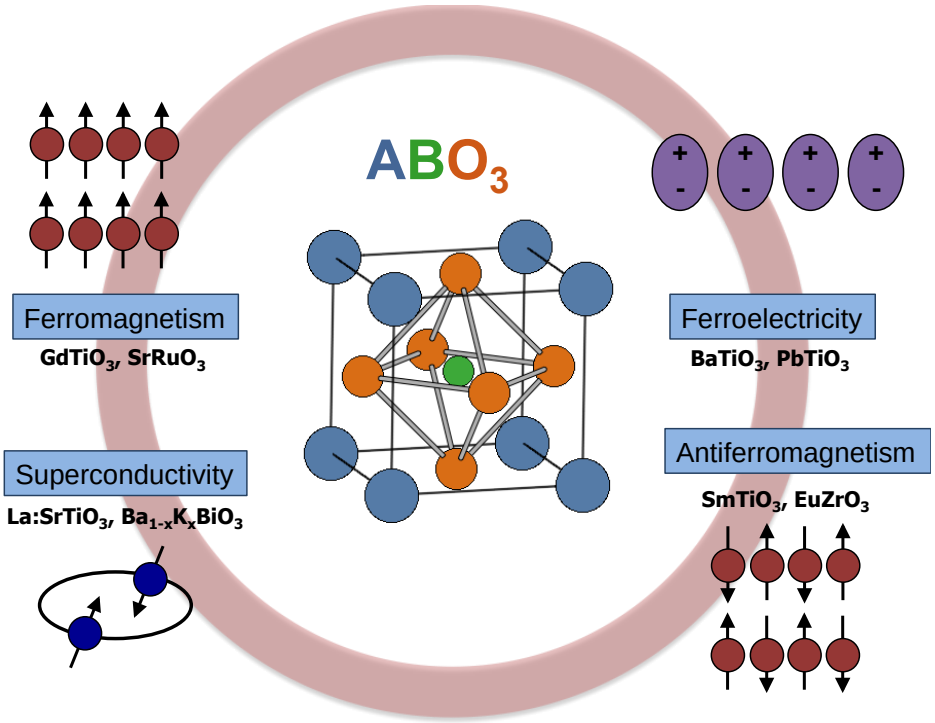

Figure 2.1 ABO_3 perovskite crystal structures with examples of electronic and magnetic ordering phenomena that can be found in this large family of materials.

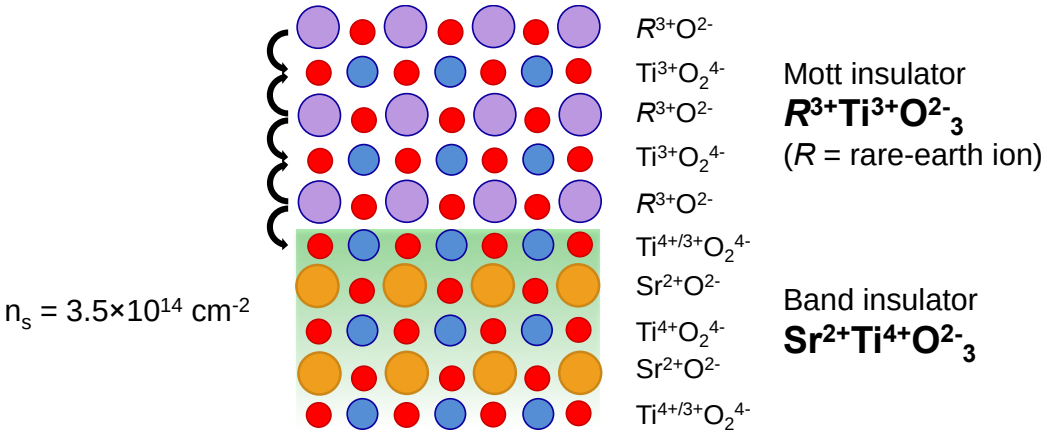

Figure 2.2 Illustration of nonpolar/polar perovskite oxide interface. The fixed positive charge in the initial $R^{3+}O^{2-}_2$ layer is compensated by a high-density mobile 2DEG in the nonpolar $SrTiO_3$ layer.

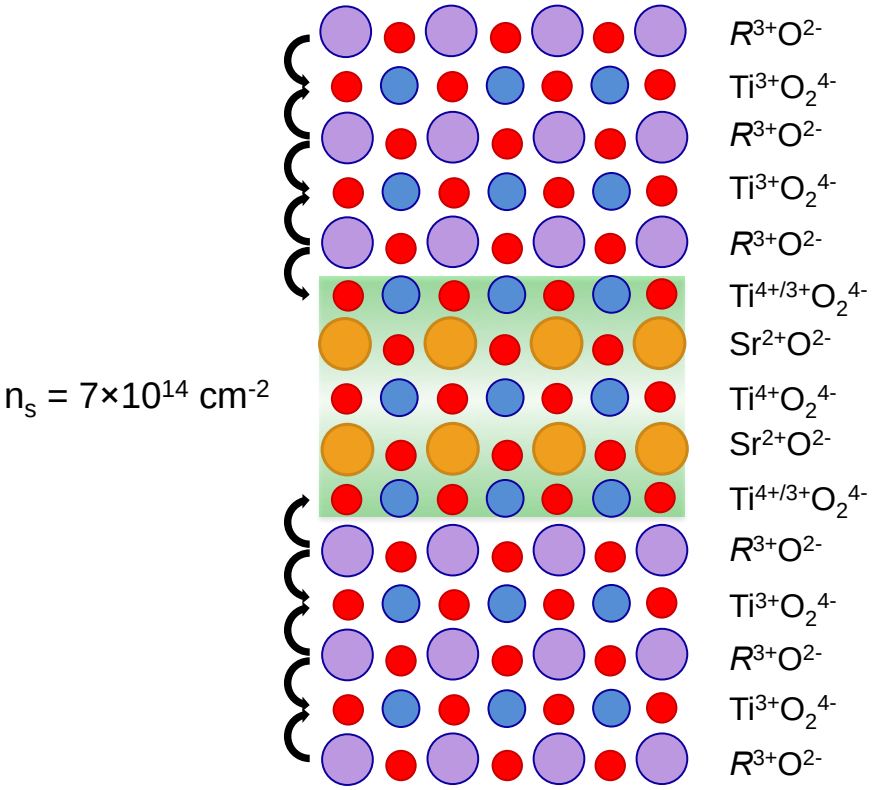

Figure 2.3 Schematic of an RTiO$_3$/SrTiO$_3$/RTiO$_3$ (R = Gd, Sm) quantum well structure. The doping induced by the polar discontinuity at each interface leads to extreme sheet carrier densities near 7×10^{14} cm^{-2}, a situation enhancing strong electron correlations.

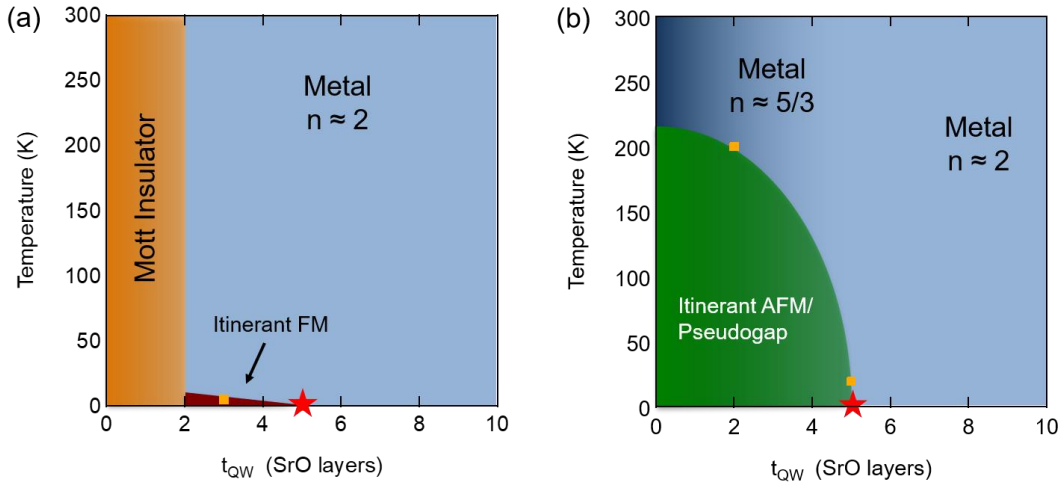

Figure 2.4 Phase diagrams of RTiO$_3$/SrTiO$_3$/RTiO$_3$ quantum well systems with R = Gd, Sm. (a) In GdTiO$_3$-embedded wells a metal-to-insulator transition is observed in thin wells. Fermi liquid-like scattering behavior is observed throughout the metallic phase with $n \approx 2$. Induced itinerant ferromagnetic order has been observed at low temperatures in wells under 5 SrO layers thick. (b) In SmTiO$_3$-embedded wells metallic behavior is seen at all well thicknesses with non-Fermi liquid ($n \approx 5/3$) observed below 5 SrO layers. An itinerant antiferromagnetic phase leading to a pseudogap state is seen at low temperatures. In both systems divergences in the transport coefficients and the emergence of itinerant magnetic phases hint at the existence of a quantum critical point at a thickness of 5 SrO layers, marked by the red star.

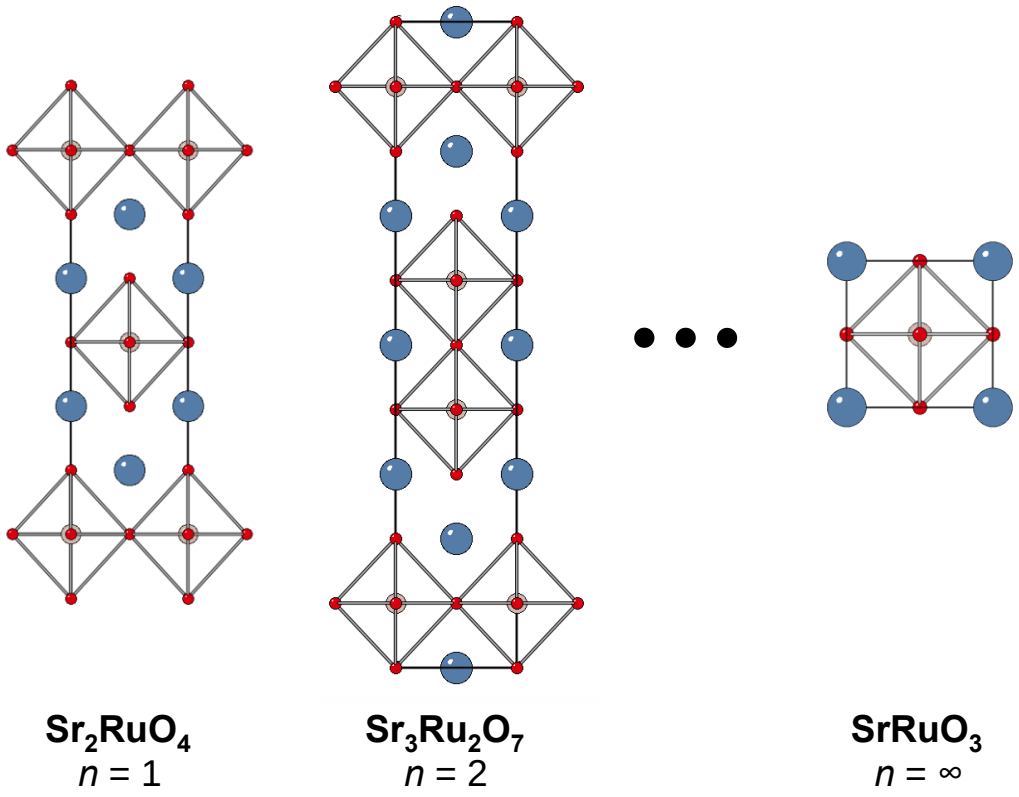

Figure 2.5 Layered structure of the $Sr_{n+1}Ru_nO_{3n+1}$ Ruddlesden-Popper series. Increasing n increases the thickness of adjacent layers of RuO_6 octahedra (marked by the grey diamonds) in which metallic transport takes place.

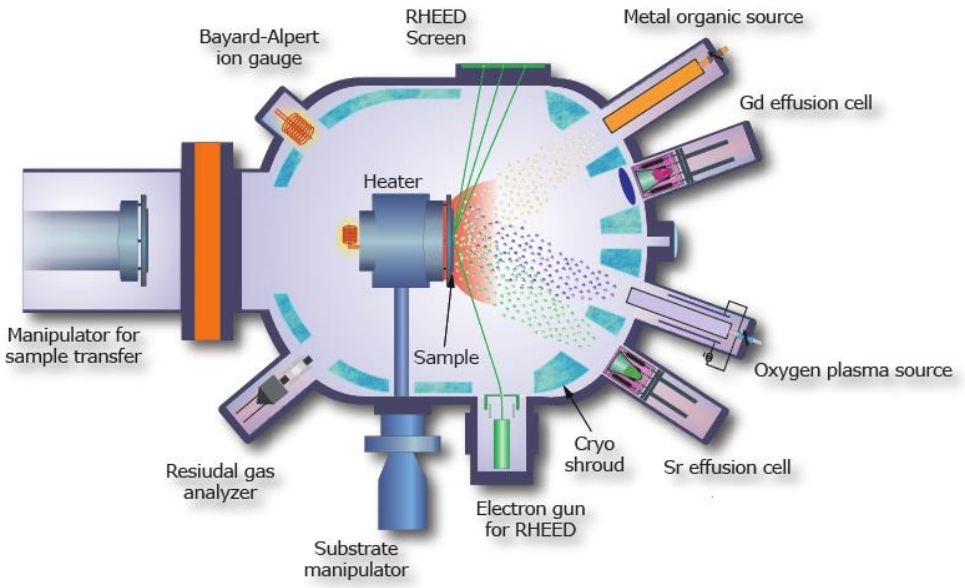

Figure 2.6 Schematic illustration of a hybrid MBE growth chamber used for the growth of perovskite oxides. One of the metal cations is delivered in the form of a volatile precursor.

Chapter 3 Pseudogaps and Emergent Phases in $SrTiO_3$ Quantum Wells

3.1 Introduction

The atomic-dimension smoothness and control of layer thickness offered by MBE make it an excellent technique for the study of electron correlation physics in low-dimensional metallic systems. An example of such a system is the correlated two-dimensional electron gas that arises at interfaces between the band insulator $SrTiO_3$ and the Mott insulating rare-earth titanates $RTiO_3$ (R = Sm, Gd), where the interfacial charge is induced by a polar discontinuity as introduced in Section 2.2. In $RTiO_3/SrTiO_3/RTiO_3$ quantum well structures with two back-to-back interfaces, sheet carrier densities of 7×10^{14} cm^{-2} can be realized. The result is a metallic, electrostatically confined, strongly correlated 2DEG in the $SrTiO_3$ well layer. Previous studies of the transport properties of this quantum well system, detailed in Section 2.3, revealed evidence for a quantum critical point near a quantum well thickness of 5 SrO layers for wells embedded in both antiferromagnetic $SmTiO_3$ and ferrimagnetic $GdTiO_3$ barriers [62], [63]. In this system the non-thermal external tuning parameter that dictates proximity to the quantum critical point is the quantum well thickness. The evidence for criticality at this thickness includes a discontinuity in the power law exponent of the temperature dependence of the resistivity, a divergence of the hall coefficient R_H, and two-lifetime transport behavior [63]. Although strong evidence of quantum criticality in this system exists, its microscopic origin is not clear.

A commonly encountered phenomenon in systems in close proximity to a quantum critical point is a pseudogap in the density of states, introduced in Section 1.7. The structure of the pseudogap provides unique information about the underlying electronic correlation effects that give rise to it. In particular, the width of the pseudogap provides information about the effective binding energy of the ordered phase giving rise to the pseudogap. Additionally, the presence or absence of coherence peaks at energies just above the gap provides information about whether or not well-defined coherent quasiparticle states emerge from the ordering. An accurate picture of pseudogap behavior is critical in obtaining a comprehensive understanding of the physics of quantum criticality and emergent correlated phases.

The most common technique for probing the density of states of such a system is scanning tunneling microscopy. In such an experiment the tunneling current between a sharp metallic probe and the metallic surface of the sample is measured as the driving bias of the tip is swept at a particular location on the sample. The differential conductance of the tunneling current, dI/dV, then gives a direct measure of the single-particle density of states at that location [83]. This technique has long been used in studies of the pseudogap state in the cuprates. Major limitations of this technique are that it only probes information about the electronic structure right at the surface of a sample and its high sensitivity to contamination, necessitating a method of obtaining an ultra-clean metallic surface. This is often achieved by *in-situ* cleaving of a bulk crystal, but this is not possible in some cases.

Due to the insulating barrier layer on the surface of the RTiO$_3$/SrTiO$_3$/RTiO$_3$ quantum well structure, STM-based tunneling spectroscopy is impossible. Another route to investigating the density of states that circumvents this issue is the fabrication of tunnel junction devices. The fabrication of such a device involves the use of a series of photolithography, deposition, and etch steps to form Ohmic contacts to the underlying correlated metal. A tunnel barrier grown on top of the correlated metal and the deposition of a top gate contact then allow a tunneling current to be driven into the underlying metal. In this manner one can measure the differential conductance (dI/dV) and obtain a direct measure of the electronic density of states. A classic example of this is the use of thin Al_2O_3 tunnel barriers to measure the superconducting gap of a lead electrode by Ivar Giaever in 1960 [84].

In this study we will detail the use of this tunnel junction technique to explore the electronic structure and pseudogap behavior of a series of correlated 2DEGs in $SrTiO_3$ quantum wells of various thicknesses embedded in both $SmTiO_3$ and $GdTiO_3$ barriers. A precise and systematic study was carried out to provide insight into how emergent ordered phases in such strongly correlated systems evolve as a function of dimensionality, the magnetism of the barrier layers, and the degree structural distortion. This is made possible by the precision of the MBE growth technique and the simplicity and tunability of this quantum well system.

3.2 Fabrication of Tunnel Junction Devices

A series of quantum wells with the structures $SmTiO_3/SrTiO_3/SmTiO_3$ and $GdTiO_3/SrTiO_3/GdTiO_3$ with $SrTiO_3$ well thicknesses of 0.8, 2.0, and 4.0 nm were grown on single crystal $(LaAlO_3)_{0.3}(Sr_2AlTaO_6)_{0.7}$ substrates. The quantum well thicknesses will be specified in terms of the number of adjacent SrO planes contained in the well, which would be 2, 5, and 10 SrO layers for the thicknesses listed above. Following the growth of each quantum well structure an epitaxial 3 nm thick layer of $SrZrO_3$ was grown on top *in-situ*. The high resistivity and relatively wide bandgap of 5.6 eV of $SrZrO_3$ make it an excellent tunneling barrier. Tunnel junction devices were fabricated following growth. An initial photolithography step was used to pattern and deposit Pt top contacts of dimensions 100×350 μm^2 using an electron beam evaporator. The high work function of Pt helps to prevent the direct injection of current into the device, improving the signal from the tunneling current. This was followed by a second photolithography step to pattern the ohmic contacts. A short etch in a buffered HF solution was used to remove the $SrZrO_3$ barrier, followed by the deposition of 40 nm thick Ti contacts. This was followed by the deposition of 400 nm thick gold pads on top of the Ti to facilitate wire bonding. A schematic of the final tunnel junction device is shown in Figure 3.1. Following fabrication of the tunnel devices a Keithley 2400 Source Meter was used to obtain the current-voltage ($I-V$) curves. Various bias ranges and sweep rates were collected to ensure reproducibility of the results. The differential conductance, dI/dV, was calculated by numerical differentiation.

The contacts between the Ti pads and the underlying 2DEGs in the $SrTiO_3$ wells were found to remain ohmic down to 2 K. This is facilitated by both by the low work function of Ti and the extremely high sheet carrier density in the underlying quantum well. Current-voltage sweeps collected between ohmic contacts deposited on a 2 SrO layer thick quantum well embedded in $SmTiO_3$ are shown in Figure 3.2 (a), with the corresponding conductance shown in Figure 3.2 (b). The $I - V$ curves, which remain linear down to 2 K, demonstrate that the contacts remain ohmic. Furthermore, the flat conductance characteristics demonstrate that the features observed in the tunneling measurements described in the following sections cannot be ascribed to non-linearities stemming from the contacts.

3.3 Tunneling Results

The raw differential conductance spectra are plotted for the quantum wells embedded in $SmTiO_3$ in Figure 3.3 (a)-(c). Symmetric reductions in the density of states centered on the Fermi level (zero bias) are present for all three thicknesses at low temperatures. The non-zero density of states at the Fermi level is consistent with prior measurements revealing that $SrTiO_3$ quantum wells embedded in $SmTiO_3$ remain metallic at all thicknesses, even down to a quantum well consisting of only a single layer of SrO [61]. The depth of the gap is most pronounced in thinner quantum wells and at low temperatures. The raw conductances of the quantum wells embedded in $GdTiO_3$ are shown in Figure 3.3 (d)-(f). The behavior at thicknesses of 5 and 10 SrO layers is rather similar

to the $SmTiO_3$-embedded wells, with a symmetric reduction of the density of states around the Fermi level with similar dependences on well thickness and temperature. At 2 SrO layers, however, a marked difference is seen, with the conductance of the $GdTiO_3$-embedded well reaching zero at the Fermi level. This reflects prior transport measurements revealing a metal-to-insulator transition in $GdTiO_3$ at well thicknesses of 2 SrO layers and fewer. This is likely the result of a symmetry-lowering structural distortion in the $SrTiO_3$ well arising from coupling to the distorted TiO_6 octahedral structure in the $GdTiO_3$ layers, which has been studied quantitatively using TEM [61]. No such distortion was seen in $SmTiO_3$-embedded wells, reflecting the less-distorted structure of $SmTiO_3$.

Improved resolution of features in the conductance spectra can be realized through the use of the normalized conductance, defined as the quantity $(I/V)^{-1}(dI/dV)$ (equivalent to $d\ln(I)/d\ln(V)$). This technique is commonly used in the interpretation of tunneling spectroscopy data [86]–[88]. This quantity minimizes background features that vary slowly with the applied bias. The normalized conductances for the $SmTiO_3$-embedded wells are plotted Figure 3.4 (a)-(c). The normalized signal in the 10 SrO layer thick well is featureless with no obvious pseudogap at any temperature (the small discontinuity at 0 V originates from the differentiation), which is the expected behavior for conventional metallic behavior. A clear pseudogap state emerges in the 5 SrO layer thick well as the temperature is reduced below 20 K. In the thinnest well of 2 SrO layers the pseudogap behavior is most pronounced, becoming apparent below 200 K. Additionally, we begin to see an increase in the signal just outside of the pseudogap at both negative and

positive biases, with defined peak structures becoming apparent near 10 K. This can be described as the onset of coherence peaks with an energy gap 2Δ of approximately 65 meV.

3.4 Discussion

The differences in the evolution of the pseudogap behavior in the quantum wells embedded in the two different barrier materials provide insight into how the barrier influences the physics of the electron correlations, and in particular the important role of the nature of the magnetic ordering. In the thinnest $SmTiO_3$-embedded quantum well, the pseudogap is accompanied by the onset of coherence peaks just outside of the pseudogap at temperatures below 10 K. This behavior usually marks emergence of a coherent long-range phase with a well-defined energy. It is important to note that coherence peaks have been observed to accompany some, but not all, of the pseudogap phases observed in other strongly correlated systems [89], [90]. Considering the antiferromagnetic nature of the $SmTiO_3$ barrier ($T_N = 50\ K$), it seems likely that the pseudogap behavior and coherence peaks originate from an incipient itinerant antiferromagnetic phase, which is often associated with spin density wave order. It is well established that spin fluctuations can give rise to pseudogap behavior [91]. This is supported by recent muon spin relaxation and polarized neutron reflectometry measurements of this quantum well system which found evidence of the onset of quasistatic magnetic correlations under the same conditions in which the pseudogap is observed in the present study [64]. Magnetic correlations, as evidenced by an enhanced depolarization rate, were observed in a 5 SrO layer thick

quantum well below 20 K but were absent in a 10 SrO layer thick well. Polarized neutron reflectometry measurements of a 2 SrO layer thick well confirmed the absence of net magnetization in the well, leaving itinerant antiferromagnetic order as the likely origin. Adding to this, dynamical mean field theory calculations of the electronic structure of $SrTiO_3$ wells in $SmTiO_3$ predicted a loss of spectral weight in the 2DEG due to coupling between the antiferromagnetic fluctuations in the $SmTiO_3$ barrier and the conduction electrons [92]. The presence of coherence peaks are consistent with the fact that fluctuations of antiferromagnetic order, in contrast to ferromagnetic order, usually only affect certain regions of the Fermi surface [91]. The conditions of low temperature and reduced but finite phase space for scattering may promote the emergence of the coherent phase.

In contrast, the quantum wells embedded in the ferrimagnetic $GdTiO_3$ barrier show no evidence of coherence peaks, as seen in the comparison in Figure 3.5. Instead, continual reduction of the quantum well thickness induces a symmetry-lowering structural transition and the onset of a true gap in the density of states. This is accompanied by insulating in-plane behavior of the resistivity as observed in prior studies. The absence of coherence peaks suggests that no well-defined long-range coherent phases emerge during the transition to the insulating state. The ferrimagnetic character and more distorted structure of the $GdTiO_3$ barrier layers likely play a role. Previously, $GdTiO_3$ barriers have been found to induce itinerant ferromagnetism in the confined 2DEG via exchange coupling [60]. Ferromagnetic order in a metal is known to affect the entire Fermi surface, thereby completely affecting the phase space in which well-defined quasiparticle excitations could

exist and suppressing the emergence of coherence peaks. Taking into account the symmetry-lowering distortion that occurs in wells in $GdTiO_3$, the results also support the idea that the strengths of the electron-phonon coupling and Coulomb interactions influence the evolution of the pseudogap behavior, perhaps by promoting short-range order.

Finally, we note that the pseudogap state observed in this system is not related superconductivity, as no evidence of superconductivity has been observed at any temperature. This supports the idea that pseudogap behavior is a general feature of unconventional metallic systems in the vicinity of a quantum critical point rather than being directly related to a superconducting pairing mechanism. Instead, it is more likely that the origin of pseudogap behavior lies in the formation of low-temperature ordered phases driven by strong correlations.

In conclusion, we have demonstrated the utility of the fabrication of planar tunnel junction devices in performing tunneling spectroscopy measurements of correlated quantum well systems. This is especially relevant in cases where the use of STM is made impossible by the presence of an insulating barrier on the surface. Tunneling spectroscopy measurements of both $SmTiO_3$ and $GdTiO_3$-embedded wells of various thicknesses revealed the onset of pseudogap behavior. Coherence peaks emerged in the wells in antiferromagnetic $SmTiO_3$, while the wells in ferrimagnetic $GdTiO_3$ showed pseudogap behavior with no coherence before evolving into an insulating state. The results highlight the importance of incipient magnetic order and the strength of electron-lattice coupling in the evolution of ordered phases in correlated materials.

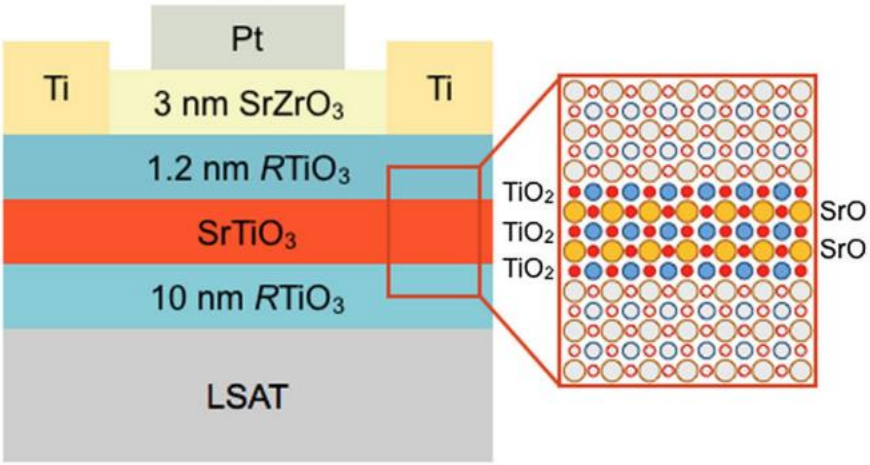

Figure 3.1 Schematic of the tunnel junction devices used to perform tunneling spectroscopy measurements. Reprinted with permission from P. B. Marshall, E. Mikheev, S. Raghavan, and S. Stemmer, Physical Review Letters 117, 046402 (2016), Copyright 2016 by the American Physical Society (Ref. [85]).

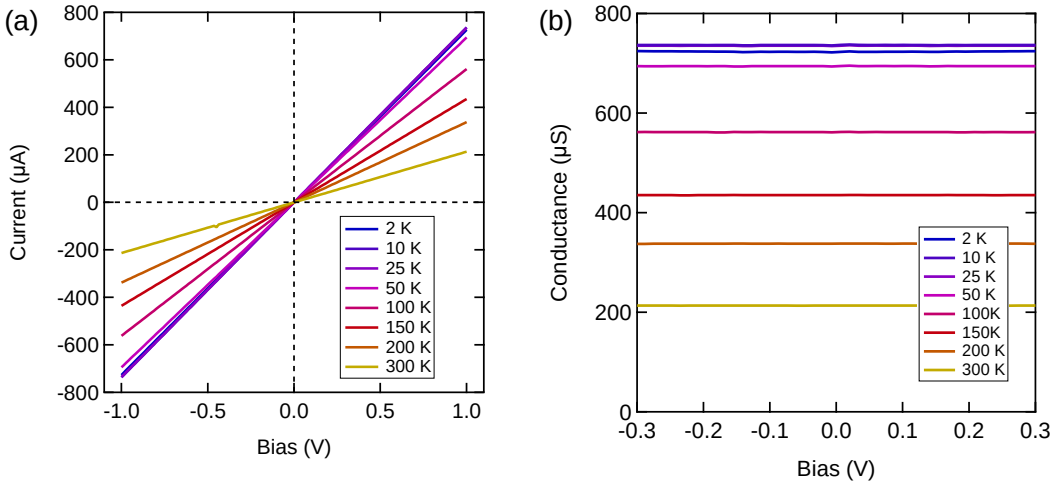

Figure 3.2 (a) $I-V$ sweeps collected between Ti contacts deposited on a 10 nm $SmTiO_3$/2 SrO/ 10 nm $SmTiO_3$ quantum well structure. (b) Differential conductance (dI/dV) obtained via numerical differentiation of the $I-V$ data. The flat conductance demonstrates the ohmic nature of the contacts down to 2 K. Reprinted with permission from P. B. Marshall, E. Mikheev, S. Raghavan, and S. Stemmer, Physical Review Letters 117, 046402 (2016), Copyright 2016 by the American Physical Society (Ref. [85]).

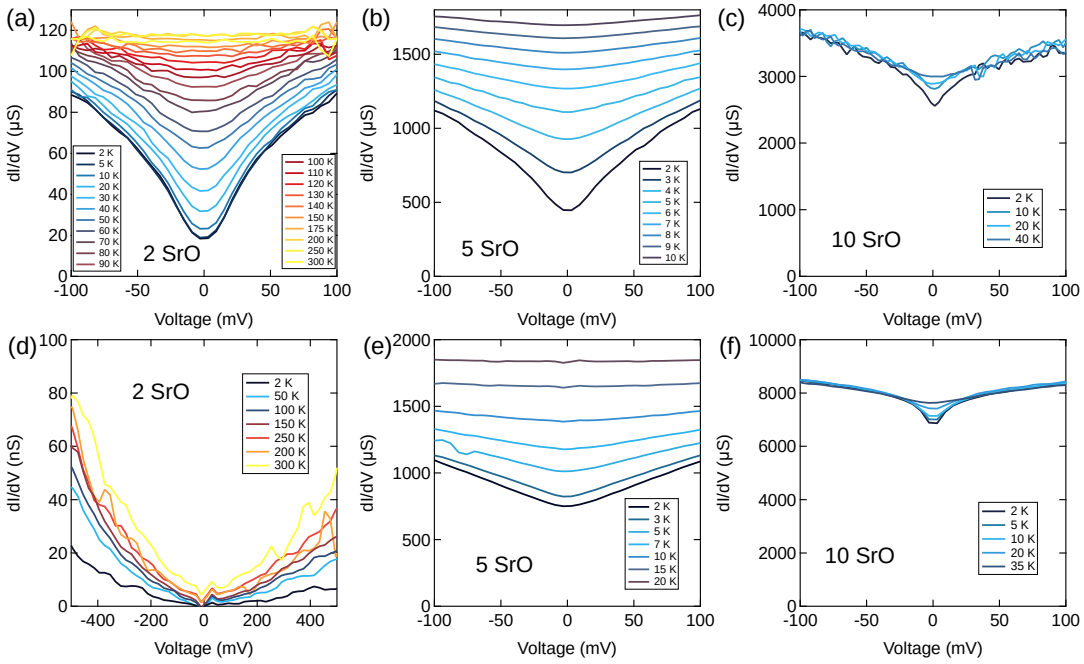

Figure 3.3 Raw conductance spectra (dI/dV) of 2, 5, and 10 SrO layer thick quantum wells embedded in both $SmTiO_3$ (a)-(c) and $GdTiO_3$ (d)-(f). Reprinted with permission from P. B. Marshall, E. Mikheev, S. Raghavan, and S. Stemmer, Physical Review Letters 117, 046402 (2016), Copyright 2016 by the American Physical Society (Ref. [85]).

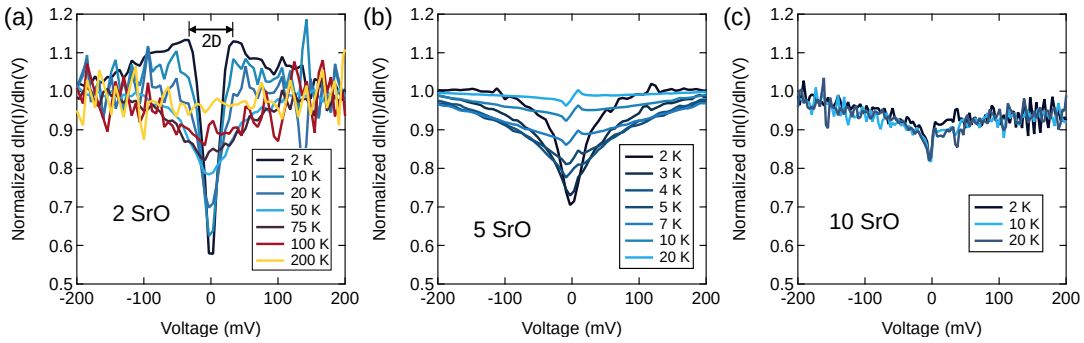

Figure 3.4 Normalized differential conductance $(d\ln(I)/d\ln(V))$ for quantum wells embedded in $SmTiO_3$. The pseudogap feature centered on the Fermi level becomes more pronounced as the well thickness is reduced. Coherence peaks emerge at low temperatures in the 2 SrO layer thick well with an energy spacing 2Δ of approximately 65 meV. Reprinted with permission from P. B. Marshall, E. Mikheev, S. Raghavan, and S. Stemmer, Physical Review Letters 117, 046402 (2016), Copyright 2016 by the American Physical Society (Ref. [85]).

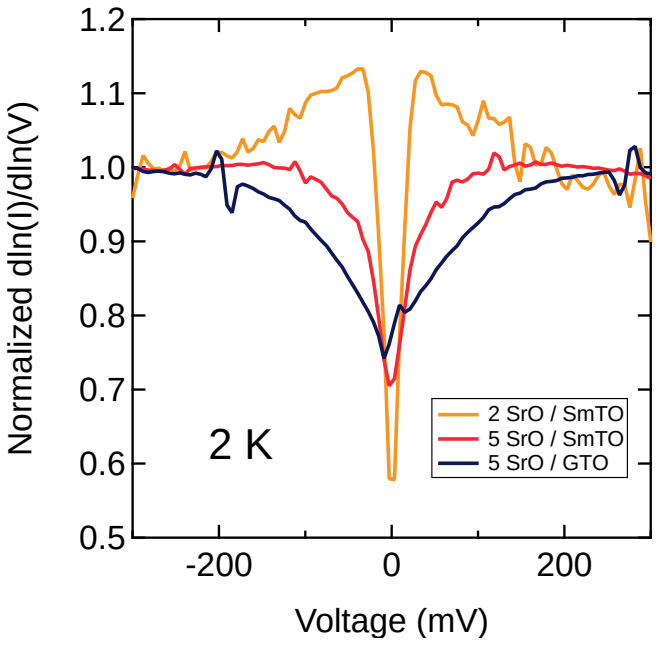

Figure 3.5 Comparison of normalized conductance of the 2 and 5 SrO layer thick quantum wells embedded in $SmTiO_3$ and the 5 SrO layer thick well embedded in $GdTiO_3$. Pronounced coherence peaks emerge in $SmTiO_3$-embedded wells but not in $GdTiO_3$-embedded wells. Reprinted with permission from P. B. Marshall, E. Mikheev, S. Raghavan, and S. Stemmer, Physical Review Letters 117, 046402 (2016), Copyright 2016 by the American Physical Society (Ref. [85]).

Chapter 4 Effect of Disorder on Scattering Rate separation

4.1 Introduction

Transport in strongly correlated metals differs from conventional metallic behavior in numerous striking ways. This includes non-Fermi liquid scattering behavior observed in the temperature dependence of the longitudinal resistivity, in which the exponent n takes on values lower than the typical Fermi liquid value of 2 in the power law expression $R_{xx} = R_o + AT^n$. The classic example of this is the T-linear (n = 1) behavior observed in the cuprate superconductors. It is believed by some that uncovering the microscopic origin of this behavior may be the key in unraveling the mystery of high-T_C superconductivity. A related but more subtle transport anomaly is the phenomenon of *scattering rate separation*, introduced in Section 1.5. Scattering rate separation refers to a divergence of the Hall and longitudinal scattering rates ($\tau_{xx} \neq \tau_H$), in contrast to conventional metallic behavior where they are assumed to be equivalent. Evidence of lifetime separation has been observed in many of the same systems in which non-Fermi liquid behavior has been reported. This includes the cuprates [26], the $V_{2-y}O_3$ system [27], and heavy Fermion materials [93]. Theories that have been proposed to explain this behavior include anisotropic scattering on the Fermi surface (commonly seen near an antiferromagnetic transition) [29], separation of spin and charge degrees of freedom (Luttinger liquid behavior) [24], and proximity to a quantum critical point [30]. Despite this, no microscopic theory is universally accepted. Developing a comprehensive understanding of two-lifetime behavior and the associated robust T^2 dependence of the Hall scattering rate, which seems

to be nearly universal among these systems, may go a long way in advancing the understanding of strong electron correlations and quantum criticality.

The quantum criticality and non-Fermi liquid scattering behavior observed in RTiO$_3$/SrTiO$_3$/RTiO$_3$ (R = Gd, Sm) quantum wells is also accompanied by scattering rate separation. The thickness of the quantum wells, which acts as the non-thermal external tuning parameter determining proximity to the quantum critical point, also controls the extent of carrier lifetime separation [63]. As mentioned previously, the precise control of dimensionality in these quantum well systems offered by MBE makes this system ripe for detailed investigation of the scattering rate separation phenomenon. Additionally, when grown epitaxially on the (001) surface of DyScO$_3$ substrates, uniformly spaced and highly anisotropic planar defects were found to form in the film. This offers an excellent route by which the effect of disorder on lifetime separation behavior can be investigated via angle-dependent measurements. In this chapter we report on a study in which these questions were addressed through electrical characterization of a series of SmTiO$_3$/SrTiO$_3$/SmTiO$_3$ quantum wells grown on DyScO$_3$ (001) substrates.

4.2 Growth, Fabrication, and Measurement Technique

Hybrid MBE, introduced in Section 2.5, was used to grow a series of quantum wells with the structure SmTiO$_3$/SrTiO$_3$/SmTiO$_3$ on (001) DyScO$_3$ substrates. SrTiO$_3$ quantum wells with thicknesses of 2, 3, 4, 5, 6, and 10 SrO layers were grown, where the thickness of the quantum well layer is specified in terms of the number of SrO planes that it contains.

The structure of the $DyScO_3$ substrate belongs to the orthorhombic *Pbnm* space group, similar to the $SmTiO_3$ barrier layers. This is in contrast to many previous studies of this quantum well system in which the wells were grown on cubic $(LaAlO_3)_{0.3}(Sr_2AlTaO_6)_{0.7}$ (LSAT) substrates. This distinct substrate symmetry, which was found to modify the growth orientation of the $SmTiO_3$ barrier layers, has important effects on the transport properties. This will be discussed later.

Angle-dependent measurements of the 3 and 6 SrO layer thick quantum wells were made possible through the fabrication of "centipede" devices with a series of photolithography, dry etching, and contact deposition steps. The devices allowed transport measurements to be performed along four crystallographic directions which were equally spaced in intervals of 45°. Electrical contact was made using electron beam evaporated Ti contacts, which have previously been demonstrated to remain Ohmic down to 2 K. A layer of Au was deposited on top of the Ti to facilitate wire bonding. The transport measurements were performed at temperatures ranging from 300 K down to 2 K in a Quantum Design Physical Property Measurement System, with the Hall resistance being measured using sweeps of the magnetic field from -0.6 T to 0.6 T. High-angle annular dark-field (HAADF) scanning transmission electron microscopy (STEM) images were taken of the quantum well structure using cross-sectional specimens prepared in an FEI Helios dual beam focused ion beam microscope. Imaging was performed with an FEI Titan S/TEM operating at 300 kV.

4.3 Planar Defects and Barrier Orientation

To characterize the microstructure, HAADF-STEM images were taken of the 6 SrO layer thick quantum well along two orthogonal directions. The images are shown in Figure 4.1 (a) and (b) looking along the $[010]_O$ and the $[100]_O$ crystallographic directions, respectively, where the subscript indicates that the directions are referenced to the orthorhombic unit cell. We note that the bottom $SmTiO_3$ barrier layer has grown with its $(001)_O$ planes parallel to the substrate surface, which is apparent when comparing the schematics of the crystal structure in Figure 4.1 (c) and (d) to the corresponding STEM images of Figure 4.1 (a) and (b). This orientation is different than previous studies of this system, including the study of the pseudogap behavior in Chapter 3, in which the quantum wells were grown on cubic LSAT substrates. When grown epitaxially on LSAT the $SmTiO_3$ barrier grows its the $(110)_O$ planes parallel to the substrate. The difference in the growth orientation can be explained by the different strain states of the $SmTiO_3$ when grown on the two substrates. The lattice constant of LSAT is 3.87 Å, while the pseudocubic in-plane lattice constant of the $DyScO_3$ (001) surface is 3.95 Å. The pseudocubic in-plane lattice constants of $SmTiO_3$ are 3.90 Å and 3.94 Å for the $(110)_O$ and the $(001)_O$ crystal planes, respectively. Therefore it is energetically favorable for the $(001)_O$ $SmTiO_3$ plane to be parallel to the substrate surface when grown on $DyScO_3$ (001), as this minimizes the energy built up by elastic strain. This demonstrates how judicious choice of a substrate surface can be used to engineer the crystallographic orientation during epitaxial growth, a concept that is applicable to other materials systems. This is especially relevant to the

study of the transport properties of strongly correlated materials, as minute structural changes have been shown to lead to substantial modifications of the transport behavior.

Looking along the $[010]_O$ direction in Figure 4.1 (a), no extended defects are visible. When looking along the $[100]_O$ direction, however, planar defects are present (marked by red arrows in Figure 4.1 (b)). The fact that they are not visible along one direction but clearly visible along an orthogonal direction indicates that the planar defects are highly anisotropic. They are fairly uniformly spaced, with an average spacing of about 20 nm. Due to the highly anisotropic nature of the defects one may expect a high degree of anisotropy in the in-plane electrical resistivity, particular in the low-temperature residual resistivity. It is this anisotropy, to be discussed in detail in the following sections, which allowed for the systematic study of the effect of disorder on scattering rate separation detailed in this chapter.

Finally, we observe a zigzag pattern in the A-site cation displacements in the $DyScO_3$ substrate and $SmTiO_3$ barrier in the STEM image along $[100]_O$. No such pattern is visible in the $SrTiO_3$ quantum well, a sign that distortion to an orthorhombic structure has not yet occurred in the 6 SrO layer thick quantum well. Instead, the structure of the $SrTiO_3$ in the well retains a slightly tetragonal structure (due to the epitaxial strain) with no significant tilting of the oxygen octahedra. Previous structural studies of $SrTiO_3$ quantum wells grown on LSAT have found that orthorhombic distortions in the $SrTiO_3$ can be induced below a critical quantum well thickness [61], but this has not yet occurred in the 6 SrO layer thick well in the present study.

Confirmation of the epitaxial relationship between the $SmTiO_3$ barrier and the $DyScO_3$ substrate was obtained via a reciprocal space map of one of the quantum well structures, shown in Figure 4.2. This was achieved by aligning a high-resolution x-ray diffractometer to the (116) orthorhombic peak of the substrate. The alignment of the in-plane lattice parameters along q_x (horizontal axis) confirms that the $SmTiO_3$ is fully strained.

4.4 Results of Electrical Transport Measurements

The results for the in-plane sheet resistance R_{xx} as a function of temperature made using the centipede Hall bar devices are shown in Figure 4.3 (a) and (b) for the 3 and 6 SrO layer thick wells, respectively. Measurements were made along the [100], [110], [$1\bar{1}0$], and [010] crystallographic directions. Clear anisotropies in the value of the sheet resistance are observed in both quantum wells, with similar dependences on angle. The angle-dependence of the resistance is not surprising when the preferred orientation of the planar defects is considered. The [100] direction runs parallel to the defects, allowing the electrons to travel relatively unimpeded when driven by an electric field and therefore resulting in the lowest resistance. The [010] direction runs perpendicular to the defects, subjecting the electrons to the greatest scattering and therefore resulting in the maximum resistance. Both the [110] and [$1\bar{1}0$] directions run at 45° angles to the defects, therefore resulting in similar resistances roughly half way between the two extremes. The quantity dR_{XX}/dT for the 6 SrO layer thick well is plotted versus temperature on a logarithmic

scale in Figure 4.3 (c). The slope of the curve in such a plot provides a measure of the power law exponent n in the expression $R_{XX}(T) = R_0 + AT^n$. The dotted black line shows the expected slope for conventional Fermi liquid behavior with $n = 2$. Clearly none of the curves follow this behavior. In fact, because the slopes of the lines are not constant at any temperature, one can conclude that $R_{XX}(T)$ in this disordered system does not follow a well-defined power law at all.

The Hall angle, $H \cot\theta_H$, can be calculated in a straightforward manner using knowledge of R_{XX} and the Hall coefficient R_H according to the formula

$$H \cot\theta_H = H\frac{R_{XX}}{R_{XY}} = \frac{R_{XX}}{R_H} = H(C + \alpha T^2), \qquad 4.1$$

where H is the applied magnetic field, R_{XY} is the Hall resistance, C is the Hall angle residual (which is effectively the inverse Hall mobility μ_H^{-1} extrapolated to 0 K), and α is the Hall scattering amplitude, which is related to the electron effective mass via the relationship

$$\alpha T^2 = \frac{m^*}{e}\Gamma(T^2), \qquad 4.2$$

where Γ is scattering rate and e is the elementary charge. The Hall angle of the 6 SrO layer thick quantum well is plotted as a function of temperature on a T^2 scale in Figure 4.4 (a). We note that the curves are very linear along all four directions, indicating a strong T^2 dependence regardless of the measurement angle. We also observe that there is very little variation in the slope of the lines. Because the slope is determined by $H\alpha$, this implies that $H\alpha$ is a disorder-independent quantity that gives a measure of the amplitude of *intrinsic*

electron-electron scattering mechanisms. This curious disorder-independence of $H\alpha$ has also been observed in the cuprates [95].

Extrapolating the Hall angle in Figure 4.4 (a) to 0 K allows us to extract the Hall angle residual HC. The Hall residual is plotted as a function of the angle of the measurement relative to the lowest resistance $[100]$ axis (defined as 0°) in Figure 4.4 (b), along with the low temperature residual of the sheet resistance R_{XX} at 2 K, which can be taken as a close estimate of R_0. The resistance residuals were taken from the data in Figure 4.3 (b). Here we observe a strong dependence of both of the quantities on angle, and we can therefore conclude that both of the residuals are strongly dependent on disorder. Furthermore, the two quantities scale in a very similar fashion, which is to say that a given degree of disorder introduced by the planar defects in the film enhance both R_0 and HC by the same factor. The strong dependence of HC on the amount of disorder present has also been noted in the cuprates, where it was found to increase linearly with the concentration of impurity dopants [26], [95]. A linear relationship between HC and disorder is also observed in the present data, indicating that the linear relationship of HC and disorder is a very general behavior. We can also conclude that only a single transport lifetime is influenced by disorder due to the similar scaling of R_0 and HC.

We can also deduce that the carrier lifetime separation phenomenon is present in these quantum wells. In Figure 4.3 (c), analyzing the temperature dependence of R_{XX}, we saw that $R_{XX}(T)$ did not follow a well-defined power law at all, likely due to the high degree of disorder. In stark contrast, the Hall angle $H\cot\theta_H(T)$ follows a robust T^2 dependence regardless of the amount of disorder. Therefore, for the scattering mechanism

that influences the temperature dependent transport there must be two carrier lifetimes: one that influences the temperature dependence of R_{XX} that does not follow a well-defined power law and one that influences the temperature dependence of $H\cot\theta_H$ which has a strong quadratic dependence on temperature.

Because the Hall scattering amplitude $H\alpha$ can be interpreted as a robust measure of the amplitude of intrinsic electron-electron interactions, it is interesting to consider what effect the quantum well thickness t_{QW} might have on the scattering amplitude. Decreasing the well thickness will change the effective three-dimensional carrier concentration, as well as increasing tendency towards structural distortion in the well due to proximity to the orthorhombically distorted barrier material. The Hall scattering amplitude measured in $SmTiO_3/SrTiO_3/SmTiO_3$ quantum wells grown on both LSAT and $DyScO_3$ substrates are compared as a function quantum well thickness, t_{QW}, in Figure 4.5 (a). The data from the quantum wells on LSAT were taken form Ref. [63].

A similar trend in $H\alpha$ is observed in both curves. It is relatively constant in thicker quantum wells, with an abrupt increase below a critical thickness. The average $H\alpha$ is about 50% higher in the wells grown on $DyScO_3$ compared to the wells grown on LSAT. The critical thickness under which $H\alpha$ begins to diverge is near 5 SrO layers on $DyScO_3$ and 3 SrO layers on LSAT. The residual of R_{xx} measured at 2 K as a function of t_{QW} are compared for the two substrates in Figure 4.5 (b). Similar to $H\alpha$, $R_{XX}(2\ K)$ is nearly constant in thicker quantum wells with an abrupt increase under a critical well thickness. This critical thickness is near 3 SrO layers on $DyScO_3$ and 1 SrO layer on LSAT.

The temperature-dependences of the quantity $(eR_H)^{-1}$ for the 3 and 6 SrO layer thick quantum wells are shown in Figure 4.6 (a) and (b), respectively. Measurements along the high resistance direction, [100], and the low resistance direction, [010] are plotted. As mentioned previously, in the absence of lifetime separation and with a single carrier type, $(eR_H)^{-1}$ is simply a measure of the sheet carrier concentration. This is typically the case in weakly correlated metals and semiconductors. This is also the case in $SmTiO_3/SrTiO_3/SmTiO_3$ quantum wells at high temperatures, as the value of $(eR_H)^{-1}$ at 300 K corresponds to a sheet carrier concentration of around 7×10^{-14} cm^{-2}, which is the expected in the absence of correlation effects.

If correlation effects are present the value of $(eR_H)^{-1}$ can be affected, leading to shifts in its low temperature value or non-trivial temperature dependences. This is the case in the 6 SrO layer thick quantum well in Figure 4.6 (b). As discussed in the introduction in Section 1.5, the Hall coefficient is the ratio of the in-plane sheet resistance to the Hall angle, leading to

$$(eR_H)^{-1} = \frac{H}{e}\left(\frac{C+\alpha T^2}{R_0+AT^n}\right). \qquad 4.3$$

The departure from trivial temperature-independent behavior can arise from both divergences in the low temperature residual, C/R_0, and from deviations from T^2-behavior in the in-plane resistivity. Not only could a non-trivial temperature dependence arise from a power-law exponent of the temperature dependence of the resistivity that differs from the

Fermi liquid value $n = 2$, but also if the resistivity does not follow a well-defined power law at all, as is the case in the quantum wells in this study.

Not only is non-trivial temperature dependence apparent in the 6 SrO layer thick quantum well, but a shift in the low temperature residual C/R_0 is clear as well. Rather than the value of ~ 7×10^{-14} cm^{-2} expected based on the interfacial area of the unit cell, the value at 2 K increases to near 1.1×10^{-15} cm^{-2}, an enhancement of C/R_0 by a factor of 1.6 compared to its expected value. This enhancement is not present in the 3 SrO layer thick quantum well.

A comparison of the Hall angle residuals, $(eR_H)^{-1}(2\,K)$, for various well thicknesses in quantum wells grown on both $DyScO_3$ and LSAT substrates is shown in Figure 4.7. A similar dependence on well thickness is seen for both substrates. The initial value in thin wells is close to the expected value, followed by a steady increase to a maximum value. The value then drops off to near the expected value in thick quantum wells. Although the shape is the same, the curves are shifted, with the maximum value of $(eR_H)^{-1}(2\,K)$ occurring near 4 or 5 SrO layers for quantum wells grown on LSAT and 6 SrO layers for quantum wells grown on $DyScO_3$.

4.5 Effects of Quantum Well Barrier Orientation on Correlations

As discussed in Section 4.3, the crystallographic orientation of the $SmTiO_3$ barrier layers is different when grown on LSAT and $DyScO_3$ substrates due to the different

epitaxial strains. $SmTiO_3$ layers on LSAT grow with the (110) crystal plane parallel to the substrate surface, while $SmTiO_3$ on $DyScO_3$ grows with the (001) plane parallel to the surface. The barriers are effectively rotated by 90° relative to each other, thereby changing the orientation of the A-site structural distortions as seen in Figure 4.1.

Differences in the transport properties are apparent between the quantum wells grown on LSAT in previous studies and the wells grown on $DyScO_3$ in the present study. First of all, the Hall scattering amplitude was enhanced by roughly 50% on the wells on $DyScO_3$ from 1 to 1.5×10^{-6} $Vs/cm^2/K^2$. It is likely that this increase originates from an enhancement of the in-plane effective mass, as $\alpha \propto m^*$. In addition to the enhancement of the value of $H\alpha$, the critical thickness under which the abrupt increase in $H\alpha$ occurred was greater on $DyScO_3$ compared to LSAT. This likely originates from subtle changes in how the structure of the barrier layers couples into the well layer for the two orientations. In thin quantum wells, structural differences in the barrier may be expected to couple into the transport properties of the well itself, which can increase effective mass [61], [96]. Both theory and experimental observations have also shown that the magnetic order of the barrier can couple into the itinerant electron system in thin wells [60], [97]. This may also increase the effective mass [98].

The temperature dependence of R_{XX} also varies in the wells grown on the two substrates. In quantum wells grown on LSAT R_{XX} follows well-defined power laws of the form $R_{XX}(T) = R_0 + AT^n$, where a shift in the exponent n from the Fermi liquid value of 2 to non-Fermi liquid values tracks proximity to a quantum critical point. On the other

hand, $R_{XX}(T)$ in quantum wells grown on $DyScO_3$ does not follow well-defined power laws at all. It is likely that the greater disorder in these wells brings the carriers in close proximity to a disorder-induced localization transition, resulting in the complicated temperature dependence of $R_{XX}(T)$. This is especially evident in the 3 SrO layer thick well, where the $R_{XX}(T)$ curve in the high resistance [010] direction in Figure 4.3 (a) actually has a negative slope near room temperature. In any case, the temperature dependence of the Hall angle is not influenced by the scattering mechanism controlling the in-plane resistivity, as it retains a robust T^2 dependence on both substrates for every quantum well thickness.

4.6 Implications for Theory of Carrier Lifetime Separation

Much of the literature treating the two carrier lifetime phenomenon focuses on the specific case in which $R_{XX} \sim T$ and $\cot\theta_H \sim T^2$. In fact, some consider an understanding of the T -linear dependence of the resistivity observed in many unconventional superconductors to be the essential ingredient needed to unravel the mystery of high temperature superconductivity. However, the present data suggests that the nearly universal T^2 of the Hall scattering rate may be the fundamental feature underlying the physics of these systems. The previous studies of quantum well grown on LSAT substrates found that the T^2 dependence of the Hall scattering rate persists even when the power-law exponent of the resistivity takes on non-Fermi liquid values [63]. The data from the quantum wells grown on $DyScO_3$ substrates take this a step further and show that the

$\cot\theta_H \sim T^2$ dependence remains even when large amounts of disorder are present and $R_{XX}(T)$ does not follow a power law at all. The central conclusion that can be taken from this is that the ubiquitousness and the robust character of the T^2 dependence of $\cot\theta_H$ should be a central consideration when developing models of correlated electron systems near a quantum critical point. This has been considered in the study of the cuprates [99], but this study suggests that this pertains to an even wider class of materials.

A scattering rate obeying a T^2 dependence is often taken as an indication of electron-electron scattering in a Fermi liquid. However, an essential feature of Fermi liquid behavior is a scattering rate that is dependent on the three-dimensional carrier concentration. The scattering rate in the quantum wells shows evidence of a carrier density independent scattering rate. This is evident in the data of Figure 4.5 (a). The quantity $H\alpha$, a measure of the intrinsic electron-electron scattering rate, is constant with quantum well thicknesses above a critical thickness. Because the three-dimensional carrier concentration decreases with increasing quantum well thickness, we can conclude that the electron-electron scattering rate is independent of the carrier density. Therefore, the T^2 dependence of the Hall angle cannot be ascribed to an underlying Fermi liquid. This carrier density independence of the scattering rate is also present in many other strongly correlated materials where transport measurements reveal a scattering rate with a strong T^2 dependence. This supports the argument made in Ref. [20] that a T^2 dependent scattering rate should not automatically be attributed to the presence of a Fermi liquid state, as is often done in studies of cuprates and other transition metal oxides. Rather, a distinct and poorly

understood scattering mechanism may be at play. This highlights the importance of the development of a unified microscopic theory of the origin of the T^2 scattering dependence in strongly correlated materials.

This study also provides insight into the origin of the microscopic parameters determining the Hall scattering rate. In previous studies of this quantum well system the divergence of the low temperature residual C/R_0, also shown in the present data (Figure 4.7), was ascribed to a quantum critical point. The data suggest that critical fluctuations appear in the residual C but *not* in R_0. The data in Figure 4.6 show that the divergence of C/R_0 does not arise from disorder. The low-temperature residual is the same, regardless of if the measurement is taken along the low resistance [100] or the high resistance [010] direction. Thus, the scattering rate, and perhaps its temperature dependence, originates from electronic correlations. Also, the results show that the Hall angle $\cot(\theta_H)$ is less sensitive to carrier localization than the resistivity. The same carrier can appear localized or delocalized depending on the specific transport coefficient under consideration.

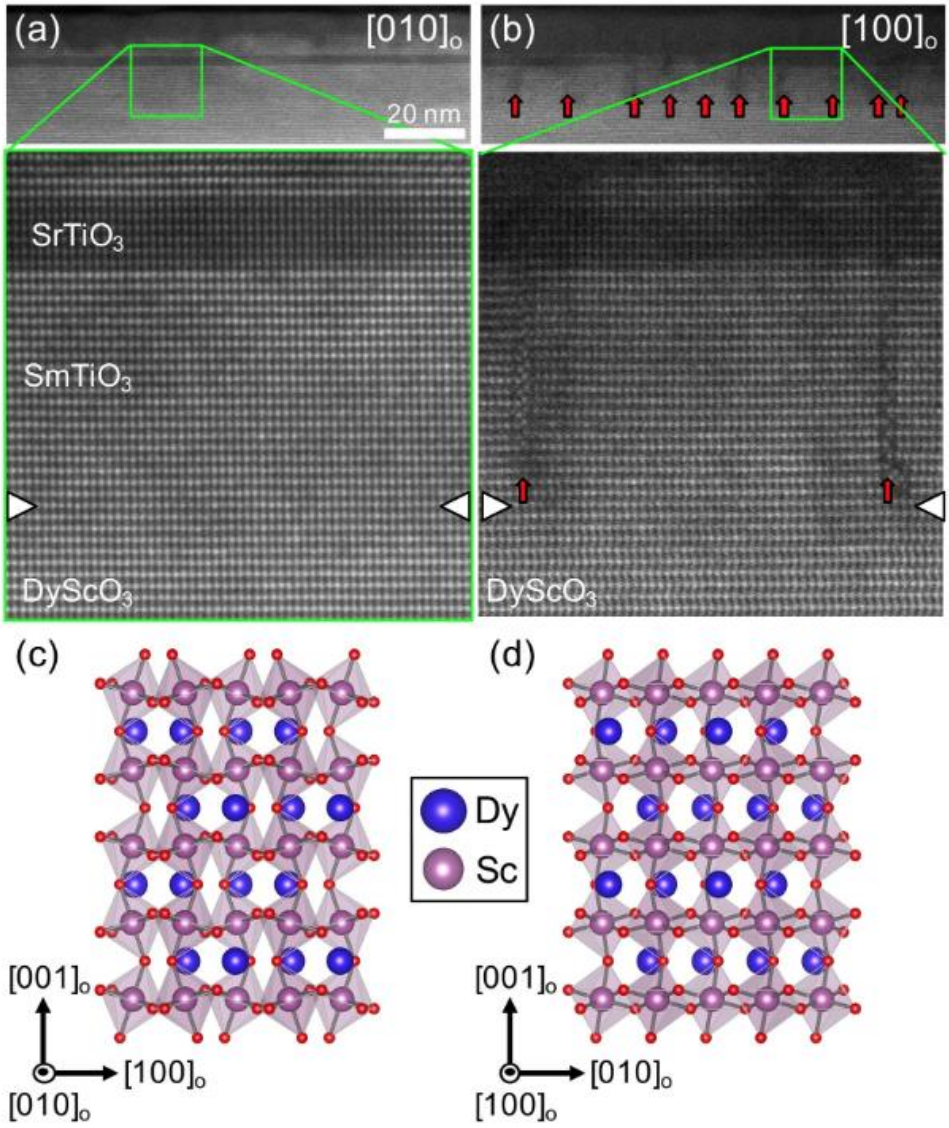

Figure 4.1 HAADF-STEM images of 6 SrO thick quantum well along (a) $[010]_O$ and (b) $[100]_O$ directions. Planar defects, marked with red arrows, are visible when looking along $[100]_O$ but not along $[010]_O$, suggesting a high degree of anisotropy. Additionally, they are fairly uniformly spaced, with about 20 nm separating adjacent defects. Illustrations of the structure of the $DyScO_3$ substrate looking along $[010]_O$ and $[100]_O$ are shown in (c) and (d), respectively. Reprinted from P. B. Marshall, H. Kim, and S. Stemmer, Scientific Reports 7, 10312 (2017). This article is distributed under a Creative Commons Attribution 4.0 (CC BY 4.0) license (https://creativecommons.org/licenses/by/4.0/). (Ref. [94]).

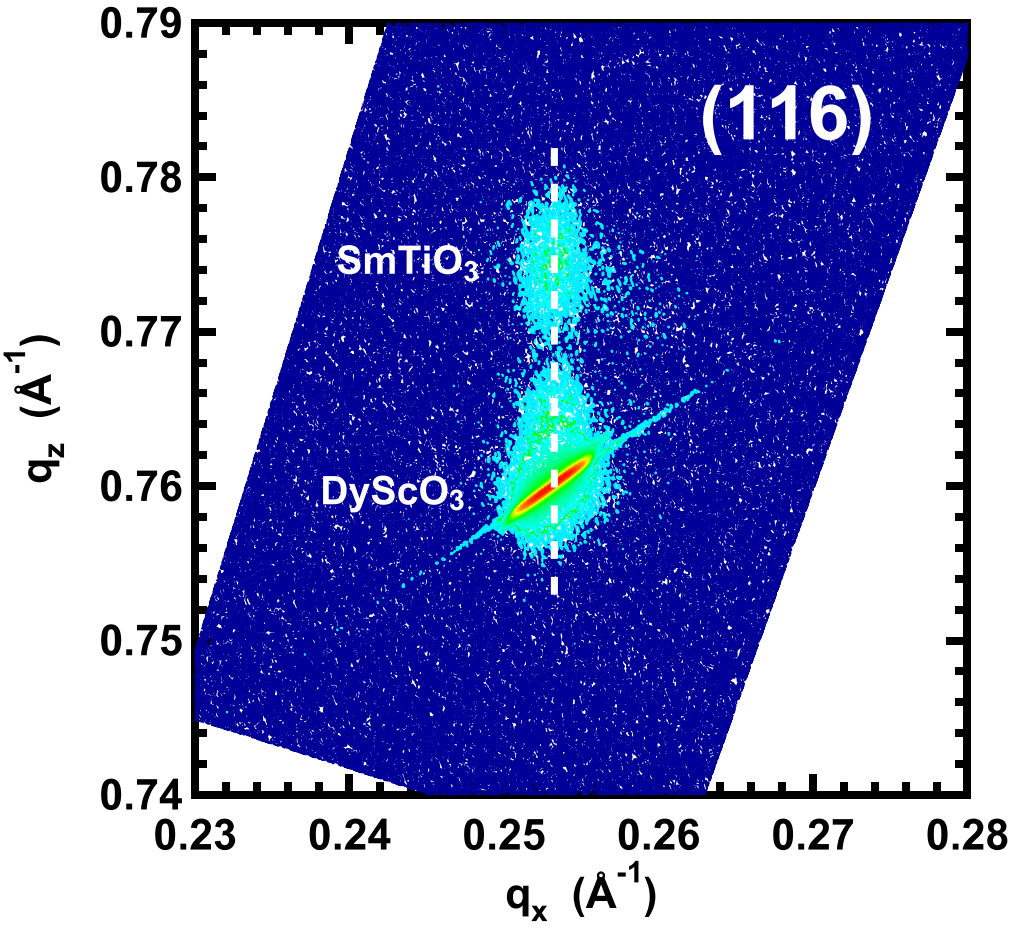

Figure 4.2 Reciprocal space map taken around the (116) orthorhombic peak of the $DyScO_3$ substrate of a 10 nm $SmTiO_3$/10 SrO/10 nm $SmTiO_3$ quantum well structure. The alignment of the in-plane lattice constants along the horizontal axis confirms that the $SmTiO_3$ barrier layers are fully strained to the substrate. Reprinted from P. B. Marshall, H. Kim, and S. Stemmer, Scientific Reports 7, 10312 (2017). This article is distributed under a Creative Commons Attribution 4.0 (CC BY 4.0) license (https://creativecommons.org/licenses/by/4.0/). (Ref. [94]).

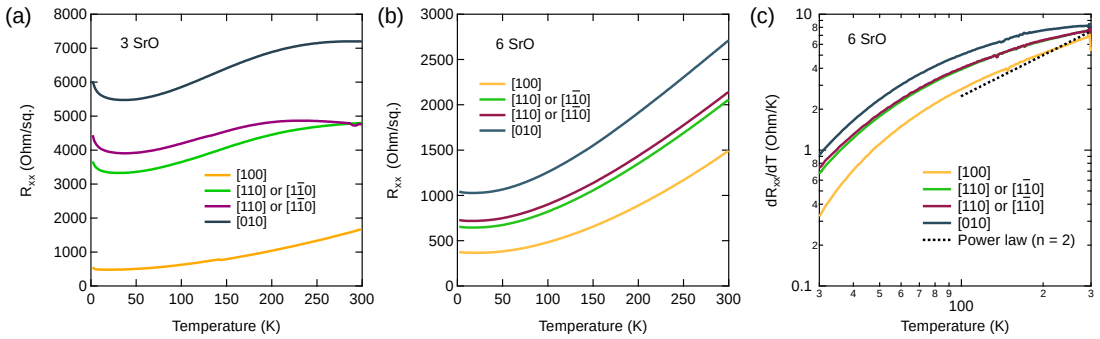

Figure 4.3 In-plane sheet resistance R_{XX} as a function of temperature along the four crystallographic directions defined by the centipede Hall bar device in the (a) 3 and (b) 6 SrO layer thick quantum wells. (c) The quantity dR_{XX}/dT for the 6 SrO layer thick well plotted on a logarithmic temperature scale. The dash line represents the expected slope for a T^2 temperature dependence. Reprinted from P. B. Marshall, H. Kim, and S. Stemmer, Scientific Reports 7, 10312 (2017). This article is distributed under a Creative Commons Attribution 4.0 (CC BY 4.0) license (https://creativecommons.org/licenses/by/4.0/). (Ref. [94]).

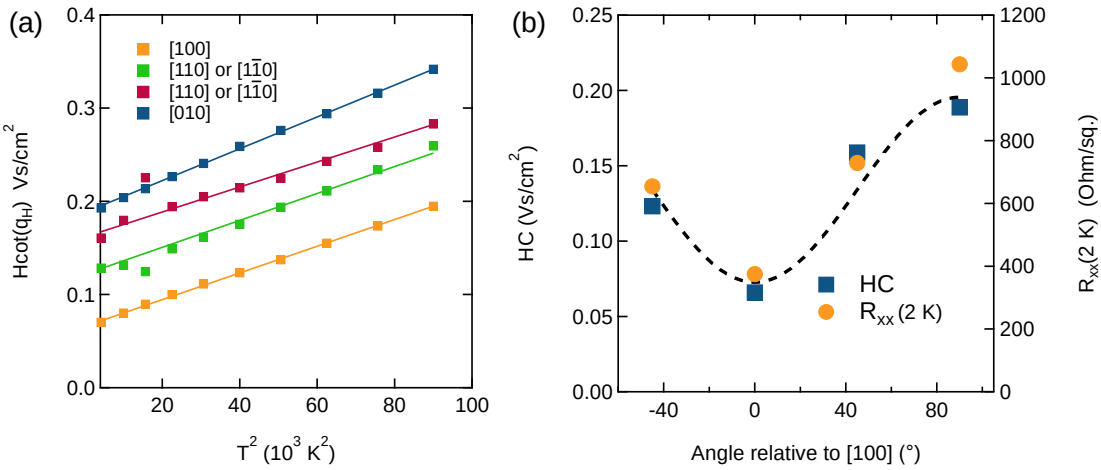

Figure 4.4 (a) Temperature dependence of the Hall angles of the 6 SrO layer thick quantum well plotted on a T^2 axis measured with the Hall bar centipede device. (b) Low-temperature residuals of the Hall angle, HC, and the sheet resistance, $R_{XX}(2\,K)$ as a function of angle relative to the low resistance [100] direction, which is defined as 0°. Reprinted from P. B. Marshall, H. Kim, and S. Stemmer, Scientific Reports 7, 10312 (2017). This article is distributed under a Creative Commons Attribution 4.0 (CC BY 4.0) license (https://creativecommons.org/licenses/by/4.0/). (Ref. [94]).

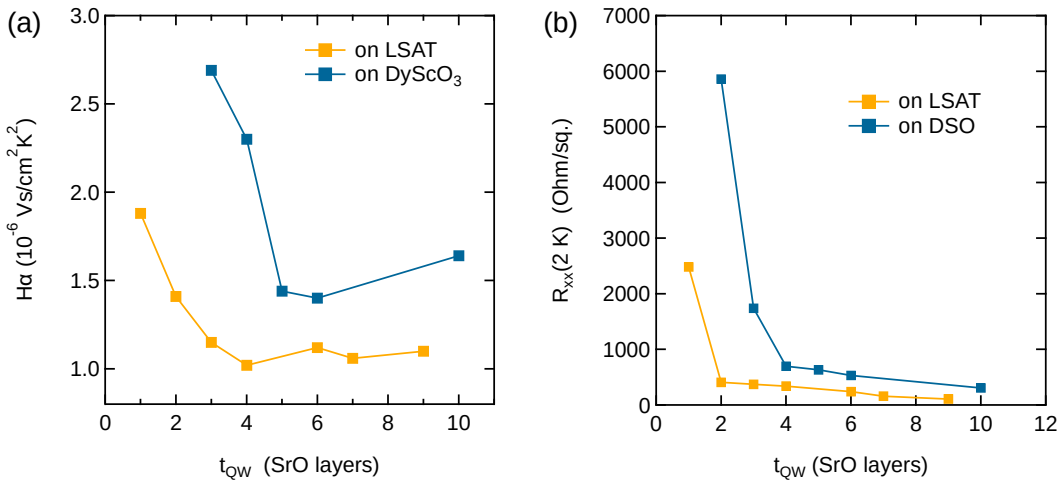

Figure 4.5 (a) Comparison of Hall scattering amplitude $H\alpha$ as a function of quantum well thickness for wells grown on $DyScO_3$ and LSAT substrates. (b) Similar comparison of the residual sheet resistance measured at 2 K, $R_{XX}(2\ K)$. The data from the wells grown on LSAT was taken from Ref. [63]. Reprinted from P. B. Marshall, H. Kim, and S. Stemmer, Scientific Reports 7, 10312 (2017). This article is distributed under a Creative Commons Attribution 4.0 (CC BY 4.0) license (https://creativecommons.org/licenses/by/4.0/). (Ref. [94]).

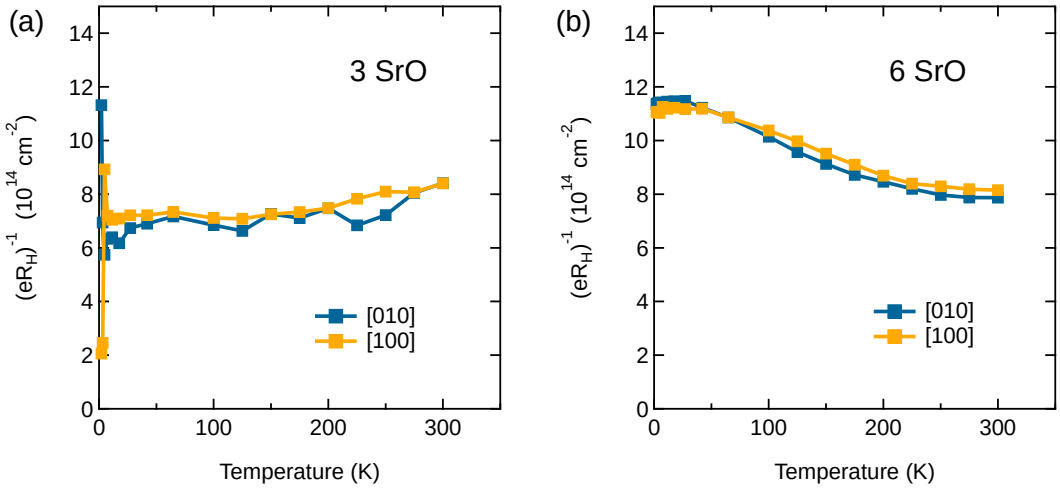

Figure 4.6 The quantity $(eR_H)^{-1}$ as a function of T for the (a) 3 SrO layer and (b) 6 SrO layer thick quantum wells. Measurements were taken along the high resistance [010] and low resistance [100] directions. Reprinted from P. B. Marshall, H. Kim, and S. Stemmer, Scientific Reports 7, 10312 (2017). This article is distributed under a Creative Commons Attribution 4.0 (CC BY 4.0) license (https://creativecommons.org/licenses/by/4.0/). (Ref. [94]).

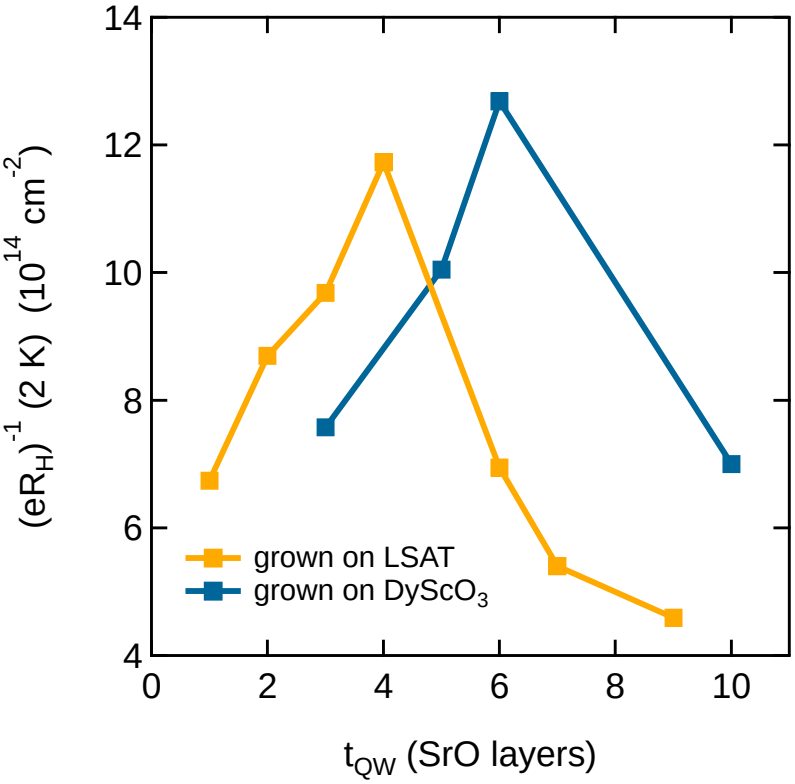

Figure 4.7 Comparison of the Hall angle residual measured at 2 K, $(eR_H)^{-1}(\,2\,K)$, for quantum wells grown on LSAT and $DyScO_3$ substrates as a function of t_{QW}. The data for the wells grown on LSAT was taken from Ref. [63]. Reprinted from P. B. Marshall, H. Kim, and S. Stemmer, Scientific Reports 7, 10312 (2017). This article is distributed under a Creative Commons Attribution 4.0 (CC BY 4.0) license (https://creativecommons.org/licenses/by/4.0/). (Ref. [94]).

Chapter 5 Growth of the Strontium Ruthenate Ruddlesden-Popper Series with a Hybrid MBE Approach

5.1 Motivation for the MBE Growth of Strontium Ruthenate

The observation of phenomena such as *p*-wave spin triplet superconductivity, metamagnetism, and nematic order in the layered strontium ruthenate Ruddlesden-Popper series, introduced in Section 2.4, has led to a surge of interest in the epitaxial growth of these materials to explore their physics in thin film form [23], [68], [100]. One driving factor is the possibility of strain engineering of the Fermi surface of these materials, which will allow for systematic studies with the aim of achieving a deeper understanding of how these phenomena emerge from the strong electron correlations and complex magnetic states in these materials [37]. To date, the majority of the experiments involving this class of materials have been performed on bulk single crystal samples.

Synthesis with thin film deposition methods has remained more challenging than bulk crystal growth. This largely stems from the extremely low vapor pressure of Ru, which makes thermal sublimation with a standard effusion cell nearly impossible. Some success has been achieved with pulsed laser deposition or through the use of an electron beam evaporated Ru source in an MBE environment [101], [102]. However, the flux provided from electron beam evaporation is inherently unstable and the highly energetic deposition oftentimes generates point defects, making this technique difficult to control reproducibly. Another challenge is the limit of the amount of oxygen that can be introduced to the growth chamber and the flux instabilities associated with high oxygen background pressures, potentially leading to oxygen deficiency in the film.

It is therefore of interest to explore alternative sources of Ru with which the growth rate can be precisely controlled and the depositing species reach the surface with a lower energy. One route to achieve this is through the use of a volatile precursor, similar to the hybrid MBE technique developed for the growth of the titanates detailed in Section 2.5. In this chapter we will explore the use of the volatile inorganic precursor ruthenium tetroxide (RuO_4) for the growth of the layered strontium ruthenate series with a hybrid MBE approach. Several features make RuO_4 promising as a precursor for ruthenate growth. First, RuO_4 has a vapor pressure of nearly 100 Torr at room temperature, which is around a factor of 100 higher than the TTIP precursor used for the growth of titanates. Secondly, the ruthenium cation is bonded to four oxygen atoms in the molecule, providing an additional source of oxygen and assisting in overcoming the problem of oxygen deficiency. This approach has the potential to enable the reproducible, systematic crystal growth necessary to carry out studies to explore the unique emergent phases of the strontium ruthenate series.

5.2 Hybrid MBE Growth of Sr_2RuO_4

Here we will discuss the growth of the $n = 1$ Ruddlesden-Popper phase Sr_2RuO_4 using the RuO_4 precursor. In this approach Sr is supplied from a high-purity metallic charge in a conventional effusion cell while Ru is supplied in the form of the RuO_4 precursor. The RuO_4 precursor has previously been used in the synthesis of Ru, RuO_2, and $SrRuO_3$ films, but has not yet been used in MBE growth [103]–[105]. The resulting

Sr_2RuO_4 films possess excellent structural quality as evidenced by a number of characterization techniques, demonstrating that the use of the RuO_4 precursor is a viable technique for the growth of high-quality thin films of Sr_2RuO_4 other members of this fascinating class of materials.

5.2.1 Details of Growth Technique

Sr_2RuO_4 thin films were grown on single crystal (001) $(LaAlO_3)_{0.3}(Sr_2AlTaO_6)_{0.7}$ (LSAT) substrates in an oxide MBE system (GEN 930, Veeco Instruments). The in-plane lattice constants of Sr_2RuO_4 and LSAT are almost identical at 3.87 Å, resulting in almost no elastic strain building up in the film. The substrates were etched in a 3:1 $HCl:HNO_3$ solution prior to growth to provide smooth stepped surfaces. A 350 nm thick layer of Ta was deposited by e-beam evaporation on the back of the substrates to facilitate heat transfer between the substrate heater and the growth surface. The films were grown by co-deposition, with the Sr supplied by a high purity elemental source in a conventional low-temperature effusion cell. Ruthenium was supplied by the RuO_4 precursor. The precursor was supplied by Air Liquide (Fremont, CA) under the brand name Torus. Due to the unstable nature of the precursor, it is packed in a solution of fluorinated ethers. The solution consists of only about 1% by weight of the RuO_4 precursor. The precursor cylinder was maintained at room temperature, which is high enough to supply sufficient vapor pressure for delivery to the chamber with no additional heating. The precursor was

delivered to the chamber via a stainless steel tube that was heated to near 50 °C to prevent condensation of the precursor. A linear leak valve and a capacitive manometer were used to monitor and control the flow of the precursor. The precursor was introduced to the growth chamber with a gas injector heated to 50 °C. Additional oxygen was supplied with an RF plasma source operating at 300 W. The background pressure of oxygen in the chamber was 5×10^{-6} Torr. In-situ monitoring of the growth surface was done with reflection high-energy electron diffraction (RHEED). Ex-situ characterization was performed with x-ray diffraction (XRD), atomic force microscopy (AFM), and transmission electron microscopy (TEM). Resistivity measurements of the films were performed at room temperature with Ohmic Au/Ti contacts deposited in a four-point van der Pauw geometry.

5.2.2 Optimizing Stoichiometry and Growth Temperature

The stoichiometry was optimized to obtain an idea of the Sr/Ru beam flux ratio (as measured by an ion gauge) needed for a phase pure film. This was done by maintaining the ruthenium flux at a constant value using the gas inlet system and varying the Sr effusion cell temperature to vary the flux. Like the growth of $SrTiO_3$, RHEED patterns provided a sensitive probe of film stoichiometry. The post-growth RHEED patterns of three films grown using varying Sr fluxes are shown in Figure 5.1 along the [100] and the [110] crystallographic directions. Film roughening caused modulations in the RHEED streaks in Sr-deficient film grown with a Sr cell temperature of 480 °C. Spottiness is especially

noticeable along the [110] direction. This is likely linked to the formation of second phases within the film, which will be discussed further in Section 5.3. Chevron patterns in the Sr-rich film grown at 498 °C indicated that excess Sr was accumulating on the surface and forming metal droplets. The stoichiometric film grown at a cell temperature of 488 °C produced the smoothest and most intense RHEED patterns along both the [100] and [110] directions, indicating the smoothest film surface and best crystal quality.

The effect of the substrate temperature was explored by growing stoichiometric films using varying substrate temperatures (as measured by a thermocouple mounted behind the sample). The substrate growth temperature was found to have a dramatic effect on the quality of the film, with very high temperatures being necessary for good film quality. Sr_2RuO_4 films grown at a substrate temperature of 900 °C showed poor structural characteristics in both XRD and RHEED. At 920 °C, the films showed improved structural characteristics with sharper Bragg peaks and smoother surfaces. However, it wasn't until a substrate temperature of 950 °C that both XRD and RHEED measurements revealed a truly high-quality crystal structure. This trend is evident in the wide-angle XRD scans of the films grown at various temperatures in Figure 5.2.

The room temperature resistivity followed a similar trend with the growth temperature. The resistivity of the film grown at 900 °C was too high to be measured. The resistivity of the film grown at 920 °C was 1100 $\mu\Omega$cm. Finally, the resistivity of the film grown at 950 °C was 230 $\mu\Omega$cm, which is close to the room temperature resistivity

measured in bulk samples. From this point forward, all results shown will be from a film grown with optimal stoichiometry grown at a substrate temperature of 950 °C.

5.2.3 Growth Mode and Structural Characterization

Growth proceeded in a layer-by-layer mode, evidenced by the onset of RHEED oscillations as seen in Figure 5.3 (a). This is a desirable growth mode, as it is evidence of high adatom mobility on the growth surface and allows for excellent control over film thickness. The initial behavior of the RHEED intensity (around 200 seconds into growth) appears slightly anomalous compared to the rest of the oscillations. This may be caused by the creation of anti-site defects due to the change in symmetry from the cubic LSAT substrate to the tetragonal Sr_2RuO_4 film, a behavior that was previously observed during PLD growth [101]. The period of the oscillations corresponds to a growth rate of 16 nm/hour, meaning that there are two intensity oscillations per Sr_2RuO_4 unit cell, a periodicity that has been observed by others [106]. The layer-by-layer growth mode observed here typically results in very smooth post-growth surfaces, which is confirmed in the AFM image of Figure 5.3 (b). The features in the image are on the order of the unit cell height of Sr_2RuO_4 of 12.74 Å.

The excellent structural quality is confirmed in the wide angle XRD scan of Figure 5.4 (a). The 002, 004, 006, 008, and 00$\underline{10}$ Bragg peaks of Sr_2RuO_4 are all present, with the spacing indicating a unit cell height of 12.74 Å, in nearly exact agreement with previous measurements of bulk Sr_2RuO_4 crystals [107]. No additional peaks are present, confirming

the phase purity of the film. This is noteworthy, as other phases of the Ruddlesden-Popper series are possible, which would result in mixed-phase films with deteriorated properties. A high resolution XRD scan of the 006 Sr_2RuO_4 and 002 LSAT peak is shown in Figure 5.4 (b). The pronounced Laue fringes emanating from the Sr_2RuO_4 peak are evidence of a very smooth film/substrate interface and film surface. The period of the Laue fringes corresponds to a film thickness of 29 nm, which is in excellent agreement with the thickness derived from the spacing of the RHEED intensity oscillations. This implies that the flux does not vary significantly during growth, a situation that offers precise control of stoichiometry and the Sr_2RuO_4 film thickness. The rocking curve full width at half maximum of 0.075°, shown in Figure 5.5, provides further evidence of the excellent crystallinity.

A cross-sectional image taken by high-angle annular dark field (HAADF) scanning transmission electron microscopy (STEM) is seen in Figure 5.6. The image confirms the tetragonal structure and $n = 1$ layering of the Sr_2RuO_4 unit cell, with none of the other Ruddlesden-Popper phases present. It is also confirms that growth took place with the *c*-axis along the growth direction.

In summary, phase-pure epitaxial thin films of Sr_2RuO_4 have been synthesized using a hybrid molecular beam epitaxy approach incorporating a precursor solution containing the volatile and highly reactive molecule RuO_4. The structural quality of the films is excellent, as evidenced by several characterization techniques. This method enables excellent control of stoichiometry and phase purity, and the layer-by-layer growth

mode allows for highly smooth interfaces and surfaces and fine control of film thickness. The structural quality demonstrates the potential of this precursor to be used in the growth of other members of the fascinating strontium ruthenate Ruddlesden-Popper series, and the control it offers is ideal for the growth of heterostructures comprised of these materials.

5.3 Hybrid MBE Growth of the $Sr_{n+1}Ru_nO_{3n+1}$ Series

In addition to Sr_2RuO_4, other members of the strontium ruthenate family, especially the n = 2 $Sr_3Ru_2O_7$ and $n = \infty$ $SrRuO_3$ phases, are of scientific interest. The growth of epitaxially strained thin films could offer unique insight into their emergent low temperature electronic and magnetic phases. The growth of these materials was explored using hybrid MBE technique incorporating the volatile RuO_4 previously discussed for the growth of Sr_2RuO_4.

A method of approaching this is by considering the relative content of Sr and Ru in each of the phases. Examining the formula units in the $Sr_{3n+1}Ru_nO_{3n+1}$ series, we note that the Sr/Ru ratio is maximum for n = 1 Sr_2RuO_4 (Sr/Ru = 2), decreases to an intermediate value for $n = 2$ $Sr_3Ru_2O_7$ (Sr/Ru = 1.5), and continues decreasing to the limit of $n = \infty$ $SrRuO_3$ (Sr/Ru = 1). Therefore, an obvious approach to stabilizing the various phases during MBE growth is by varying the ratio of the Sr and Ru fluxes. This was attempted by holding the flux of the RuO_4 precursor constant while systematically reducing the Sr flux by lowering the Sr effusion cell temperature. The results are summarized in the series of wide angle XRD scans in Figure 5.7. It was found that the Sr_2RuO_4, $Sr_3Ru_2O_7$, and $SrRuO_3$

phases were stabilized at Sr effusion cell temperatures of 488 °C, 475 °C, and 470 °C, respectively, with the flux of the RuO_4 precursor and the substrate temperature held constant. The resulting films were phase-pure with no unexpected Bragg reflections observed. However, it was found that mixed-phase films were possible if the Sr/Ru ratio was set to a value intermediate to those of two of the Ruddlesden-Popper phases.

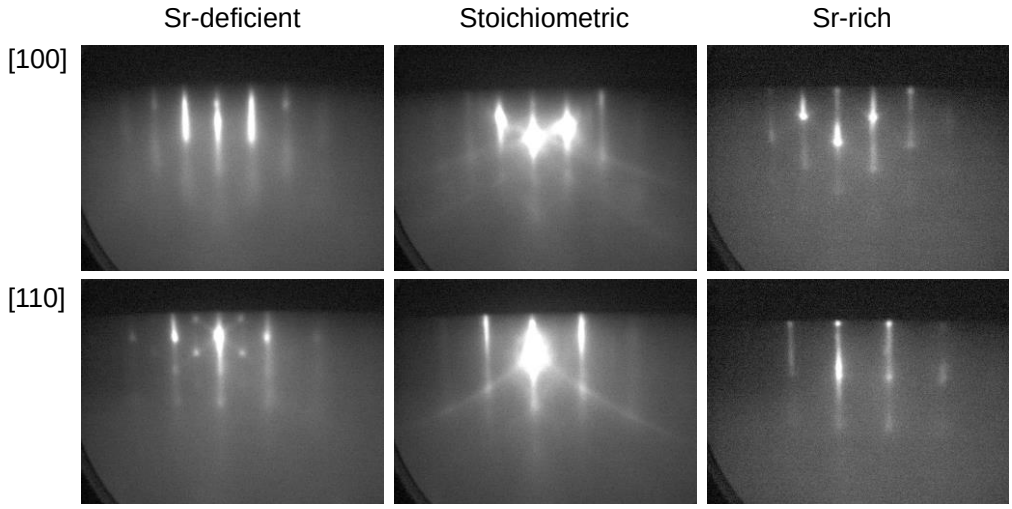

Figure 5.1 Post-growth RHEED patterns of Sr_2RuO_4 films of varying stoichiometry. From left to right, the strontium cell temperature was set to 480 °C (Sr-deficient), 488 °C (stoichiometric), and 498 °C (Sr-rich). Reprinted from P. B. Marshall, H. Kim, K. Ahadi, and S. Stemmer, APL Materials 5, 096101 (2017). This article is distributed under a Creative Commons Attribution 4.0 (CC BY 4.0) license (https://creativecommons.org/licenses/by/4.0/). (Ref. [82]).

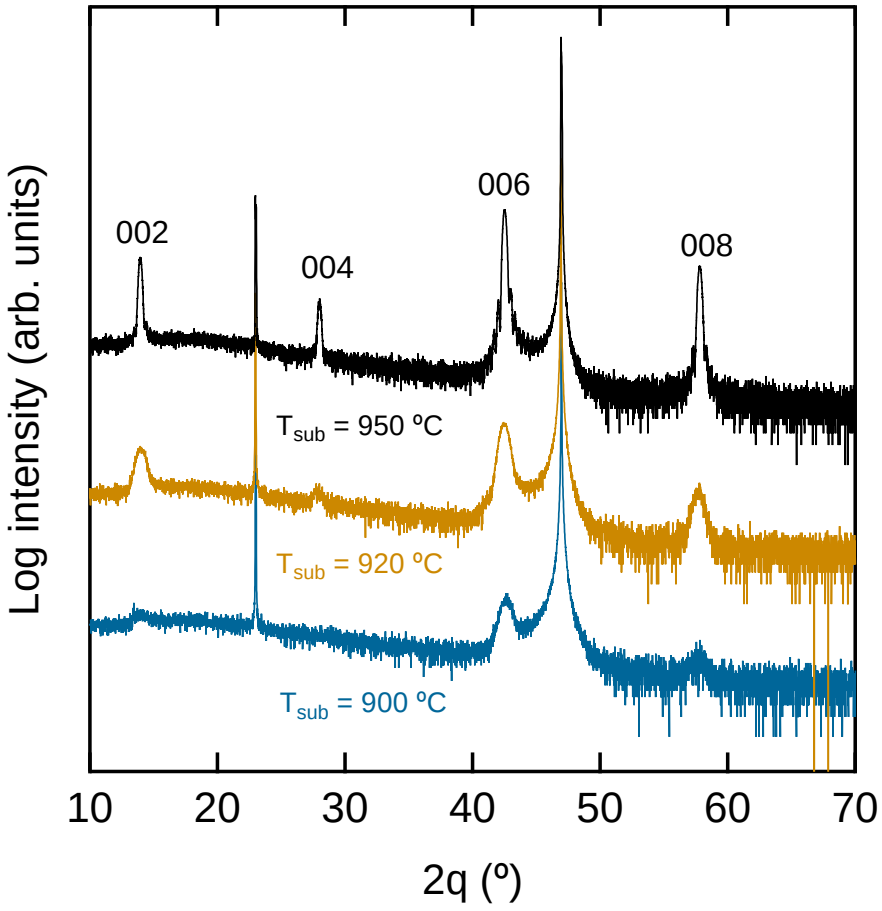

Figure 5.2 Wide angle XRD scans of Sr_2RuO_4 films grown at 900 °C (bottom), 920 °C (middle), and 950 °C (top), showing a clear trend with increasing crystallinity at higher growth temperatures.

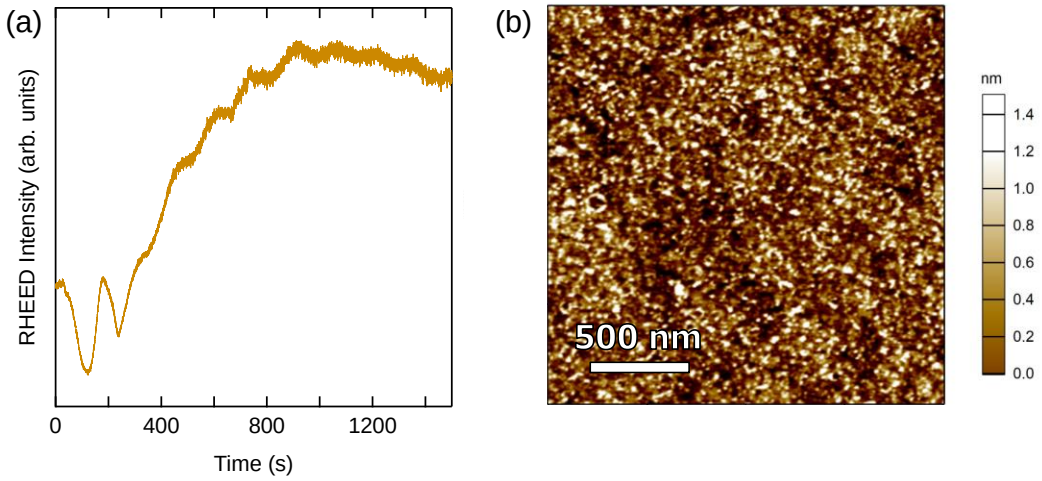

Figure 5.3 (a) RHEED intensity oscillations showing the growth of Sr_2RuO_4 commencing in a layer-by-layer mode. (b) 2×2 μm AFM image confirming smooth post-growth surface of a Sr_2RuO_4 thin film. Reprinted from P. B. Marshall, H. Kim, K. Ahadi, and S. Stemmer, APL Materials 5, 096101 (2017). This article is distributed under a Creative Commons Attribution 4.0 (CC BY 4.0) license (https://creativecommons.org/licenses/by/4.0/). (Ref. [82]).

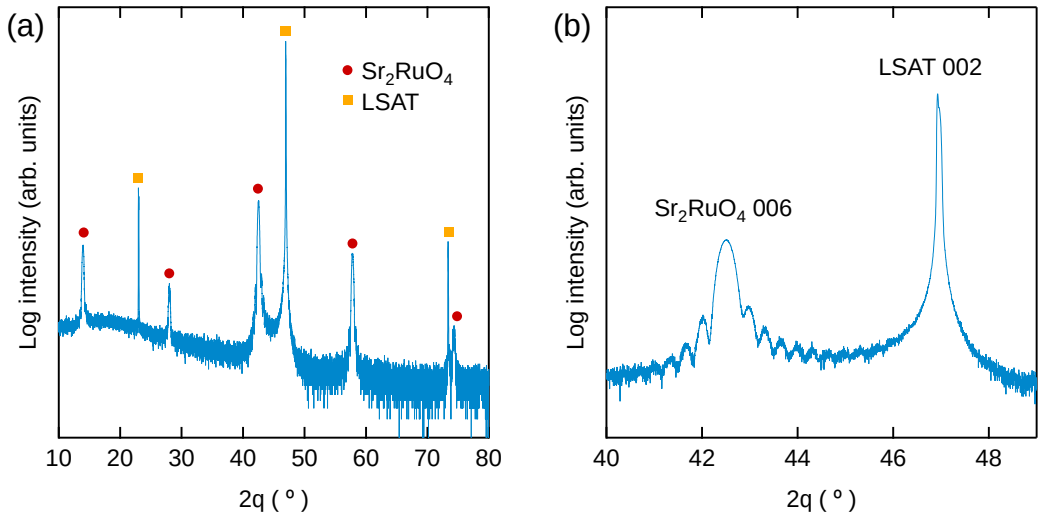

Figure 5.4 (a) Wide-angle XRD scan showing high purity and structural quality of a Sr_2RuO_4 film grown on an LSAT substrate. From left to right, the Sr_2RuO_4 Bragg peaks are 002, 004, 006, 008, and 00$\underline{10}$. (b) High resolution XRD scan of the 006 Sr_2RuO_4 peak and the 002 LSAT peak showing prominent Laue fringes indicating a smooth film with a thickness of 29 nm. Reprinted from P. B. Marshall, H. Kim, K. Ahadi, and S. Stemmer, APL Materials 5, 096101 (2017). This article is distributed under a Creative Commons Attribution 4.0 (CC BY 4.0) license (https://creativecommons.org/licenses/by/4.0/). (Ref. [82]).

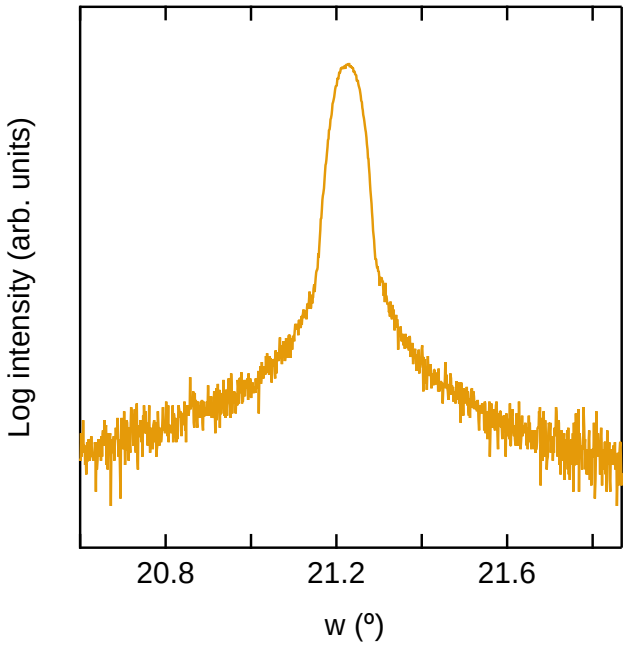

Figure 5.5 Rocking curve of the 006 peak of the Sr_2RuO_4 film. The full width at half maximum is 0.075°. Reprinted from P. B. Marshall, H. Kim, K. Ahadi, and S. Stemmer, APL Materials 5, 096101 (2017). This article is distributed under a Creative Commons Attribution 4.0 (CC BY 4.0) license (https://creativecommons.org/licenses/by/4.0/). (Ref. [82]).

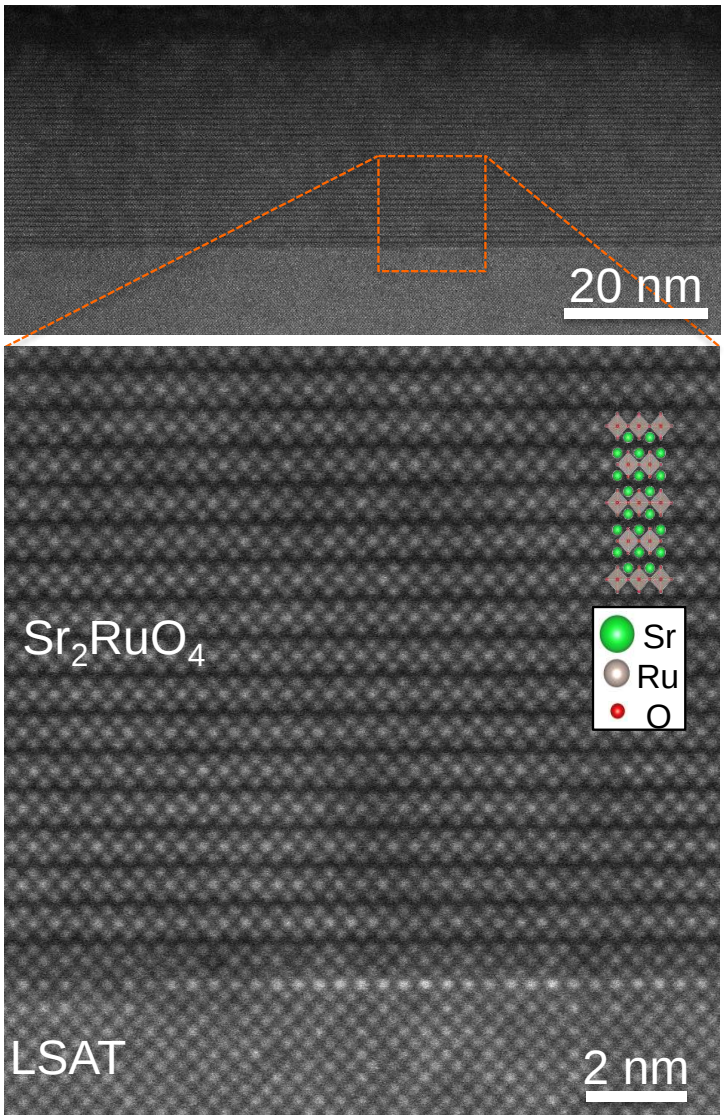

Figure 5.6 HAADF-STEM images of a Sr_2RuO_4 thin film grown epitaxially on LSAT. (a) Smooth interfaces with no extended defects are visible in the large field of view. (b) The tetragonal structure of the Sr_2RuO_4 with the *c*-axis parallel to the growth direction can be resolved under higher magnification. Reprinted from P. B. Marshall, H. Kim, K. Ahadi, and S. Stemmer, APL Materials 5, 096101 (2017). This article is distributed under a Creative Commons Attribution 4.0 (CC BY 4.0) license (https://creativecommons.org/licenses/by/4.0/). (Ref. [82]).

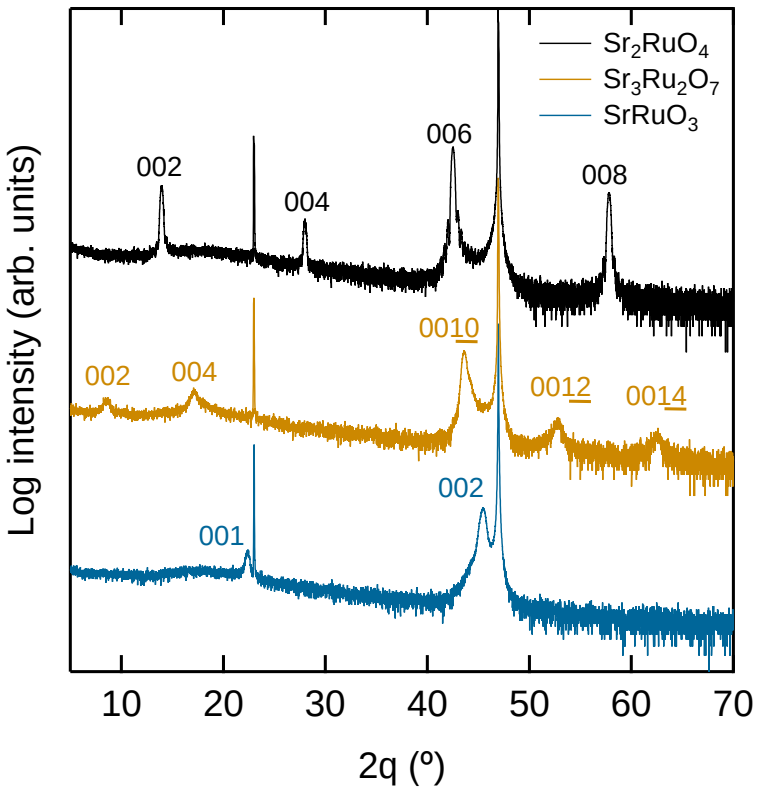

Figure 5.7 Wide angle XRD scans of various Ruddlesden-Popper phases grown at different Sr/Ru flux ratios. With the RuO_4 precursor flux held constant, the Sr_2RuO_4, $Sr_3Ru_2O_7$, and $SrRuO_3$ phases were stabilized at Sr effusion cell temperatures of 488 °C, 475 °C, and 470 °C, respectively.

Chapter 6 Nematic Transport Behavior in a Strained $Sr_3Ru_2O_7$ Thin Film

6.1 Introduction

Among the non-magnetic members of the $Sr_{n+1}Ru_nO_{3n+1}$ series, the $n = 2$ phase $Sr_3Ru_2O_7$ is the closest to a magnetic instability. Strong magnetic fluctuations have been observed in bulk samples via neutron scattering. Fluctuations of ferromagnetic order were found to emerge below 150 K, which transitioned to fluctuations of antiferromagnetic order upon cooling below 20 K [108]. A peak in the magnetic susceptibility occurs at this transition temperature. Additionally, it hosts a metamagnetic transition, which is a transition from a lowly polarized paramagnetic state to a highly-polarized ferromagnetic state through the application of an external magnetic field [67]. This transition occurs at a field of approximately 5 T when the field is oriented in-plane and 8 T when the field is oriented out-of-plane. The magnetic instability is related to magnetic field-tuned instabilities of the Fermi surface. In bulk crystals of $Sr_3Ru_2O_7$ sharp peaks in the magnetoresistance are observed at the critical fields, likely arising from enhanced scattering off of critical fluctuations of the Fermi surface near the transition.

More recently, evidence of a nematic phase has been found in studies of the in-plane transport [68]. Strong anisotropy in the magnetoresistance was observed at temperatures below 1 K in the vicinity of the metamagnetic transition, with the direction of the anisotropy being controlled by the direction of the applied magnetic field relative to the applied current used to measure the resistance. Neutron scattering studies have revealed that the nematic anisotropic behavior observed in the transport is likely related to

magnetic field-controlled spin density wave (SDW) phases that form in the vicinity of the metamagnetic transition [69]. The nematic behavior in bulk crystals has been observed with the applied field oriented along the *c* axis.

Many of these unusual properties can be linked to underlying features of the Fermi surface. In particular, the Fermi surface of $Sr_3Ru_2O_7$ has been found to be both strongly nested and in close proximity to a Van Hove singularity, a phenomenon introduced in Section 1.6 [72]. The flat features in the band structure near the Van Hove singularity lead to a divergence of the density of states which lies close to the Fermi level, making the Fermi surface especially susceptible to breakdown into anisotropic and magnetic states due to enhanced screening. Subtle modification of the lattice structure should be expected to modify the energy spacing between the Van Hove singularity and the Fermi level and therefore affect the emergent magnetic phases. For example, small amounts of uniaxial pressure have been found to induce ferromagnetic order in bulk samples of $Sr_3Ru_2O_7$ [109].

We may then ask what the effect of epitaxial strain may be on these phenomena. The control over the strain state offered by epitaxial growth may be expected to offer control of the electronic and magnetic interactions via modifications of the Fermi surface, making this material an excellent platform to study ordered phases emerging from strong correlations, quantum criticality, and their relationship to the underlying band structure. It is possible that modifications of the Fermi surface may give rise to entirely new types of electronic or magnetic order. In this study we explore the transport properties and magnetization of compressively stressed $Sr_3Ru_2O_7$ films grown using the hybrid MBE

technique discussed in Chapter 5. Anisotropy in the magnetoresistance, where the applied magnetic field controls the orientation, is revealed in low-temperature magnetotransport measurements, similar to previous measurements on bulk samples. However, it was found that the anisotropy in the thin film samples persists to an order of magnitude higher temperatures. Additionally, an itinerant antiferromagnetic state observed at low temperatures gives rise to anisotropies in the in-plane resistivity, with anisotropic non-Fermi-liquid scattering suggesting the presence of critical fluctuations affecting certain regions of the Fermi surface.

6.2 Growth and Measurement Details

$Sr_3Ru_2O_7$ thin films were grown epitaxially on cubic $(LaAlO_3)_{0.3}(Sr_2AlTaO_6)_{0.7}$ (LSAT) substrates using the hybrid MBE technique incorporating the volatile RuO_4 precursor molecule detailed in Chapter 5 [82]. The growth was carried out using an RF oxygen plasma source at a power of 300 W with a background oxygen pressure maintained near 5×10^{-6} Torr. The thickness of the $Sr_3Ru_2O_7$ film on which the magnetization and transport measurements were taken for this study was 20 nm. Ohmic 40 nm thick Ti contacts were deposited on the corners of the sample in van der Pauw geometry, with 400 nm thick Au pads deposited on top to facilitate wire bonding. In-plane sheet resistance and magnetoresistance measurements were performed in a Quantum Design Physical Property Measurement system capable of reaching a base temperature of 2 K. The magnetoresistance measurements were performed with the applied magnetic field, B, in

the ab plane of the sample along the $\langle 100 \rangle$ family of directions. The resistance was measured along both the [100] and [010] directions, a configuration which yields measurements both parallel and transverse to the applied magnetic field. The magnetization measurements were carried out in a Quantum Design SQUID magnetometer.

6.3 Structural Characterization of the $Sr_3Ru_2O_7$ Film

The wide-angle XRD scan in Figure 6.1 reveals a phase-pure $Sr_3Ru_2O_7$ film. From left to right, the 002, 004, 00$\underline{10}$, 00$\underline{12}$, and 00$\underline{14}$ Bragg reflections are present. The absence of the 006 and 008 reflections can be explained by their low structure factors and the low film thickness leading to a signal that is too weak to be distinguished from the noise.

The cross-section high-resolution TEM image Figure 6.2 confirms the absence of misfit dislocations, demonstrating that the film is coherently strained to the substrate. Growth took place with the (001) plane of the tetragonal unit cell parallel to the film surface, meaning that the c-axis is out of plane. The only occasional defects are regions of the n = 3 phase intermixed with the otherwise pure n = 2 layering of $Sr_3Ru_2O_7$.

6.3 Transport and Magnetization Results

The $Sr_3Ru_2O_7$ film remained metallic from 300 K down to a temperature of 2 K, as seen in the $\rho(T)$ curve in Figure 6.3 (a). The derivative $d\rho(T)/dT$ is plotted in Figure 6.3

(b). We notice two distinct features in the curve as the temperature is reduced from room temperature: one occurring near 165 K and the second near 40 K. It is likely that these features arise from magnetic transitions.

The magnetization of the film was measured at 50 K and 2 K, seen in Figure 6.4 (a) and (b), respectively. At 50 K weak ferromagnetic order is observed with a small amount of hysteresis with a coercive field of 100 Oe. At 2 K the coercivity vanishes, hinting that the ferromagnetic order has transitioned to antiferromagnetic order.

Magnetoresistance curves at various temperatures from 300 down to 2 K are shown in Figure 6.5. The magnetoresistance was measured with the applied current I in the direction of the applied magnetic field ($B \parallel I$, parallel configuration) and with the applied current perpendicular to the magnetic field ($B \perp I$, transverse configuration). Above 40 K, negative magnetoresistance is observed in both directions, consistent with the ferromagnetism seen in the magnetization at higher temperatures. Below 40 K an anisotropy begins to set in, with a transition to positive magnetoresistance in the transverse configuration while the parallel configuration retains its negative magnetoresistance. A prominent magnetoresistance peak sets in with a maximum at 5 T in the transverse configurations near 5 K, while it is suppressed in the parallel configuration. At fields exceeding 5 T the behavior of the two configurations becomes similar with a linear negative magnetoresistance signifying the completion of the metamagnetic transition and the onset of ferromagnetism.

The in-plane resistance offers a different perspective of this anisotropy. The resistance normalized to its value at 2 K, $R(T)/R(2\ K)$, is shown in Figure 6.6 (a)-(c) at magnetic fields of 0, 5, and 9 T in both the parallel and transverse configurations. In the absence of a field the behavior is isotropic. At the critical metamagnetic field of 5 T in Figure 6.6 (b) evidence of enhanced scattering is seen in the transverse configuration, while the behavior in the parallel configuration remains unchanged. Finally, upon further increasing the field to 9 T (which pushes the magnetic ordering into the ferromagnetic state beyond the metamagnetic transition), the enhanced scattering in the transverse configuration appears to be suppressed with a return to nearly isotropic behavior.

A more quantitative analysis is possible by plotting the quantity $\log(dR/dT)$ on a scale of $\log(T)$, as seen in Figure 6.7 (a)-(c). Assuming that the resistivity follows a power-law of the form $R = R_0 + AT^n$, the exponent n is related to the slope of the curve according to the equation $n = slope + 1$. The black dotted line in Figure 6.7 (a) is a fit with n set to 2 to demonstrate Fermi liquid behavior. Again, isotropic behavior is observed in the absence of a field with n being close to the Fermi liquid value for both configurations. At the critical field of 5 T enhanced scattering is again seen in the transverse configuration with an n that is close to 1.6, while the resistance in the parallel configuration retains its Fermi liquid character. The intercept with the vertical axis of the transverse configuration, given by $\log(nA)$, is higher than that of the parallel configuration. This is suggestive of effective mass enhancement, as $A \propto m^*$. Finally, at a field of 9 T,

isotropic behavior is recovered. The resistance in the transverse configuration displays a return to Fermi liquid behavior and the intercept returns to its original value.

6.4 Discussion

In bulk samples of $Sr_3Ru_2O_7$ magnetic fluctuations have been observed by neutron scattering [108]. However, no long-range magnetic order is typically observed. In the present strained thin film sample weak long-range ordering is present, with ferromagnetism emerging below 165 K with a transition to antiferromagnetic ordering below 40 K. This reflects the neutron scattering studies of bulk $Sr_3Ru_2O_7$, which found a similar transition from ferromagnetic to antiferromagnetic-like character in the fluctuations as the temperature was reduced below 20 K [108]. Thus, it appears that while a similar transition in the character of the magnetism is observed in the thin film sample, the epitaxial strain has enhanced the magnetic interactions and induced true long-range magnetic order. This is not surprising, as previous studies of uniaxial pressure applied to bulk samples revealed ferromagnetism at a pressure of only 0.1 GPa [109]. Here, using the elastic tensor of $Sr_3Ru_2O_7$, we can estimate the effective pressure to be near 1.1 GPa based on the lattice mismatch, well exceeding 0.1 GPa.

At temperatures below 20 K, past the transition to antiferromagnetic behavior, the magnetoresistance becomes anisotropic and is strongly affected by the direction of the applied magnetic field, consistent with electron nematic behavior. Neutron scattering studies revealed that SDWs are the likely origin of the field-controlled nematicity observed

in bulk $Sr_3Ru_2O_7$. SDWs are known to cause resistivity anisotropy by removing states from regions of the Fermi surface at directions determined by the SDW ordering vector. Therefore, the anisotropy observed in the strained films, which is sensitive to the direction of the applied field, suggests that the applied field is controlling the direction of SDW order. Previous studies of bulk $Sr_3Ru_2O_7$ revealed two SDW phases with maximum critical temperatures below 1 K [69]. These phases only formed in a narrow range of magnetic fields around the metamagnetic transition. This contrasts with the thin film $Sr_3Ru_2O_7$, in which anisotropic nematic behavior is observed at low magnetic fields and at temperatures up to 20 K, which is over an order of magnitude higher than the nematic behavior observed in bulk samples. At 20 K the bulk samples displayed only fluctuations of antiferromagnetic order. A phase diagram in $B - T$ phase space is illustrated in Figure 6.8, where the green region marks the conditions in which nematic behavior is observed. The black data points correspond to positions of the maxima in the magnetoresistance in the transverse configuration at the various temperatures in Figure 6.5. The structure of the SDW order is likely different than the SDW phases observed in bulk $Sr_3Ru_2O_7$. An in-plane magnetic field caused an increase in the resistivity when oriented parallel to the current in bulk samples, while it induces negative magnetoresistance in the strained films. Additionally, the nematic behavior in bulk crystals has been observed with the magnetic field along the c axis (corresponding to the magnetoresistance peak near 8 T) while the nematic behavior in the present in the strained film is observed with the magnetic field in the ab plane (corresponding to the 5 T magnetoresistance peak).

The peak in the magnetoresistance at 5 T in the strained film is in close agreement with the peak position in bulk crystals when the field is oriented in the ab plane. The resistance maximum at 5 T marks the metamagnetic transition in both types of samples. This is accompanied by non-Fermi liquid scattering behavior in bulk $Sr_3Ru_2O_7$. Non-Fermi liquid scattering is also present in the strained film, as demonstrated in Figure 6.7. However, in the strained film the non-Fermi liquid behavior is anisotropic, with its direction being sensitive to the direction of the applied field. There are very few reports of this type of behavior. At fields exceeding 5 T, quasi-linear negative magnetoresistance is observed in both the parallel and the transverse configurations, which is similar to the negative magnetoresistance observed in the intermediate temperature regime. This marks a ferromagnetic phase with isotropic Fermi liquid scattering behavior. The isotropy reflects the fact that ferromagnetism is known to affect the entire Fermi surface.

The likely origin for the observed differences between bulk and strained films is the epitaxial strain imparted by the substrate. Small amounts of uniaxial pressure have previously been demonstrated to greatly affect the magnetism in $Sr_3Ru_2O_7$ [109]. The epitaxial strain in this study was the result of the lattice mismatch between the cubic LSAT substrate (a = 3.868 Å) and the pseudocubic in-plane lattice parameter of $Sr_3Ru_2O_7$ of 3.888 Å. This yields a biaxial compressive stress of 1.1 GPa as calculated using the elastic tensor of $Sr_3Ru_2O_7$ [110]. The strain modifies the shape of the Fermi surface, as well as the proximity of the Fermi level to any singularities, which in turn affects the low temperature transport properties. This has been demonstrated for Sr_2RuO_4, where an

enhancement of the critical temperature for superconductivity has been observed under uniaxial pressure [111], [112].

SDWs are often observed in metals with strongly nested Fermi surfaces. The observation of a SDW phase over much larger regions of $B - T$ space in the strained film compared to bulk suggests that the compressive in-plane strain may have enhanced Fermi surface nesting. The origin of the metamagnetic transition in bulk $Sr_3Ru_2O_7$ may be a Van Hove Singularity in the underlying band structure, which gives rise to a diverging density of states near the Fermi level. Zeeman splitting from an applied magnetic field can shift the position of the singularity closer to the Fermi level, thereby causing instability to the emergence of a ferromagnetic state. Theoretical work has shown that the critical field and temperature at which metamagnetic transition is observed are strongly related to the energy separation between the Fermi level and a Van Hove Singularity [113]. Metamagnetic transitions between anisotropic and isotropic phases are associated with rapid fluctuations of the Fermi surface topology, known as a Lifshitz transition [114], [115]. The observation of anisotropic non-Fermi liquid scattering, enhanced scattering causing the magnetoresistance peak, and the enhancement of the effective mass near the critical transition depend on the orientation of the applied magnetic field highlight the connection between the emergent properties of $Sr_3Ru_2O_7$ and field-tuned Fermi surface instabilities. The epitaxial strain strongly modifies these instabilities.

Finally, we observe that linear negative magnetoresistance was observed in two distinct regions in phase space where ferromagnetic order was present. The strong

similarity in two distinct regions of phase space suggests that this behavior is intrinsic to the ferromagnetic state, which affects the Fermi surface isotropically (no transport anisotropies were observed in these regions of phase space). Some theory work has predicted a transition between open and closed Fermi surfaces at the metamagnetic transition [115]. Other work has predicted negative magnetoresistance when the majority spin is shifted into a dispersive region of the Fermi surface at the transition [116]. These models are consistent with the observations in this study and highlight the close connection between the magnetotransport properties and the shape of the Fermi surface in $Sr_3Ru_2O_7$.

6.5 Conclusions

We have observed evidence of emergent ordered phases in compressively strained $Sr_3Ru_2O_7$ films grown by hybrid MBE that are similar to those observed in bulk crystals. These include nematic transport behavior and non-Fermi liquid behavior arising from a metamagnetic quantum critical point. However, it was found that modification of the lattice through epitaxial strain greatly influences the nature of these phases. The nematicity, likely arising from the onset of spin density wave order, was observed over a larger region of phase space as compared to bulk samples. The critical temperature for the onset of this behavior was observed at temperatures that were over an order of magnitude higher than in bulk samples. Anisotropic non-Fermi liquid behavior controlled by the direction of the applied field was observed, which has not yet been reported in bulk $Sr_3Ru_2O_7$. This study highlights how subtle perturbations of the lattice by epitaxial strain

can modify the Fermi surface, which in turn can have a dramatic effect on the emergent phenomena. Clearly, subtle aspects of the Fermi surface have a very large impact on the physics of the ruthenates. This demonstrates the possibility of employing strain engineering to design studies to obtain a greater understanding of the emergent phenomena in strongly correlated materials.

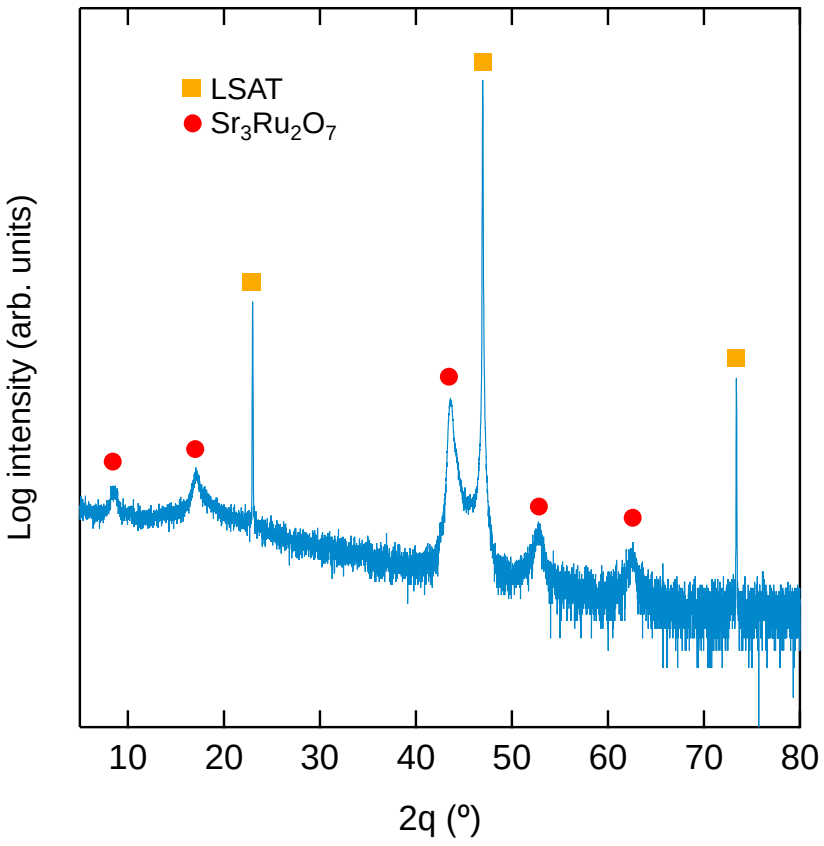

Figure 6.1 Wide angle XRD scan of a $Sr_3Ru_2O_7$ film (Bragg peaks marked by red circles) grown epitaxially on an LSAT substrate (marked by orange squares). From left to right, the $Sr_3Ru_2O_7$ peaks are 002, 004, 00$\underline{10}$, 00$\underline{12}$, and 00$\underline{14}$. Reprinted with permission from P. B. Marshall, K. Ahadi, H. Kim, and S. Stemmer, Physical Review B 97, 155160 (2018), Copyright 2018 by the American Physical Society (Ref. [39]).

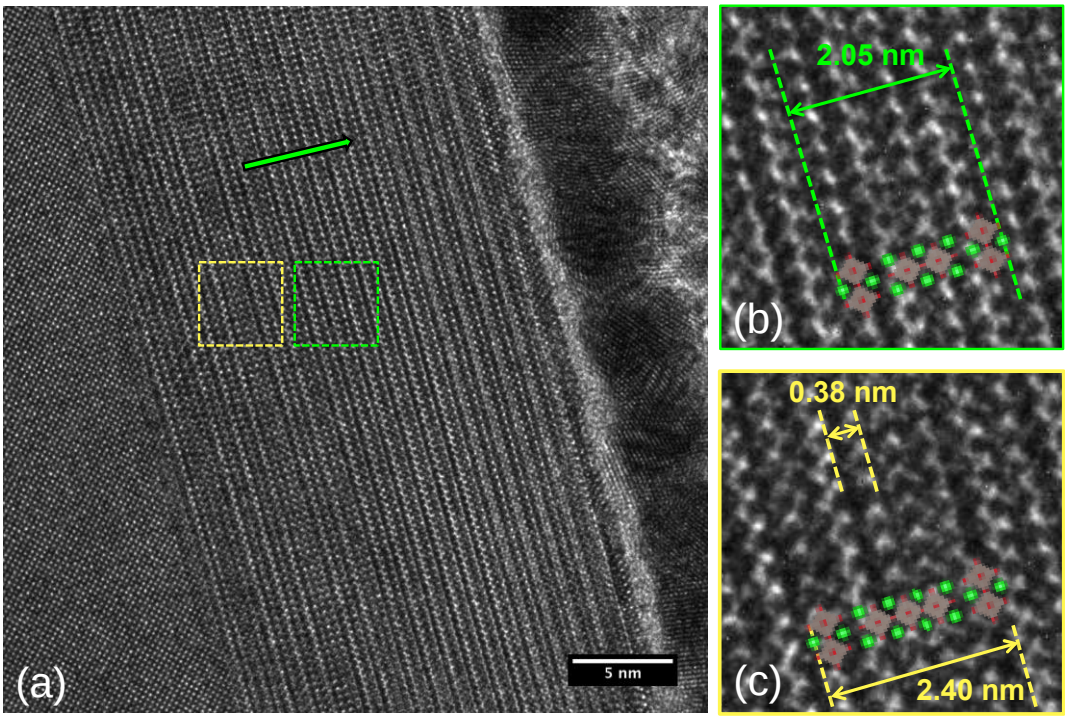

Figure 6.2 (a) TEM images of a $Sr_3Ru_2O_7$ film grown epitaxially on LSAT. The magnified image in (b) confirms the tetragonal structure of the unit cell with the c-axis out-of-plane along the growth direction. The film was fairly phase pure with the exception of occasional intermixed n = 3 layers as seen in (c). Reprinted with permission from P. B. Marshall, K. Ahadi, H. Kim, and S. Stemmer, Physical Review B 97, 155160 (2018), Copyright 2018 by the American Physical Society (Ref. [39]).

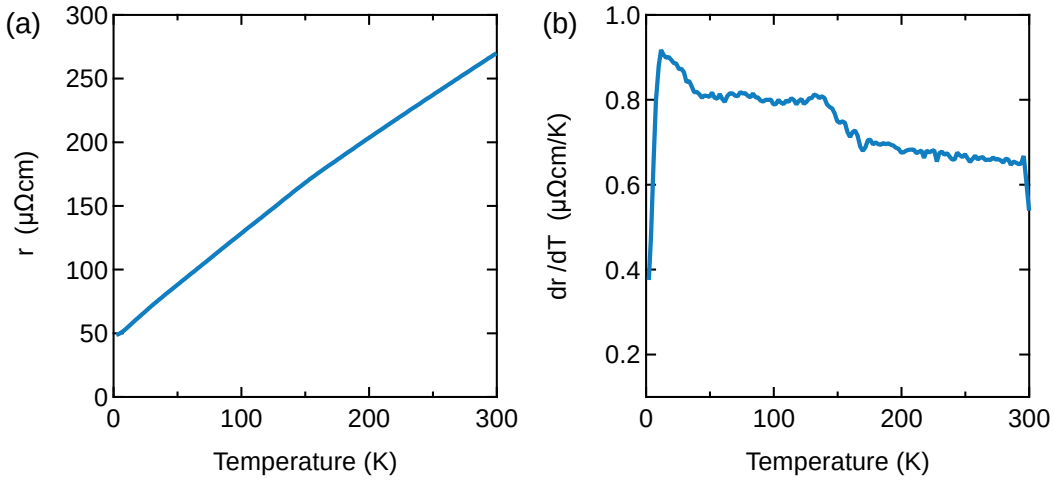

Figure 6.3 (a) Resistivity ρ as a function of temperature showing metallic behavior down to 2 K. (b) The derivative $d\rho/dT$ showing two abrupt changes at 165 K and 40 K. Reprinted with permission from P. B. Marshall, K. Ahadi, H. Kim, and S. Stemmer, Physical Review B 97, 155160 (2018), Copyright 2018 by the American Physical Society (Ref. [39]).

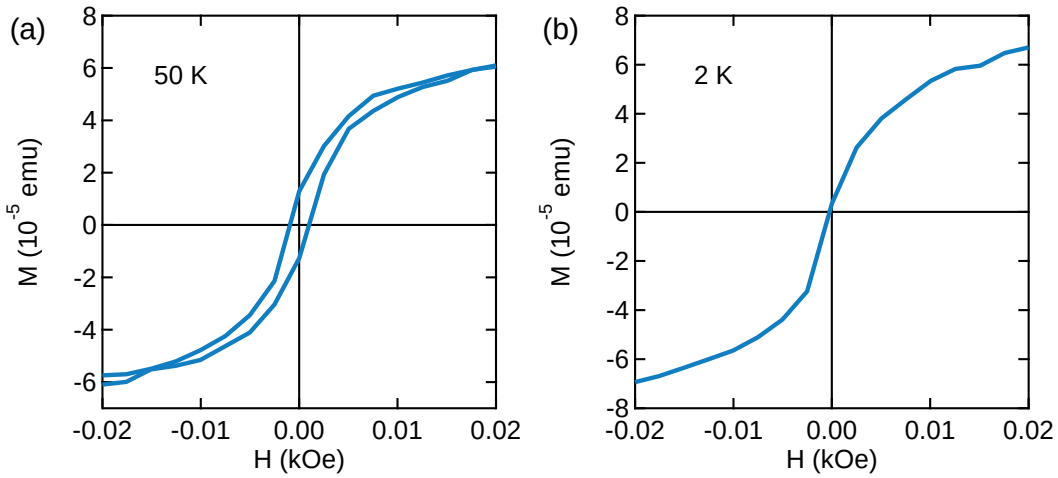

Figure 6.4 Magnetization as a function of applied field at (a) 50 K and (b) 2 K. The small coercive field at 50 K suggests that weak ferromagnetic order is present. The vanishing coercive field at 2 K suggests that a transition to magnetism of antiferromagnetic order has occurred. Reprinted with permission from P. B. Marshall, K. Ahadi, H. Kim, and S. Stemmer, Physical Review B 97, 155160 (2018), Copyright 2018 by the American Physical Society (Ref. [39]).

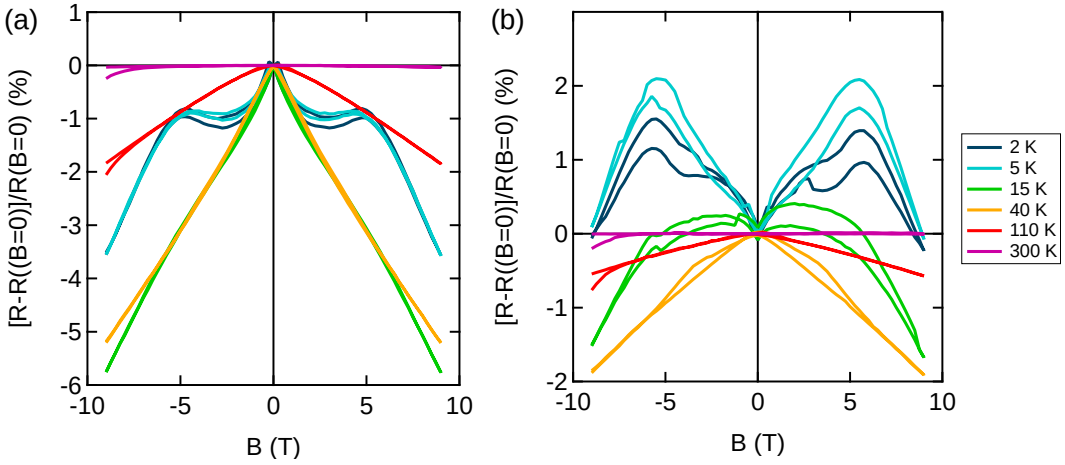

Figure 6.5 (a) Magnetoresistance (normalized to its value at $B = 0$) in the parallel configuration with $B \parallel I$. (b) Magnetoresistance in the transverse configuration with $B \perp I$. Above 40 K, negative magnetoresistance in both configurations is seen in the ferromagnetic phase. Below 40 K anisotropy sets in with positive magnetoresistance with $B \perp I$ and negative magnetoresistance with $B \parallel I$. Reprinted with permission from P. B. Marshall, K. Ahadi, H. Kim, and S. Stemmer, Physical Review B 97, 155160 (2018), Copyright 2018 by the American Physical Society (Ref. [39]).

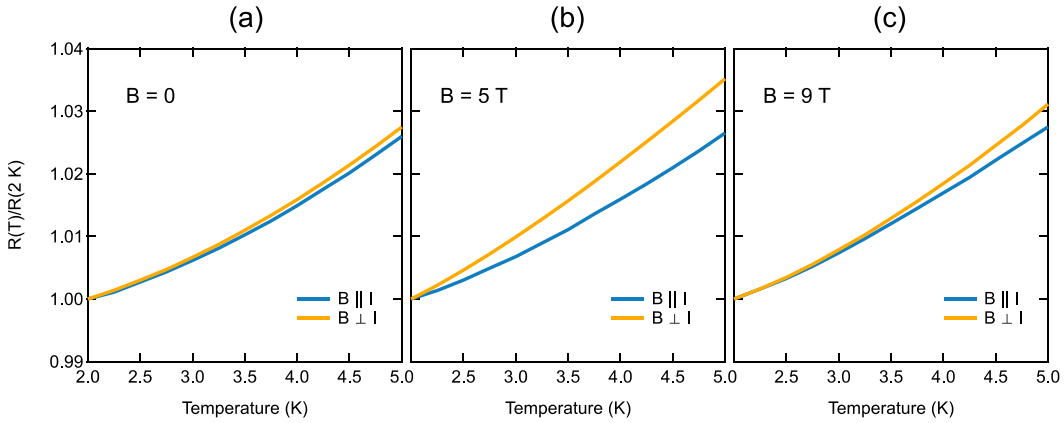

Figure 6.6 (a)-(c) In-plane resistance normalized to its value at 2 K, $R(T)/R(2\ K)$, for the parallel and transverse magnetic field directions with applied fields of 0, 5, and 9 T. Under zero applied field the temperature dependence is isotropic. Enhanced scattering in the transverse is configuration in the critical magnetic field of 5 T. Finally, isotropy is recovered at 9 T in the ferromagnetic state. Reprinted with permission from P. B. Marshall, K. Ahadi, H. Kim, and S. Stemmer, Physical Review B 97, 155160 (2018), Copyright 2018 by the American Physical Society (Ref. [39]).

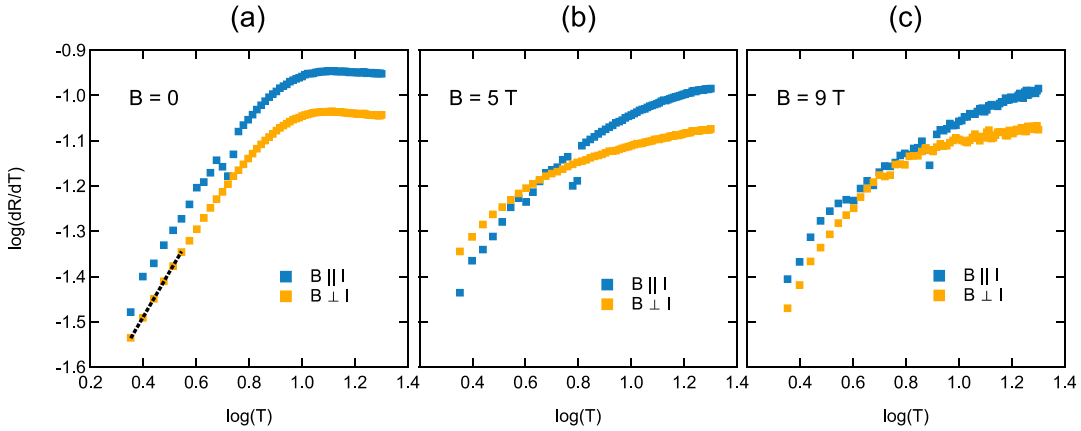

Figure 6.7 (a)-(c) The quantity $\log(dR/dT)$ plotted on a scale of $\log(T)$ for both current configurations at magnetic fields of 0, 5, and 9 T. The dotted black line in (a) is a fit with n set to 2 to demonstrate Fermi liquid behavior. Reprinted with permission from P. B. Marshall, K. Ahadi, H. Kim, and S. Stemmer, Physical Review B 97, 155160 (2018), Copyright 2018 by the American Physical Society (Ref. [39]).

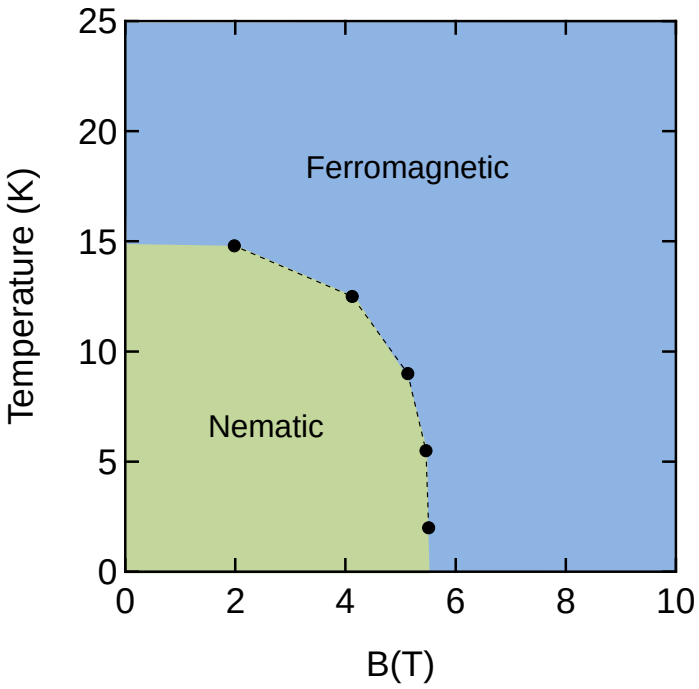

Figure 6.8 Phase diagram showing the region in $B - T$ space where nematic behavior is observed in the magnetoresistance of the $Sr_3Ru_2O_7$ film. The black points are the positions of the maxima in the magnetoresistance at various temperatures. The range of magnetic fields and temperatures in which nematic behavior is seen is much larger compared to previous studies of bulk samples. Reprinted with permission from P. B. Marshall, K. Ahadi, H. Kim, and S. Stemmer, Physical Review B 97, 155160 (2018), Copyright 2018 by the American Physical Society (Ref. [39]).

Chapter 7 Summary and Directions for Future Research

7.1 Summary of Work

The central aim of the research presented in this work was to explore the physics of transport and emergent phases in strongly correlated complex oxide thin films and to study how effects such as dimensionality, proximity magnetic materials, and lattice strain influenced or led to new types of emergent order. The use of the hybrid molecular beam epitaxy technique, introduced in Chapter 2.5, enabled the growth of heterostructures with layer thicknesses that could be controlled down to atomic dimensions and modification of the lattice using epitaxial strain. This allowed for the design of systematic experiments to explore how subtle modifications of the structure can in turn influence the properties of the ordered phases emerging at low temperatures. Experiments involving perovskite oxides with two B-site cations were presented: the ATiO$_3$ titanates (A=Sr, Gd, Sm), and the $Sr_{n+1}Ru_nO_{3n+1}$ Ruddlesden-Popper series. This allowed an investigation of the phenomenon of quantum criticality and emergent order from two perspectives: in the titanate system the external non-thermal tuning parameter was the SrTiO$_3$ quantum well thickness in RTiO$_3$/SrTiO$_3$/RTiO$_3$ (R = Gd, Sm) structures, while in the bilayer ruthenate $Sr_3Ru_2O_7$ the tuning parameter was the applied magnetic field.

In Chapter 3, a study of the electronic density of states in RTiO$_3$/SrTiO$_3$/RTiO$_3$ quantum wells was discussed. Tunnel junction devices were fabricated to enable tunneling spectroscopy measurements of the density of states in the correlated 2DEG residing in the SrTiO$_3$ well. A pseudogap state was observed in both quantum wells embedded in SmTiO$_3$

and $GdTiO_3$. However, the nature of the evolution of the pseudogap with quantum well thickness and temperature was distinct for the two barriers. In the thinnest $SmTiO_3$-embedded well, the onset of coherence peaks at low temperatures marked the emergence of a well-defined long-range coherent phase, which is likely an itinerant spin density wave state linked to the antiferromagnetic fluctuations induced by the barrier. In $GdTiO_3$, however, no coherent phases were found to emerge, and instead the pseudogap evolved to a true gap marking a structural distortion-induced metal-to-insulator transition. This highlights the importance in the nature of the magnetic interactions and the strength of coupling to the lattice in determining the behavior of the quasiparticle state.

In Chapter 4 a study involving the growth of similar quantum well structures on an alternative substrate was discussed. Rather than the cubic LSAT substrates used in the tunneling study, orthorhombic $DyScO_3$ (001) substrates were used. This was found to rotate the orientation of the $SmTiO_3$ barrier by 90° relative to the orientation on LSAT. Regularly spaced anisotropic planar defects were observed via TEM. A high degree of anisotropy in the transport properties was found as a result of this, which allowed a systematic investigation of the effect of disorder on carrier-lifetime separation, a commonly observed phenomenon in strongly correlated metals. The temperature dependence of the in-plane resistivity varied greatly with disorder, which could be controlled through the angle of the resistance measurement relative to the planar defects. Remarkably, it was found that even though the in-plane resistance didn't obey a power law at all in the presence of high disorder, the Hall angle still displayed a robust T^2 dependence.

This points to the need for a unified theory that describes this dependence, which has been observed in many other correlated materials systems.

A novel route to the growth of the layered strontium ruthenate Ruddlesden-Popper series, $Sr_{n+1}Ru_nO_{3n+1}$, was presented in Chapter 5. This series of layered perovskite materials hosts a rich array of electronic and magnetic phases, most notably *p*-wave superconductivity in Sr_2RuO_4 and metamagnetism and nematic order in $Sr_3Ru_2O_7$. Epitaxial growth of thin films of these materials allows detailed studies of how subtle modifications of the lattice change the band structure and evolution of the correlated phases. Unfortunately, reproducible growth of these materials is made difficult by the extremely low vapor pressure of ruthenium. We propose a route around this through the use of the volatile inorganic precursor RuO_4 in lieu of a pure ruthenium source. It was demonstrated that Sr_2RuO_4 thin films could be grown with extremely high structural quality, as evidenced by XRD, AFM, TEM and RHEED. It was also shown that by tuning the Sr/Ru flux ratio different members of the series could be stabilized. In particular, the growth of phase-pure films of $Sr_3Ru_2O_7$ and $SrRuO_3$ were demonstrated, which are of significant scientific interest.

Finally, in Chapter 6, the transport properties of a strained $Sr_3Ru_2O_7$ thin film were discussed. In its bulk form, $Sr_3Ru_2O_7$ is known to host strong magnetic fluctuations giving rise to a metamagnetic transition at an in-plane applied magnetic field of 5 T, which is accompanied by a peak in the magnetoresistance. This transition is quantum critical in nature, and it is accompanied by the formation of multiple spin density wave phases in the

vicinity of the metamagnetic transition at low temperatures. In the biaxially compressively stressed thin film sample evidence of enhanced magnetization was seen, with true ferromagnetic order suggesting that the modification of the lattice by the strain may have enhanced the tendency toward magnetic order. This transitioned to order of antiferromagnetic character at temperatures below 20 K, a behavior that has previously been observed in bulk samples. At this transition, the onset of a magnetoresistance anisotropy was found, with the orientation being sensitive to the direction of the applied field. This anisotropy persisted to temperatures that were many orders of magnitude higher than the nematic states previously observed in studies of bulk $Sr_3Ru_2O_7$ crystals. Additionally, field-dependent non-Fermi liquid scattering behavior was observed, with non-Fermi liquid temperature dependence of the resistivity and mass enhancement observed when the applied field was transverse to the current near the critical metamagnetic field.

7.2 Directions for Future Work

The work in this thesis demonstrates the unique advantages of the hybrid molecular beam epitaxy technique in synthesizing films with the aim of probing the low temperature electronic order emerging from the strong electron correlations. Subtle effects, such as small epitaxial strain or the magnetic order of a quantum well barrier material, were shown to greatly influence the emergence of the ordered phases. The many different tuning parameters offered by MBE also open the possibility of engineering the behavior of these

phases for applications in future technology that are not possible with conventional weakly correlated semiconductors. As a result, there are many possible avenues that could be explored to achieve these aims. A few will be highlighted in this section, ranging from specific goals which are direct extensions of the work in this thesis to more general aims for the field strongly correlated materials.

7.2.1 Understanding of T^2 Scattering Behavior in $SrTiO_3$

One of the fundamental observations of transport in correlated 2DEGs in $SrTiO_3$ was T^2 dependences of the transport coefficients. The most striking observation of this behavior was the robust T^2 dependence of the Hall angle $\cot(\theta_H)$ in Chapter 4. Even in the presence of large amounts of disorder, and even when the in-plane resistance $R_{xx}(T)$ did not follow a power law at all, a clear T^2 dependence of $\cot(\theta_H)$ was still observed at all temperatures at which measurements were taken. Adding to this, prior transport studies have revealed T^2 dependences of $R_{xx}(T)$ in regimes where Fermi liquid theory should not apply. A carrier density-independent scattering rate has been measured over a wide range of densities, an observation that is at odds with Fermi liquid theory [20]. Together, these observations support the idea that an underlying, poorly understood scattering mechanism is at play in $SrTiO_3$ that cannot simply be described by Fermi liquid theory, and a deeper understanding is needed.

This behavior is more general than just transport in $SrTiO_3$. There is increasing attention being paid to the $\cot(\theta_H) \sim T^2$ behavior that is observed in the cuprates. In some

cases this behavior is obeyed across the entire phase space of doping and temperature, including in the strange metal regime where T-linear behavior is seen in the resistivity and even in the region where the pseudogap state is observed in the density of states [117]. Attention has also been called to the anomalous T^2 dependence of the resistivity in the cuprates under conditions where conventional Fermi liquid scattering would not be expected to be dominant [118]. This suggests that the T^2 dependence of the Hall angle (and possibly of the resistivity) may be a nearly universal behavior in this class of strongly correlated oxides, and a unifying microscopic theory that can account for this behavior would go a long way toward the development of a complete understanding of the correlations physics in these materials.

7.2.2 Achieving Superconductivity in Hybrid MBE-grown Sr_2RuO_4

It was demonstrated that Sr_2RuO_4 films of excellent structural quality could be grown with the hybrid MBE technique detailed in Chapter 5. In addition to the smooth interfaces confirmed with XRD and AFM, the sharp rocking curve and absence of extended defects in the TEM image demonstrated excellent crystallinity. However, superconducting thin films have not yet been achieved with this technique. The unusual *p*-wave superconductivity in Sr_2RuO_4, with a T_C of 1.5 K, is notorious for being extremely sensitive to the presence of disorder. The coherence length for superconducting pairing in this material is nearly 70 nm, meaning that greater than roughly 70 nm of pristine defect-free material is needed to accommodate the superconducting phase. The absence of any

extended defects in the hybrid MBE grown films, which is often a problem encountered during growth with other more energetic techniques, indicates that point defects are a likely culprit for the increased residual resistivity. Low concentrations of small point defects can be difficult to resolve even with TEM. Possible point defects are carbon impurities introduced from the precursor mixture, which is comprised of 99% fluorinated ethers, and oxygen vacancies.

There are two obvious modifications that could be made to address these problems. The first is growth at a higher substrate temperature. Higher quality perovskite oxides can almost always be attained through the use of higher growth temperatures. With the MBE system setup used to carry out the hybrid technique, the maximum substrate temperature during growth (as measured by a thermocouple) that could be attained was 950 °C. At this temperature the current driven by an external power source was reaching its maximum value, and the high oxygen content needed during this growth (as supplied by a plasma source) increases the risk of filament oxidation and heater failure. To circumvent this, an upgrade to a heater with a more oxygen resistant filament could be considered. An example of such a material available commercially is SiC. This material can withstand much higher temperatures and is also much less prone to oxidation. Operation of heaters with SiC filaments at up to 1200 °C in an oxidizing environment has been reported. This may assist in burning off more of the carbon impurities introduced by the ethers. This may also improve the crystal growth more generally through improved adatom mobility.

Another system modification that would likely improve the electronic properties is an oxygen source capable of providing a higher concentration of active oxygen species. Currently, an RF oxygen plasma source is operated at its maximum power 300 W with a chamber oxygen background pressure of roughly 8×10^{-6} Torr. Plasma sources capable of reaching higher powers are available. This could have several beneficial effects. First, it could reduce carbon impurities by rapidly breaking down the ethers and oxidizing them to more volatile fragments that would desorb from the substrate. It would also ensure that a sufficient amount of active oxygen is supplied to avoid an oxygen deficient film. Finally, it could increase the growth rate by breaking down the RuO_4 precursor molecules more rapidly. Currently, the growth rate is quite low at a value near 15 nm/hr. Enhancing this could further reduce defect incorporation.

7.2.3 Effect of Strain & Symmetry on the $Sr_{n+1}Ru_nO_{3n+1}$ Series

In Chapter 6 the enhanced nematic behavior and magnetic order in strained $Sr_3Ru_2O_7$ films demonstrated the profound effect that perturbations of the lattice can have on the correlated emergent phases. A biaxial in-plane compressive strain of -0.5% was sufficient to enhance the critical temperature for the observation of nematic transport behavior by an order of magnitude. This observation, along with the paucity of reports of transport behavior of strained thin films of the layered $Sr_{n+1}Ru_nO_{3n+1}$ series, naturally invites more work of this type.

In addition to the effect of the lattice mismatch (both tensile and compressive stresses could be explored), one would expect that the symmetry of the substrate would also play an important role. Distorting the symmetry of the film might break the nominally C_4 rotational symmetry of the ruthenate Fermi surface, leading to additional anisotropies in the transport properties or instabilities towards magnetic states. An example would be the growth of the tetragonal $Sr_3Ru_2O_7$ phase on a substrate with a small orthorhombic distortion, thereby making the a and b axes inequivalent. One candidate system is the (110) and (001) surfaces of the orthorhombic perovskite $NdGaO_3$. Schematics of the surfaces of these crystal orientations are shown in Figure 7.1, with the Nd atoms omitted for clarity. Along the (001) surface the pseudocubic lattice constants between the Ga atoms (blue) are equivalent along all directions at a_1 = 3.864 Å, imposing a tetragonal structure in an epitaxial ruthenate film. Along the (110) surface there is a slight orthorhombic distortion, with a_1 = 3.864 Å and a_2 = 3.853 Å, breaking C_4 rotational symmetry and imposing an orthorhombic structure. Although the symmetry breaking on the (110) surface is small, the study in Chapter 6 demonstrated how sensitive the electronic and magnetic properties of the ruthenates are to very subtle structural perturbations.

A direct picture of the band structure is often critical in obtaining a fundamental understanding of the transport behavior and the physics resulting from strong electron correlations. For this reason, ARPES studies of the strained ruthenate films would go a long way in advancing the understanding of the complex nature of the superconductivity and magnetism in these materials. There are reports of ARPES studies for strained thin

films of Sr_2RuO_4 and Ba_2RuO_4 [37]. However, more studies of the $n = 2$ $Sr_3Ru_2O_7$ phase would be helpful, especially in light of the study of strained $Sr_3Ru_2O_7$ detailed in Chapter 6, where it was found that subtle modifications of the Fermi surface can translate to dramatic changes in the resultant magnetic phases. Details of the Fermi surface have a large effect on the physics in this class of materials due the strong nesting and the presence Van Hove Singularities.

7.2.4 $Sr_{n+1}Ru_nO_{3n+1}$ Heterostructures

The many electronic phases observed in the layered strontium ruthenate family and the complex nature of the magnetism make this a ripe area for engineering these interactions through the development of heterostructures. Because of the similar in-plane lattice constants of these materials, in principle any member of the Ruddlesden-Popper series could be grown epitaxially on any other member without relaxation occurring until a substantial thickness limit is reached. Both the epitaxial strain, as discussed in Chapter 6, and proximity effects at the interfaces would likely lead to coupling of various electronic and magnetic phenomena.

A structure that has already attracted much interest is the ferromagnet/superconductor interface at the $SrRuO_3/Sr_2RuO_4$ junction. Because Sr_2RuO_4 is a spin-triplet superconductor with polarizable Cooper pairs, it has been shown that spin-triplet superconductivity can be induced in the otherwise not superconducting $SrRuO_3$ layer [119]. It was found that the superconducting phase could penetrate up to 15 nm into the

$SrRuO_3$ layer via a phenomenon called the *long-range proximity effect*, demonstrating the possible applicability of such interfaces in new types of spintronic devices. Changes in the magnetic properties of the $SrRuO_3$ layer itself have also been reported at such junctions [120].

Interesting follow up experiments would be possible using the $Sr_3Ru_2O_7/Sr_2RuO_4$ interface to see how the superconductivity of Sr_2RuO_4 is influenced by the strong magnetic fluctuations metamagnetism in $Sr_3Ru_2O_7$. It would also be interesting to see what effect proximity to the ferromagnetism of $SrRuO_3$ would have on the metamagnetic transition and nematic behavior of $Sr_3Ru_2O_7$ at the $SrRuO_3/Sr_3Ru_2O_7$ junction, as it could possibly enhance the ferromagnetic instability of the Fermi surface.

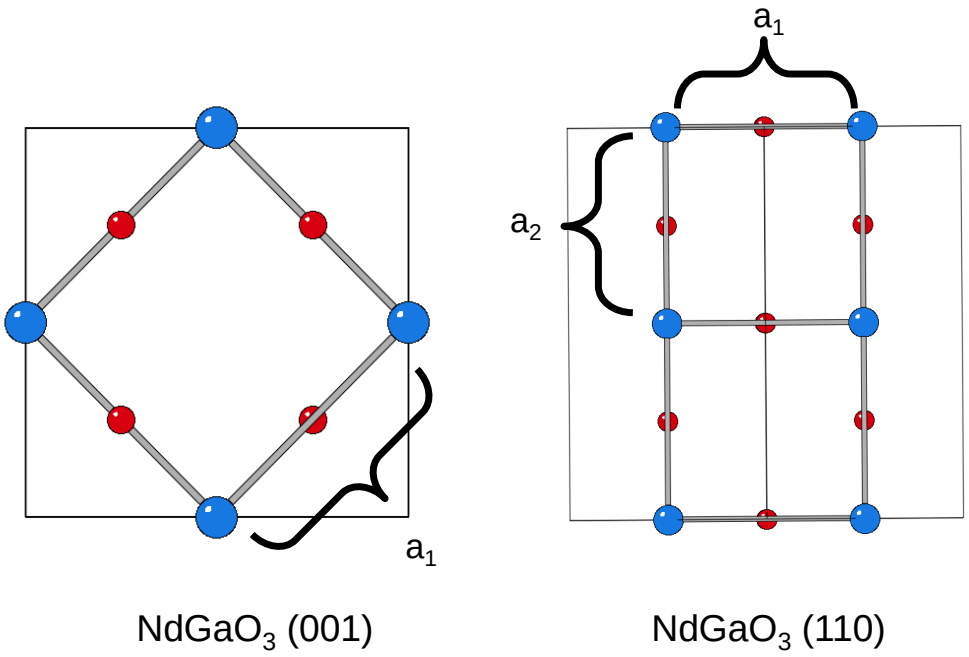

Figure 7.1 Schematic representation of the (001) and (110) surfaces of orthorhombic $NdGaO_3$. The Nd atoms have been omitted for clarity. The epitaxial surface net formed by the Ga ions (blue) on the (001) surface have identical pseudocubic lattice constants of a_1 = 3.864 Å on all sides, forcing tetragonal symmetry in an epitaxial film. Along the (110) surface the pseudocubic lattice constants are inequivalent at a_1 = 3.864 Å and a_2 = 3.853 Å, breaking C_4 rotational symmetry and imposing an orthorhombic structure.

Bibliography

[1] S. Stemmer and A. J. Millis, "Quantum confinement in oxide quantum wells" MRS Bulletin 38: 1032–1039 (2013)

[2] M. Imada, A. Fujimori, and Y. Tokura, "Metal-insulator transitions," *Rev. Mod. Phys.* 70(4): 1039–1263 (1998)

[3] J. H. Ngai, F. J. Walker, and C. H. Ahn, "Correlated Oxide Physics and Electronics" *Annu. Rev. Mater. Res.,* 44(1): 1–17 (2014)

[4] J. G. Bednorz and K. A. Muller, "Possible High Tc Superconductivity in the Ba - La - Cu - O System" *Zeitschrift für Phys. B Condens. Matter* 64: 189–193 (1986)

[5] S. Jin, T. H. Tiefel, M. Mccormack, R. A. Fastnacht, R. Ramesh, and L. H. Chen, "Thousandfold Change in Resistivity Films Magnetoresistive" *Science* 264(5157): 413–415 (2013)

[6] A. Ohtomo and H. Y. Hwang, "A high-mobility electron gas at the LAO/STO heterointerface.," *Nature* 427(6973): 423–426 (2004)

[7] D. Osterbrock, M. J. Aschwanden, L. Fletcher, C. J. Schrijver, G. Alexander, V. M. Nakariakov, L. Ofman, E. E. Deluca, B. Roberts, J. M. Davila, C. E. Deforest, J. B. Gurman, I. De Moortel, J. Ireland, R. W. Walsh, M. A. Marsh, R. W. Walsh, J. M. Pasachoff, F. A. Babcock, K. D. Russell, D. B. Seaton, S. Koutchmy, I. D. Zhugzhda, V. Locans, T. Sakurai, K. Ichimoto, K. P. Raju, J. Singh, J. W. Belcher, P. Charvin, S. W. Mcintosh, B. Fleck, T. D. Tarbell, B. W. Lites, R. Rutten, W. Kalkofen, I. Demoortel, S. M. Jefferies, P. G. Judge, V. Hansteen, A. Pietarila, R. W. Noyes, C. Foullon, V. M. Nakariakov, and E. Verwichte, "Superconducting Interfaces Between Insulating Oxides" *Science* 317: 1196–1200 (2007)

[8] A. Brinkman, M. Huijben, M. Van Zalk, J. Huijben, U. Zeitler, J. C. Maan, W. G. Van Der Wiel, G. Rijnders, D. H. A. Blank, and H. Hilgenkamp, "Magnetic effects at the interface between non-magnetic oxides" *Nat. Mater.* 6(7): 493–496 (2007)

[9] D. A. Dikin, M. Mehta, C. W. Bark, C. M. Folkman, C. B. Eom, and V. Chandrasekhar, "Coexistence of Superconductivity and Ferromagnetism in Two Dimensions" *Phys. Rev. Lett.* 107: 056802 (2011)

[10] L. Li, C. Richter, J. Mannhart, and R. C. Ashoori, "Coexistence of magnetic order and two-dimensional superconductivity at $LaAlO_3/SrTiO_3$ interfaces," *Nat. Phys.* 7(10): 762–766 (2011)

[11] P. Moetakef, T. a. Cain, D. G. Ouellette, J. Y. Zhang, D. O. Klenov, A. Janotti, C. G. Van De Walle, S. Rajan, S. J. Allen, and S. Stemmer, "Electrostatic carrier doping of $GdTiO_3/SrTiO_3$ interfaces" *Appl. Phys. Lett.* 99: 232116 (2011)

[12] J. H. de Boer and E. J. W. Verwey, "Semi-conductors with partially and with completely filled 3*d* -lattice bands" *Proc. Phys. Soc.* 49(4S): 59–71 (1937)

[13] E. Wigner, "Effects of the electron interaction on the energy levels of electrons in metals" *Trans. Faraday Soc.* 34: 678–685 (1938)

[14] N. F. Mott, "The basis of the Electron Theory of Metals, with Special Reference to the Transition Metals" *Proc. Phys. Soc. A* 62: 416 (1949)

[15] J. Hubbard, "Electron correlations in narrow energy bands" *Proc. Phys. Soc. A* 276: 238–257 (1963)

[16] F. Inaba, T. Arima, T. Ishikawa, T. Katsufuji, and Y. Tokura, "Change of electronic properties on the doping-induced insulator-metal transition in $La_{1-x}Sr_xVO_3$," *Phys. Rev. B* 52: 2221–2224 (1995)

[17] Y. Tokura, Y. Taguchi, Y. Okada, Y. Fujishima, T. Arima, K. Kumagai, and Y. Iye, "Filling dependence of electronic properties on the verge of metal–Mott-insulator transition in$Sr_{1-x}La_xTiO_3$" *Phys. Rev. Lett.* 70(14): 2126–2129 (1993)

[18] L. D. Landau, "The theory of a Fermi liquid" *Sov. Phys. JETP* **3** 920 (1957)

[19] W. G. Baber, "The Contribution to the Electrical Resistance of Metals from Collisions Between Electrons," *Proc. R. Soc. Lond. A* 158**:** 383 (1936)

[20] E. Mikheev, S. Raghavan, J. Y. Zhang, P. B. Marshall, A. P. Kajdos, L. Balents, and S. Stemmer, "Carrier density independent scattering rate in $SrTiO_3$-based electron liquids" *Sci. Rep.* 6**:** 1–8 (2016)

[21] M. Vojta, "Quantum phase transitions" *Reports Prog. Phys.* 66: 2069 (2003)

[22] G. R. Stewart, "Non-fermi-liquid behavior in d-and f-electron metals" *Rev. Mod. Phys.* 73: 797–855 (2001)

[23] S. A. Grigera, R. S. Perry, A. J. Schofield, M. Chiao, S. R. Julian, G. G. Lonzarich, S. I. Ikeda, Y. Maeno, A. J. Millis, and A. P. Mackenzie, "Magnetic Field – Tuned Quantum Criticality in the Metallic Ruthenate $Sr_3Ru_2O_7$" 294: 329–333 (2001)

[24] P. Anderson, "Hall effect in the two-dimensional Luttinger liquid" *Phys. Rev. Lett.* 67(15): 2092–2094 (1991)

[25] P. Coleman, A. J. Schofield, and A. M. Tsvelik, “How should we interpret the two transport relaxation times in the cuprates?” *J. Phys. Condens. Matter* 8(48): 9985–10015 (1996)

[26] T. R. Chien, Z. Z. Wang, and N. P. Ong, “Effect of Zn Impurities on the Normal-State Hall Angle in Single-Crystal $YBa_2Cu_{3-x}Zn_xO_{7-d}$” *Phys. Rev. Lett.* 67(15): 2088–2091 (1991)

[27] T. Rosenbaum, A. Husmann, and S. Carter, “Temperature dependence of the Hall angle in a correlated three-dimensional metal” *Phys. Rev. B - Condens. Matter Mater. Phys.* 57(22): R13997–R13999 (1998)

[28] Y. Nakajima, K. Izawa, Y. Matsuda, S. Uji, T. Terashima, H. Shishido, R. Settai, Y. Onuki, and H. Kontani, “Normal-state Hall Angle and Magnetoresistance in Quasi-2D Heavy Fermion $CeCoIn_5$ near a Quantum Critical Point” *J. Phys. Soc. Japan* 73(1): 5–8 (2004)

[29] A. T. Zheleznyak, V. M. Yakovenko, H. Drew, and I. Mazin, “Phenomenological interpretations of the ac Hall effect in the normal state” *Phys. Rev. B - Condens. Matter Mater. Phys.* 57(5): 3089–3098 (1998)

[30] M. Blake and A. Donos, “Quantum critical transport and the hall angle in holographic models” *Phys. Rev. Lett.* 114(2): 1–5 (2015)

[31] L. Van Hove, “The occurrence of singularities in the elastic frequency distribution of a crystal” *Phys. Rev.* 89(6): 1189–1193 (1953)

[32] G. Li, A. Luican, J. M. B. Lopes Dos Santos, A. H. Castro Neto, A. Reina, J. Kong, and E. Y. Andrei, “Observation of Van Hove singularities in twisted graphene layers” *Nat. Phys.* 6(2): 109–113 (2010)

[33] K. Gofron, J. Campuzano, and A. Abrikosov, “Observation of an" Extended" Van Hove Singularity in $YBa_2Cu_4O_8$ by Ultrahigh Energy Resolution Angle-Resolved Photoemission” *Phys. Rev.* 73(24): 3302–3306 (1994)

[34] J. E. Hirsch and D. J. Scalapino, “Enhanced superconductivity in quasi two-dimensional systems” *Phys. Rev. Lett.* 56(25): 2732–2735 (1986)

[35] R. S. Markiewicz, “Phase separation near the Mott transition in $La_{2-x}Sr_xCuO_4$” *J. Phys. Condens. Matter* 2: 665 (1990)

[36] A. A. Novoselov, K.S., Geim, A.K., Morozov, S.V., Jiang, D.A., Zhang, Y., Dubonos, S.V., Grigorieva, I.V. and Firsov, “Electric field effect in atomically thin carbon films” *Science* 306(5696): 666–669 (2004)

[37] B. Burganov, C. Adamo, A. Mulder, M. Uchida, P. D. C. King, J. W. Harter, D. E. Shai, A. S. Gibbs, A. P. Mackenzie, R. Uecker, M. Bruetzam, M. R. Beasley, C. J. Fennie, D. G. Schlom, and K. M. Shen, "Strain Control of Fermiology and Many-Body Interactions in Two-Dimensional Ruthenates" *Phys. Rev. Lett.* (2016)

[38] Y. T. Hsu, W. Cho, A. F. Rebola, B. Burganov, C. Adamo, K. M. Shen, D. G. Schlom, C. J. Fennie, and E. A. Kim, "Manipulating superconductivity in ruthenates through Fermi surface engineering" *Phys. Rev. B.* 94(4): 1–7 (2016)

[39] P. B. Marshall, K. Ahadi, H. Kim, and S. Stemmer, "Electron nematic fluid in a strained $Sr_3Ru_2O_7$ film" *Phys. Rev. B* 97: 155160 (2018)

[40] H. Ding, T. Yokoya, J. C. Campuzano, T. Takahashi, M. Randeria, M. R. Norman, T. Mochiku, K. Kadowaki, and J. Giapintzakis, "Spectroscopic evidence for a pseudogap in the normal state of underdoped high-T_c superconductors" *Nature* 382(6586): 51–54 (1996)

[41] V. Sidorov, M. Nicklas, P. G. Pagliuso, J. L. Sarrao, Y. Bang, V. Balatsky, and J. D. Thompson, "Superconductivity and quantum criticality in $CeCoIn_5$" *Phys. Rev. Lett.* 89(15): 157004 (2002)

[42] S. J. Allen, A. J. Hauser, E. Mikheev, J. Y. Zhang, N. E. Moreno, J. Son, D. G. Ouellette, J. Kally, A. Kozhanov, L. Balents, and S. Stemmer, "Gaps and pseudogaps in perovskite rare earth nickelates" *APL Mater.* 3(6) (2015)

[43] M. Feld, B. Fröhlich, E. Vogt, M. Koschorreck, and M. Köhl, "Observation of a pairing pseudogap in a two-dimensional Fermi gas," *Nature* 480(7375): 75–78 (2011)

[44] C. Renner, B. Revas, J.-Y. Genoud, K. Kadowaki, and Ø. Fischer, "Pseudogap Precursor of the Superconducting Gap in Under- and Overdoped $Bi_2Sr_2CaCu_2O_{8+\delta}$" *Phys. Rev. Lett.* 82(18): 3725–3725 (1999)

[45] M. V. Sadovskii, "Pseudogap in High-Temperature Superconductors" *PHYS-USP* 44(5): 515-539 (2001)

[46] B. L. Altshuler and A. G. Aronov, "Zero bias anomaly in tunnel resistance and electron-electron interaction" *Solid State Commun.* 30: 115–117 (1979)

[47] B. L. Altshuler, a. G. Aronov, and P. A. Lee, "Interaction effects in disordered fermi systems in two dimensions" *Phys. Rev. Lett.* 44(19): 1288–1291 (1980)

[48] W. L. McMillan and J. Mochel, "Electron Tunneling Experiments on Amorphous $Ge_{1-x}Au_x$" *Phys. Rev. Lett.* 46(8): 556–557 (1981)

[49] Y. Imry and Z. Ovadyahu, "Density-of-States Anomalies in a Disordered Conductor: A Tunneling Study" *Phys. Rev. Lett.* 49(11): 841–844 (1982)

[50] A. L. Efros and B. I. Shklovskii, "Coulomb gap and low temperature conductivity of disordered systems" *J. Phys. C Solid State Phys.* 8: L49–L51 (1975)

[51] M. Lee, J. G. Massey, V. L. Nguyen, and B. I. Shklovskii, "Coulomb gap in a doped semiconductor near the metal-insulator transition: Tunneling experiment and scaling ansatz" *Phys. Rev. B* 60(3): 1582–1591 (1999)

[52] V. M. Goldschmidt, "Die Gesetze der Krystallochemie," *Naturwissenschaften* 14(21): 477–485 (1926)

[53] A. C. Komarek, H. Roth, M. Cwik, W. D. Stein, J. Baier, M. Kriener, F. Bourée, T. Lorenz, and M. Braden, "Magnetoelastic coupling in $RTiO_3$ (R=La,Nd,Sm,Gd,Y) investigated with diffraction techniques and thermal expansion measurements" *Phys. Rev. B - Condens. Matter Mater. Phys.* 75(22): 1–12 (2007)

[54] G. Khalsa and A. H. MacDonald, "Theory of the $SrTiO_3$ Surface State Two-Dimensional Electron Gas" *Phys. Rev. B - Condens. Matter Mater. Phys.* 86: 125121 (2012)

[55] S. Thiel, G. Hammelr, A. Schmehl, C. W. Schneider, and J. Mannhart, "Tunable Quasi-Two-Dimensional Electron Gases in Oxide Heterostructures" *Science* 313: 1942–1945 (2006)

[56] M. Huijben, A. Brinkman, G. Koster, G. Rijnders, H. Hilgenkamp, and D. H. A. Blank, "Structure-Property Relation of $SrTiO_3$/$LaAlO_3$Interfaces" *Adv. Mater.* 21(17): 1665–1677 (2009)

[57] P. Moetakef, D. G. Ouellette, J. R. Williams, S. James Allen, L. Balents, D. Goldhaber-Gordon, and S. Stemmer, "Quantum oscillations from a two-dimensional electron gas at a Mott/band insulator interface" *Appl. Phys. Lett.* 101(15): 1–5 (2012)

[58] S. Raghavan, S. James Allen, and S. Stemmer, "Subband structure of two-dimensional electron gases in $SrTiO_3$" *Appl. Phys. Lett*, 103: 212103 (2013)

[59] P. Moetakef, C. A. Jackson, J. Hwang, L. Balents, S. J. Allen, and S. Stemmer, "Toward an artificial Mott insulator: Correlations in confined high-density electron liquids in $SrTiO_3$" *Phys. Rev. B - Condens. Matter Mater. Phys.* 86(20): 1–4 (2012)

[60] C. A. Jackson and S. Stemmer, "Interface-induced magnetism in perovskite quantum wells" *Phys. Rev. B - Condens. Matter Mater. Phys.* 88: 180403(R) (2013)

[61] J. Y. Zhang, C. A. Jackson, R. Chen, S. Raghavan, P. Moetakef, L. Balents, and S.

Stemmer, "Correlation between metal-insulator transitions and structural distortions in high-electron-density $SrTiO_3$ quantum wells" *Phys. Rev. B - Condens. Matter Mater. Phys.* 89(7): 2–6 (2014)

[62] C. A. Jackson, J. Y. Zhang, C. R. Freeze, and S. Stemmer, "Quantum critical behaviour in confined $SrTiO_3$ quantum wells embedded in antiferromagnetic $SmTiO_3$" *Nat. Commun.* 5: 4258 (2014)

[63] E. Mikheev, C. R. Freeze, B. J. Isaac, T. A. Cain, and S. Stemmer, "Separation of transport lifetimes in $SrTiO_3$-based two-dimensional electron liquids" *Phys. Rev. B* 91(16): 1–6 (2015)

[64] R. F. Need, P. B. Marshall, E. Kenney, A. Suter, T. Prokscha, Z. Salman, B. J. Kirby, S. Stemmer, M. J. Graf, and S. D. Wilson, "Quasistatic antiferromagnetism in the quantum wells of $SmTiO_3/SrTiO_3$ heterostructures" *npj Quantum Mater.* 3(1): 7 (2018)

[65] Y. Maeno, H. Hashimoto, K. Yoshida, S. Nishizaki, T. Fujita, J. G. Bednorz, and F. Lichtenberg, "Superconductivity in a layered perovskite without copper" *Nature* 372: 532–534 (1994)

[66] K. Ishida, H. Mukuda, Y. Kitaoka, K. Asayama, Z. Q. Mao, Y. Mori, and Y. Maeno, "Spin-triplet superconductivity in Sr_2RuO_4 identified by 17-O Knight Shift," *Nature* 396: 658-660 (1998)

[67] R. S. Perry, L. M. Galvin, S. A. Grigera, L. Capogna, A. J. Schofield, A. P. Mackenzie, M. Chiao, S. R. Julian, S. Nakatsuji, C. Pfleiderer, S. I. Ikeda, and Y. Maeno, "Metamagnetism and critical fluctuations in high quality single crystals of the bilayer ruthenate $Sr_3Ru_2O_7$" *Phys. Rev. Lett.* 86(12): 2661–2664 (2001)

[68] R. A. Borzi, S. A. Grigera, J. Farrell, R. S. Perry, S. J. S. Lister, S. L. Lee, D. A. Tennant, Y. Maeno, and A. P. Mackenzie, "Formation of a Nematic Fluid at High Fields in $Sr_3Ru_2O_7$" *Science* 315(5809): 214-217 (2007)

[69] C. Lester, S. Ramos, R. S. Perry, T. P. Croft, R. I. Bewley, T. Guidi, P. Manuel, D. D. Khalyavin, E. M. Forgan, and S. M. Hayden, "Field tunable spin density wave phases in $Sr_3Ru_2O_7$" *Nature Materials* 14: 1–6 (2015)

[70] J. M. Longo, P. M. Raccah, and J. B. Goodenough, "Magnetic Properties of $SrRuO_3$ and $CaRuO_3$" *J. Appl. Phys.* 39(2): 1327–1328 (1968)

[71] D. H. Lu, M. Schmidt, T. R. Cummins, S. Schuppler, F. Lichtenberg, and J. G. Bednorz, "Fermi surface and extended van hove singularity in the noncuprate superconductor Sr_2RuO_4" *Phys. Rev. Lett.* 76(25): 4845–4848 (1996)

[72] A. Tamai, M. P. Allan, J. F. Mercure, W. Meevasana, R. Dunkel, D. H. Lu, R. S. Perry, A. P. MacKenzie, D. J. Singh, Z. X. Shen, and F. Baumberger, "Fermi Surface and van Hove Singularities in the Itinerant Metamagnet $Sr_3Ru_2O_7$" *Phys. Rev. Lett.* 101(2): 9–12 (2008)

[73] N. Kikugawa, C. Bergemann, A. P. Mackenzie, and Y. Maeno, "Band-selective modification of the magnetic fluctuations in Sr_2RuO_4: A study of substitution effects" *Phys. Rev. B - Condens. Matter Mater. Phys.* 70(13): 1–7 (2004)

[74] J. J. Cuomo, D. L. Pappas, J. Bruley, J. P. Doyle, and K. L. Saenger, "Vapor deposition processes for amorphous carbon films with sp^3 fractions approaching diamond" *J. Appl. Phys.* 70(3): 1706–1711 (1991)

[75] J. R. Arthur, "Interaction of Ga and As_2 Molecular Beams with GaAs Surfaces" *J. Appl. Phys.* 39(8): 4032–4034 (1968)

[76] B. Jalan, R. Engel-Herbert, N. J. Wright, and S. Stemmer, "Growth of high-quality $SrTiO_3$ films using a hybrid molecular beam epitaxy approach" *J. Vac. Sci. Technol. A Vacuum, Surfaces, Film.* 27(3): 461–464 (2009)

[77] B. Jalan, P. Moetakef, and S. Stemmer, "Molecular beam epitaxy of $SrTiO_3$ with a growth window" *Appl. Phys. Lett.* 95(3): 2–5 (2009)

[78] J. Son, P. Moetakef, B. Jalan, O. Bierwagen, N. J. Wright, R. Engel-Herbert, and S. Stemmer, "Epitaxial $SrTiO_3$ films with electron mobilities exceeding 30,000 $cm^2V^{-1}s^{-1}$" *Nat. Mater.* 9(6): 482–484 (2010)

[79] T. A. Cain, A. P. Kajdos, and S. Stemmer, "La-doped $SrTiO_3$ films with large cryogenic thermoelectric power factors" *Appl. Phys. Lett.* 102: 182101 (2013)

[80] C. Eaton, J. A. Moyer, H. M. Alipour, E. D. Grimley, M. Brahlek, J. M. LeBeau, and R. Engel-Herbert, "Growth of $SrVO_3$ thin films by hybrid molecular beam epitaxy" *J. Vac. Sci. Technol. A Vacuum, Surfaces, Film.* 33(6): 061504 (2015)

[81] A. Prakash, J. Dewey, H. Yun, J. S. Jeong, K. A. Mkhoyan, and B. Jalan, "Hybrid molecular beam epitaxy for the growth of stoichiometric $BaSnO_3$" *J. Vac. Sci. Technol. A Vacuum, Surfaces, Film.* 33(6): 060608 (2015)

[82] P. B. Marshall, H. Kim, K. Ahadi, and S. Stemmer, "Growth of strontium ruthenate films by hybrid molecular beam epitaxy" *APL Mater.* 5: 096101 (2017)

[83] J. Bardeen, "Tunnelling from a many-particle point of view" *Phys. Rev. Lett.* 6(2): 57–59 (1961)

[84] I. Giaever, "Energy Gap in Superconductors Measured by Electron Tunneling"

Phys. Rev. Lett. 5(4): 147–148 (1960)

[85] P. B. Marshall, E. Mikheev, S. Raghavan, and S. Stemmer, "Pseudogaps and Emergence of Coherence in Two-Dimensional Electron Liquids in $SrTiO_3$" *Phys. Rev. Lett.* 117: 046402 (2016)

[86] J. A. Stroscio, R. M. Feenstra, and A. P. Fein, "Electronic structure of the Si(111)2x1 surface by scanning-tunneling microscopy" *Phys. Rev. Lett.* 57(20): 2579–2582 (1986)

[87] R. M. Feenstra, J. a Stroscio, and A. P. Fein, "Tunneling spectroscopy of the Si(111)2x1 surface" *Surf. Sci.* 181(1–2): 295–306 (1987)

[88] N. D. Lang, "Spectroscopy of single atoms in the scanning tunneling microscope" *Phys. Rev. B* 34(8): 2–5 (1986)

[89] D. N. Basov, E. J. Singley, and S. V. Dordevic, "Sum rules and electrodynamics of high-T_C cuprates in the pseudogap state" *Phys. Rev. B - Condens. Matter Mater. Phys.* 65(5): 1–7 (2002)

[90] U. Chatterjee, J. Zhao, M. Iavarone, R. Di Capua, J. P. Castellan, G. Karapetrov, C. D. Malliakas, M. G. Kanatzidis, H. Claus, J. P. C. Ruff, F. Weber, J. C. Campuzano, R. Osborn, M. Randeria, N. Trivedi, M. R. Norman, and S. Rosenkranz, "Emergence of coherence in the charge density wave state of 2H-$NbSe_2$" *Nat. Comm.* 6: 6313 (2015)

[91] J. Schmalian, D. Pines, and B. Stojković, "Microscopic theory of weak pseudogap behavior in the underdoped cuprate superconductors: General theory and quasiparticle properties" *Phys. Rev. B - Condens. Matter Mater. Phys.* 60(1): 667–686 (1999)

[92] F. Lechermann, "Unconventional electron states in delta-doped $SmTiO_3$" *Sci. Rep.* 7: 1565 (2017)

[93] S. Nair, S. Wirth, S. Friedemann, F. Steglich, Q. Si, A. J. Schofield, S. Nair, S. Wirth, S. Friedemann, F. Steglich, Q. Si, and A. J. Schofield, "Hall effect in heavy fermion metals" *Adv. Phys.*, 61(5): 583–664 (2012)

[94] P. B. Marshall, H. Kim, and S. Stemmer, "Disorder versus two transport lifetimes in a strongly correlated electron liquid" *Sci. Rep.* 7: 10312 (2017)

[95] G. Xiao, P. Xiong, and M. Z. Cieplak, "Universal Hall effect in $La_{1.85}Sr_{0.15}Cu_{1-x}A_xO_4$ systems (A = Fe, Co, Ni, Zn, Ga)," *Phys. Rev. B* 46(13): 8687–8690 (1992)

[96] R. Chen, S. Lee, and L. Balents, "Dimer Mott insulator in an oxide heterostructure"

Phys. Rev. B - Condens. Matter Mater. Phys. 87: 161119(R) (2013)

[97] J. Iaconis, H. Ishizuka, D. N. Sheng, and L. Balents, "Kinetic magnetism at the interface between Mott and band insulators" *Phys. Rev. B* 93: 155144 (2016)

[98] N. F. Berk and J. R. Schrieffer, "Effect of ferromagnetic spin correlations on superconductivity" *Phys. Rev. Lett.* 17(8): 433–435 (1966)

[99] Y. Li, W. Tabis, G. Yu, N. Barišić, and M. Greven, "Hidden Fermi-liquid Charge Transport in the Antiferromagnetic Phase of the Electron-Doped Cuprate Superconductors" *Phys. Rev. Lett.* 117(19): 1–6 (2016)

[100] Y. Maeno, H. Hashimoto, K. Yoshida, S. Nishizaki, T. Fujita, J. G. Bednorz, and F. Lichtenberg, "Superconductivity in a layered perovskite without copper" *Nature* 372: 532–534 (1994)

[101] Y. Krockenberger, M. Uchida, K. S. Takahashi, M. Nakamura, M. Kawasaki, and Y. Tokura, "Growth of superconducting Sr_2RuO_4 thin films" *Appl. Phys. Lett.* 97(8): 082502, (2010)

[102] M. Uchida, M. Ide, H. Watanabe, K. S. Takahashi, Y. Tokura, and M. Kawasaki, "Molecular beam epitaxy growth of superconducting Sr_2RuO_4 films" *APL Mater.* 5(10): 106108 (2017)

[103] J. Gatineau, K. Yanagita, and C. Dussarrat, "A new RuO_4 solvent solution for pure ruthenium film depositions" *Microelectron. Eng.* 83(11–12): 2248–2252 (2006)

[104] J. H. Han, S. W. Lee, S. K. Kim, S. Han, C. S. Hwang, C. Dussarrat, and J. Gatineau, "Growth of RuO_2 thin films by pulsed-chemical vapor deposition using RuO_4 precursor and 5% H_2 reduction gas" *Chem. Mater.* 22(20): 5700–5706 (2010)

[105] J. H. Han, W. Lee, W. Jeon, S. W. Lee, C. S. Hwang, C. Ko, and J. Gatineau, "Growth of Conductive $SrRuO_3$ Films by Combining Atomic Layer Deposited SrO and Chemical Vapor Deposited RuO_2 Layers" *Chem. Mater.* 24(24): 4686–4692 (2012)

[106] D. Reisinger, B. Blass, J. Klein, J. B. Philipp, M. Schonecke, A. Erb, L. Alff, and R. Gross, "Sub-unit cell layer-by-layer growth of Fe_3O_4, MgO, and Sr_2RuO_4 thin films" *Appl. Phys. A Mater. Sci. Process.* 77(5): 619-621 (2003)

[107] L. Walz and F. Lichtenberg, "Refinement of the structure of Sr_2RuO_4 with 100 and 295 K X-ray data" *Acta Crystallogr. Sect. C Cryst. Struct. Commun.* 49(7): 1268–1270 (1993)

[108] L. Capogna, E. M. Forgan, S. M. Hayden, A. Wildes, J. A. Duffy, A. P. Mackenzie,

R. S. Perry, S. Ikeda, Y. Maeno, and S. P. Brown, "Observation of two-dimensional spin fluctuations in the bilayer ruthenate $Sr_3Ru_2O_7$" *Phys. Rev. B* 67(1): 012504 (2003)

[109] S. I. Ikeda, N. Shirakawa, T. Yanagisawa, Y. Yoshida, S. Koikegami, S. Koike, M. Kosaka, and Y. Uwatoko, "Uniaxial-pressure induced ferromagnetism of enhanced paramagnetic $Sr_3Ru_2O_7$" *J. Phys. Soc. Japan* 73(5): 1322–1325 (2004)

[110] H. Shaked, J. D. Jorgensen, S. Short, O. Chmaissem, S.-I. Ikeda, and Y. Maeno, "Temperature and pressure effects on the crystal structure of $Sr_3Ru_2O_7$: Evidence for electronically driven structural responses" *Phys. Rev. B* 62(13): 8725–8730 (2000)

[111] C. W. Hicks, D. O. Brodsky, E. A. Yelland, A. S. Gibbs, J. A. N. Bruin, M. E. Barber, S. D. Edkins, K. Nishimura, S. Yonezawa, Y. Maeno, and A. P. Mackenzie, "Strong Increase of T_C of Sr_2RuO_4 Under Both Tensile and Compressive Strain" *Science* 344(6181): 283–285 (2014)

[112] M. E. Barber, A. S. Gibbs, Y. Maeno, A. P. Mackenzie, and C. W. Hicks, "Resistivity in the Vicinity of a van Hove Singularity: Sr_2RuO_4 under Uniaxial Pressure" *Phys. Rev. Lett.* 120(7): 76602 (2018)

[113] B. Binz and M. Sigrist, "Metamagnetism of itinerant electrons in multi-layer ruthenates" *Europhys. Lett.* 65(6): 816–822 (2004)

[114] Y. M. Blanter, M. I. Kaganov, A. V. Pantsulaya, and A. A. Varlamov, "The theory of electronic topological transitions" *Phys. Rep.* 245: 159–257 (1994)

[115] H. Y. Kee and Y. B. Kim, "Itinerant metamagnetism induced by electronic nematic order," *Phys. Rev. B - Condens. Matter Mater. Phys.* 71(18): 1–4 (2005)

[116] R. Arita, K. Kuroki, and H. Aoki, "Electron-correlation-originated negative magnetoresistance in a system having a partly flat band" *Phys. Rev. B - Condens. Matter Mater. Phys.* 61(5): 3207–3210 (2000)

[117] N. Barišić, M. K. Chan, M. J. Veit, C. J. Dorow, Y. Ge, Y. Tang, W. Tabis, G. Yu, X. Zhao, and M. Greven, "Evidence for a universal Fermi-liquid scattering rate throughout the phase diagram of the copper-oxide superconductors" *arXiv*: 1507.07885 (2015)

[118] T. Sarkar, R. L. Greene, and S. Das Sarma, "Anomalous normal state resistivity in superconducting $La_{2-x}Ce_xCuO_4$: Fermi liquid or strange metal" *arXiv*: 1805.08360 (2018)

[119] M. S. Anwar, S. R. Lee, R. Ishiguro, Y. Sugimoto, Y. Tano, S. J. Kang, Y. J. Shin,

S. Yonezawa, D. Manske, H. Takayanagi, T. W. Noh, and Y. Maeno, "Direct penetration of spin-triplet superconductivity into a ferromagnet in Au/$SrRuO_3$/Sr_2RuO_4 junctions" *Nat. Commun.* 7: 13220 (2016)

[120] Y. Sugimoto, M. S. Anwar, S. R. Lee, Y. J. Shin, S. Yonezawa, T. W. Noh, and Y. Maeno, "Ferromagnetic Properties of $SrRuO_3$ Thin Films Deposited on the Spin-Triplet Superconductor Sr_2RuO_4" *Phys. Procedia* 75: 413–418 (2015)